Temperature-Controlled MEMS Reactors and Photonic Crystals for In-Situ Transmission Electron Microscopy

Erdamar, A.K.

Citation (APA)
Erdamar, A. K. (2026). *Temperature-Controlled MEMS Reactors and Photonic Crystals for In-Situ Transmission Electron Microscopy*. [Dissertation (TU Delft), Delft University of Technology]. https://doi.org/10.4233/uuid:198800d7-4c8c-4e7b-90b7-3acd1b5e9042

Important note
To cite this publication, please use the final published version (if applicable).
Please check the document version above.

Temperature-Controlled MEMS Reactors and Photonic Crystals for In-Situ Transmission Electron Microscopy

Ahmet Koray Erdamar

Temperature-Controlled MEMS Reactors and Photonic Crystals for In-Situ Transmission Electron Microscopy

Dissertation

For the purpose of obtaining the degree of doctor at Delft University of Technology by the authority of the Rector Magnificus, Prof. dr.ir. H. Bijl chair of the Board for Doctorates to be defended publicly on Thursday 22 January 2026 at 15:00

by

Ahmet Koray ERDAMAR

Master of Science in Physics, Koç University, Türkiye

born in Ankara, Türkiye

This dissertation has been approved by the promotors

Prof. dr. P.J. French
Prof. dr. U. Staufer

Composition of the doctoral committee:
Rector Magnificus   chairperson
Prof. dr. P.J. French   Delft University of Technology, Promotor
Prof. dr. U. Staufer   Delft University of Technology, Promotor

Independent members:
Prof.dr. T. Akin   Middle East Technical University, Türkiye
Prof.dr.ir. W.D. van Driel   Delft University of Technology
Prof.dr.ir. J.P. Hoogenboom   Delft University of Technology
Prof.dr. H.P. Urbach   Delft University of Technology
Dr. G. Pandraud   Ommatidia LiDAR, the Netherlands

An electronic version of this dissertation is available at
http://repository.tudelft.nl/.

To Ata

<div align="center">**Table of Contents**</div>

Chapter 1: Introduction

Chapter 2: Fabrication of MEMS-based Heaters and Si Photonic Crystals

Chapter 3: Electron-beam lithography technique for SiN membrane applications

Chapter 4: Closed Cell Systems for in situ TEM with gas environments

Chapter 5: Thermal tuning of a silicon photonic crystal cavity infilled with an elastomer

CHAPTER 1

Introduction

1.1 General Introduction

Transmission Electron Microscopy (TEM) is a crucial tool for studying materials at an incredibly tiny scale, revealing details at the atomic level [1]. By going beyond what conventional light microscopes can see, TEM allows scientists to observe structures as small as a fraction of a nanometer, offering insights into how atoms and molecules arrange themselves within materials [2]. To push the boundaries of TEM, scientists have been exploring the integration of microelectromechanical systems (MEMS) heaters. These tiny heaters offer precise control over temperature inside the microscope, allowing researchers to study materials under different heat conditions [3].

Moreover, combining TEM with photonic crystals opens up exciting possibilities at the intersection of nanophotonics and materials science. Photonic crystals are materials with regular patterns that affect how light behaves within them, holding promise for various applications such as better optical communication and sensors [4]. By using TEM together with a technique called cathodoluminescence (CL) spectroscopy, scientists can study the optical properties of photonic crystals with high detail, understanding how their structure influences how they interact with light.

This thesis dives deep into TEM, MEMS heaters, and photonic crystals, exploring their unique contributions and how they can work together to advance our understanding of materials at the nanoscale. Through a mix of experiments, theories, and real-world applications, this research aims to shed light on new possibilities in materials science, nanotechnology, and photonics.

1.2 Transmission Electron Microscopy (TEM)

Transmission Electron Microscopy (TEM) is a powerful imaging technique that enables scientists to observe the ultrastructure of materials at nanometer-scale resolution [1]. Unlike conventional light microscopy, which has a resolution limit of around 200 nanometers due to the wavelength of visible light, TEM utilizes a beam of electrons to achieve much higher resolution. This allows for the visualization of individual atoms and their arrangement within a sample.

The development of TEM can be traced back to the early 20th century when scientists began exploring the wave-particle duality of electrons. Ernst Ruska and Max Knoll built the first prototype of the TEM in 1931, which consisted of an electron source, electromagnetic lenses, and a fluorescent screen for image detection [5]. This groundbreaking invention laid the foundation for further advancements in electron microscopy.

The fundamental principle underlying TEM is the interaction of electrons with matter. When a beam of electrons passes through a thin specimen, it undergoes various interactions, including elastic scattering, inelastic scattering, and diffraction [2]. These interactions provide valuable information about the structure, composition, and properties of the sample. Modern TEM instruments are highly sophisticated devices equipped with electron guns, electromagnetic lenses, specimen stages, detectors, and advanced imaging and analysis software [1]. Electron guns—such as thermionic, field emission, or Schottky emitters—generate a beam of electrons. In particular, field emission guns (FEGs) are used to produce a highly coherent electron beam due to their small source size and high brightness. However, the degree of coherence in an electron beam depends on the type of electron source, operating conditions, and instrument configuration. Therefore, while some TEMs provide highly coherent beams (especially those using FEGs), not all electron beams in electron microscopes are inherently coherent. Electromagnetic lenses focus and manipulate the beam to form an image, while specimen stages allow for precise positioning and manipulation of samples, enabling researchers to examine different regions of interest.

1.3   Types of Transmission Electron Microscopy and Applications

There are several variants of transmission electron microscopy (TEM), each optimized for specific applications. Conventional TEM is the most widely used mode, in which images are formed by electrons transmitted through a thin specimen and detected on the opposite side. High-resolution TEM (HRTEM) enables imaging at atomic-scale resolution and is therefore particularly suited for investigating crystal structures, defects, and interfaces. Scanning transmission electron microscopy (STEM) employs a finely focused electron probe that is scanned across the specimen while transmitted electrons are collected to form an image. In addition to high spatial resolution, STEM allows for compositional analysis through techniques such as energy-dispersive X-ray spectroscopy (EDS)[6].

TEM is applied across a wide range of disciplines, including materials science, nanotechnology, biology, and medicine [1]. It is commonly used to characterize nanomaterials, investigate biological specimens such as cells and viruses, analyze defects in semiconductor devices, and study structure–property relationships in materials. In this thesis, TEM is employed in combination with MEMS-based devices to enable controlled in situ experiments; the corresponding methodologies and applications are discussed in the following section of this chapter.

1.4   MEMS-based devices for TEM

Microelectromechanical systems (MEMS) can be described in the simplest way as mechanical and electro-mechanical systems in micron size. MEMS devices are mostly driven by electrical motion and used as actuators or sensors. For in situ transmission electron microscopy (TEM) experiments we are using MEMS-based heaters to reach required temperatures for material investigations.

Figure 1.1 shows the design of MEMS based heater which has four contact pad connections and spiral microheater. Our MEMS-based heaters, in other words microheaters, are fabricated on silicon substrate by using metal layer which is embedded in silicon nitride. The choice of the metal for heating and the isolation layer is important. In order to investigate temperature dependent material properties with TEM, microheater has to reach to elevated temperatures.
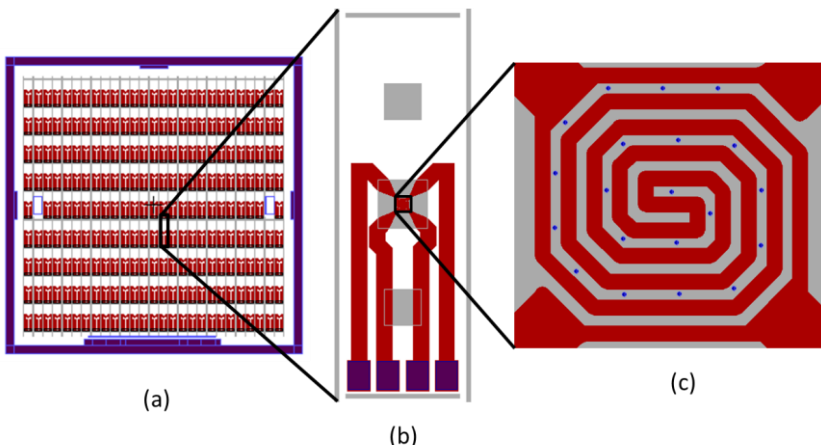
Figure 1.1. Design of four contact pad MEMS based single heater. (a) Mask design of the heater (5-inch mask, that is used to fabricate 4-inch silicon substrate), (b) enlarged of one 4 contact pad single heater. The dimension of the heater is 3.5 mm x 10 mm. Red lines demonstrate the used metal for heating which is embedded in silicon nitrite (SiN). Purple areas are the contact pad for applying voltage and temperature reading. Grey square areas are 400 nm thick SiN membranes. (c) Enlarged of microheater where blue circles are ultra-thin (~20 nm) SiN electron transparent windows.

In our heaters, we used platinum as a heating metal which is embedded in 400 nm thick SiN layer. Platinum heaters can go up to 800 ^{0}C degrees. Depending on the heating metal choice such as; tungsten (W) or molybdenum

(Mo), temperatures above 800 ^{0}C degrees can be reached. As it is shown in Figure 1.1, microheater has ultra-thin (~20 nm) silicon nitride electron transparent windows. These windows have a diameter of 6 μm, and they are located between the metal coils across the microheater. These electron transparent windows are used to perform TEM studies. The specimens can be located across these windows, and image can be obtained by transmitted electrons via specimen and ultra-thin SiN windows. Since there are more than one electron transparent windows, microheater can be used to investigate different specimens. Therefore, uniform heat distribution is important to run different experiments in different windows on heater.

In addition to providing localized heating and uniform thermal distribution, the microheater must also function as a highly accurate temperature sensor. Temperature sensing is based on the temperature dependence of the electrical resistance of the heating material. To achieve simultaneous heating and resistance measurement, a four-point probe configuration is employed. In this arrangement, an electric current is applied through the outer pair of contacts, while the voltage drop is measured across the inner pair. This setup effectively eliminates the influence of contact resistance and enables precise calculation of the electrical resistance. Since the resistance of the heating element varies predictably with temperature, it can be used as a reliable indicator of the microheater's thermal state. Prior to each experiment, a subset of microheaters from the same fabrication batch is calibrated. Due to the uniformity in metal thickness and geometry within a single batch, the resistance–temperature characteristics of the devices are highly consistent. This allows the voltage and resistance values corresponding to specific temperatures to be determined in advance and used for accurate control during in situ TEM experiments. The microheaters are operated under closed-loop control systems that continuously monitor resistance in real time and adjust the input power to maintain the desired temperature. This feedback mechanism ensures stable and precise thermal regulation under a variety of environmental conditions, including gas, liquid, and pressurized settings. Furthermore, the microheaters function at very low power levels, generally within the milliwatt range, which helps to minimize thermal drift in the TEM holder. This results in a drift rate as low as approximately 3 nanometers per minute.

In order to obtain aforementioned properties for microheater, fabrication process has to be stable. Microheater has to be reproducible with same parameters, such as thickness of the metal that leads to same resistance values, and the roughness of the electron transparent windows that leads to better imaging quality. For certain experiments, strength of these electron transparent windows is very important not to cause any leakage during in situ

TEM experiment. Above conditions make the fabrication processes of the microheater very critical. The fabrication of a microheater involves several complex and essential steps, including deposition, lithography, etching, dicing, and cleaning, all of which are critical and can significantly impact the properties and performance of the microheater. These steps are discussed in detailed in Chapter 2.

1.5   Photonic Integrated circuit

The invention of the integrated circuit (IC) by Jack Kilby in 1958 marked the beginning of the modern semiconductor industry [7]. Integrated circuits quickly became essential components in electronic devices, especially in computers and communication systems. In 1965, Gordon Moore, co-founder of Intel, made an important observation—later known as Moore's Law—stating that the number of transistors on a single chip would double approximately every two years [8]. This prediction was not only about improvements in technology, but also about how those improvements made computing more affordable. As transistors became smaller and more efficient to produce, the cost per function decreased, allowing faster and cheaper computers to be developed [9]. This relationship between technology and economics has driven decades of innovation in chip manufacturing. As of 2023, one of the most advanced chips, Intel's Ponte Vecchio GPU, contains around 100 billion transistors, spread across 47 interconnected chiplets made using five different manufacturing processes [10]. According to Intel's roadmap, processors using 5 nm technology are expected to become commercially available soon [11]. However, as more transistors are packed into a chip, challenges such as increased wiring density, greater heat generation, and slower electrical signals have become major concerns [12]. These issues limit the performance of modern chips. To overcome these limits, researchers and industry are increasingly exploring optical interconnects, which can provide faster data transmission and lower power consumption compared to traditional electrical connections [13].

Optical circuit or with another name so called "photonic integrated circuits" can be a solution to obtain faster, cheaper, reliable ways for telecommunications. Using light instead of electrons has many advantages in the transfer of data from one point to another, such as reducing crosstalk, and increasing the speed of the transmission, and eliminating losses. In the last four decades the development in optical fibre technology has resulted in their successful application in optical fibre networks that allow for the transmittance of enormous amounts of data over long distances with faster

way. Nowadays, optical fibre connection is very well spread that leads daily life easier and faster while using many technological devices.

In order to transmit the data through by optical signals in these fibres, at the end of the fibre the optical signal has to be converted to electronic signals for data processing. The electronic devices which are used to convert these optical signals to electronic signals are slow and inefficient when they are compared with the speed and amount of the optical signals. Due to these reasons, the signal processing and conversion should be performed by an all-optical process. Hereby the photonic integrated devices are needed for signal processing applications. Photonic crystals are one of the important candidates for the future photonic integrated devices and applications, since it is possible to control the light with photonic crystals that can be operated as a sensor or as switch applications by monitoring the spectral changes in the photonic devices. The sensitivity of the photonic devices can be adjusted or increased due to strong light-matter interactions depending on the type of used material and its optical properties such as transmission, refractive indices. Photonic integrated devices can be fabricated on different materials such as silicon (Si), gallium arsenide (GaAs), or indium phosphide (InP). Using photonic integrated circuits instead of electronic circuits also enables to solve packaging, coupling problems that leads to cost efficient, small size devices.

1.6   Photonic Crystal

Photonic crystals (PhCs) are artificial dielectric materials with a periodic modulation of the dielectric constant, the modulation period being on the order of the wavelength of light in the dielectric material. Yablonovitch [14] introduced the photonic crystals, and also called photonic band-gap material which is the most striking property of the PhC. This is a range of wavelengths where the photonic crystal is opaque for light, while it is highly transparent outside this range. Photonic-band gap is similar to electronic band-gap in semiconductors where electronic states do not exist. By using the photonic-band gap and other PhC properties, such as design, material, refractive indices, the propagation of light can be controlled very efficiently [4], so that PhCs are important for future integrated photonics circuits.

The periodicity of the modulation of the refractive index in a PhC can be in 1D, 2D, and 3D and this one can distinguish the type of the photonic crystals as one-dimensional, two dimensional and three dimensional. Figure 1.2 shows the schematic representation of the photonic crystals in different dimensions. The most well-known one-dimensional photonic crystal example is Distributed Bragg Mirror.
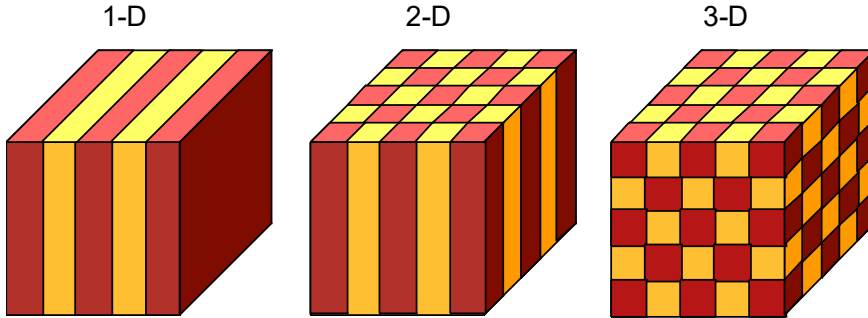
Figure 1.2. Schematic representation of the different dimension of the PhC. The different dielectric constants are represented with different colours. The image is taken from Joannopoulos [4].

The two-dimensional and three-dimensional photonic crystals are realized by Yablonovitch [14]. Among them, a 2D photonic crystal has a more promising fabrication process than the 3D photonic crystal. It is challenging to fabricate 3D photonic crystals in small scale. Moreover, 2D photonic crystals are more convenient for integration to planer photonic integrated circuits. By tailor-made use of the optical properties of the photonic crystal researchers have demonstrated novel devices such as optical switches [15, 16], low-threshold lasers [17], add-drop filters [18].

The optical properties of the photonic crystal devices can be explained by solving classical Maxwell equation. The detailed calculations and information is given in text book of Joannopolous [4]. Here are the macroscopic Maxwell's equations:

$$\nabla . B = 0, \tag{1.1}$$

$$\nabla . D = \rho, \tag{1.2}$$

$$\nabla \times E = -\frac{\partial B}{\partial t}, \tag{1.3}$$

$$\nabla \times H = J + \frac{\partial D}{\partial t}, \tag{1.4}$$

where B is the magnetic induction, D is displacement current, E and H are the macroscopic electric and magnetic fields, ρ is the charge density, and J is the current density. Combining these equations according the following assumptions; no free charge or currents, an isotropic and low-loss medium with a frequency independent dielectric constant (ε), a magnetic permeability

(μ) close to 1, and harmonically varying field results the following equation called master equation [4],

$$\nabla \times \left(\frac{1}{\epsilon(r)} \nabla \times H(r) \right) = \left(\frac{\omega}{c} \right)^2 H(r), \qquad (1.5)$$

where c is the speed of light in vacuum, H is the magnetic field vector, r is the position vector, and ω is the angular frequency of the light. This master equation provides the information about the photonic crystal system by solving modes H(r) for the corresponding frequencies. The master equation is often written as

$$\Theta H(r) = \left(\frac{\omega}{c} \right)^2 H(r), \qquad (1.6)$$

where Θ is differential operator which takes the curl, then divides, by ε(r) and then takes the curl again [4]. Therefore, the master equation is similar to Schrodinger's equation [4]. Solving the master equation is not in the scope of this thesis. The similarities between the master equation and Schrodinger equation demonstrate that photonic crystals have analogous properties with solid crystals such as energy band structure, band gap. The ability to alter the design properties of photonic crystal enables to modify the photonic band gap properties, defect states, and controlling the light in different wavelengths. To control the light in the order of its wavelength scale made the photonic crystal important part of nanophotonic research.

In this thesis, we investigate the tuning mechanisms of photonic crystals (PhCs) building blocks. Before nanofabrication of the photonic devices, the PhCs are designed and simulated by finite-difference-time-domain method with a commercial software called CrystalWave. The photonic bandgap and transmission properties of the PhC device is studied in advance by applying 3D model into the simulations. The parameters such as refractive index, thickness of the device layer, size of the lattice (a) and size of the holes/pillar (r), crystal orientation (Γκ or ΓΜ) are assigned to the simulation (see figure 1.3).
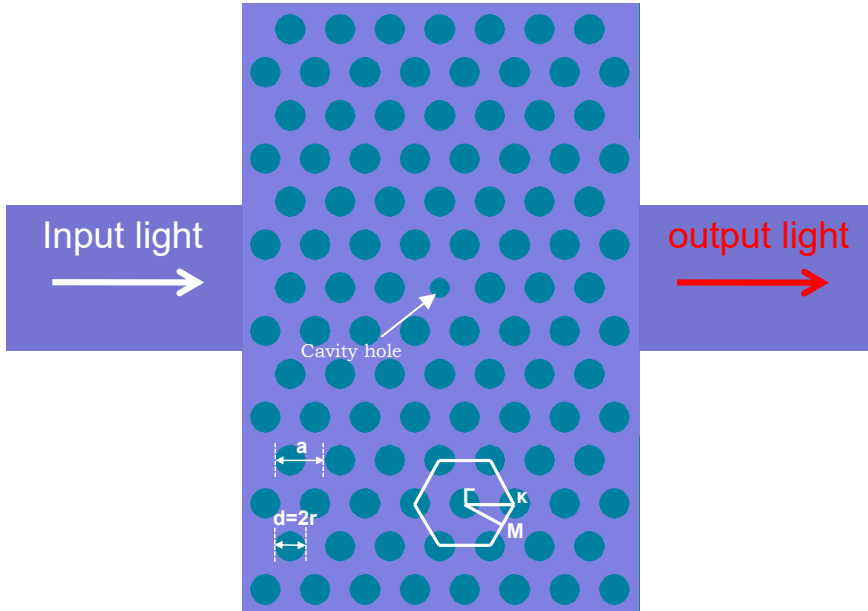
Figure 1.3. Design of the PhC device. There are ridge waveguides to couple and collect the light. In the design, *a* represents the lattice constant of PhC. The ratio r/a is the critical parameter to define the photonic band gap of the PhC. The modified centre hole is so called cavity hole that allows to transmit certain frequency of light. In this design, the configuration is called hexagonal lattice, as it is drawn inside the figure that light propagates in Γκ direction. We have used PhC crystal devices with Γκ and ΓM orientation. The detailed information can be seen in Chapter 5.

The PhCs are defined by an array of pillars or holes. In our case, an array of holes is fabricated. In order to couple the light into the PhC, and to receive the transmitted light, input and output waveguides are also needed. The whole fabrication process of PhC is performed at Kavli Nanolab facility at Delft. For the fabrication of PhCs, detailed information is given in Chapter 2. In addition to passive PhCs structures, tunable functional devices can also be fabricated. For this purpose, a defect (cavity) in the lattice of the PhC has to be created (see figure 1.3). This cavity strongly modifies the signal and allows certain wavelength within the band gap to be transmitted. The design of the cavity determines its frequency and width, which is called quality factor. Therefore, it can be tuned. There are many ways to achieve tunability in PhCs such as; thermo-optic [19, 20], electro-optic [21], mechanical tuning [22], and changing the index modulation by infilling in which are focused on and application is demonstrated in Chapter 5.

1.7 Thesis outline

This thesis investigates the design, fabrication, and application of MEMS-based microheaters and silicon photonic crystal (PhC) devices, with a focus on enabling advanced in situ transmission electron microscopy (TEM) and optical characterization techniques. Chapter 2 presents the fabrication processes of both MEMS-based microheaters and photonic crystals. The microheaters were fabricated using standard photolithography and thin-film techniques, while electron-beam lithography (EBL) was employed to define the sub-micron features of the silicon photonic crystals. Chapter 3 introduces a fabrication method called "through-membrane electron-beam lithography," which enables top-side patterning to define structures and subsequent back-side etching to locally thin down SiN membranes. This technique is used to obtain electron-transparent regions suitable for in situ TEM applications such as nanogap formation. Chapter 4 details the development of nanoreactor systems based on MEMS heaters, including closed-cell designs using O-ring chips, for conducting gas-phase experiments at high pressure and elevated temperature within the TEM. Chapter 5 focuses on the thermo-optic tuning of silicon photonic crystal cavities using elastomeric infill. It includes transmission measurements and resonance shift analysis to demonstrate wavelength tuning as a function of temperature. Finally, Chapter 6 explores the integration of cathodoluminescence (CL) spectroscopy with TEM to study diamond-based photonic crystals containing nitrogen-vacancy (NV) centers. Although the NV emission could not be conclusively detected, the experimental challenges are discussed, and suggestions for future improvements are provided.

CHAPTER 2

**Fabrication of MEMS-based heaters
and Si photonic crystals**

2.1 Introduction

This chapter covers the fabrication of the PhC devices and MEMS-based heaters. The fabrication of these two different devices involves several process steps. Photonic crystal device fabrication is based on electron-beam lithography (EBL) while MEMS-based heaters are photo lithography due to different feature size. Smallest photonic crystals features were on the order of ~100 nm while heaters were ~6 μm range. Fabrication details of these two different devices are given in the further part of the chapter.

2.2 Fabrication of microheater

The microheater is used as a sensor simultaneously for sensing the temperature during the experiments. In order to perform reliable and reproducible TEM studies with microheater, indispensable requirements are needed. First of all, microheater has to be material compatibility for fabrication process and TEM usage. Secondly, the microheater has to reach the elevated required temperatures (more example and details are given in Chapter 3-4) to investigate the properties of the specimens according to the temperature variations. Therefore, design of microheaters, choice of the metal for heating and the isolation layer and fabrication process are very important steps.

2.2.1 Design of microheaters

There are different types of TEM holders for various *in-situ* TEM studies. Therefore, in line with holder requirements we have designed several types of microheaters. In general, these microheaters are working in similar principle, and have almost the same fabrication process steps. In this thesis, the most common microheater which is so called 4-pin single heater and its fabrication process is described. Figure 2.1 shows the design of the MEMS-based 4-pin single heater chip and the coil where it works as a microheater. There are two types of heater shape, one is called spiral (figure 2.1b), and the other is flat centre (figure 2.1c). The width of the metal wire is 18 μm, and the distance between the two metal wires is 12 μm. As it is shown in figure 2.1, electron transparent windows are distributed in heater between the metal wires. In spiral heater, the temperature gradient change according to the area is higher than the flat centre one. More information related to temperature distribution is given in figure 4.12 in Chapter 4.
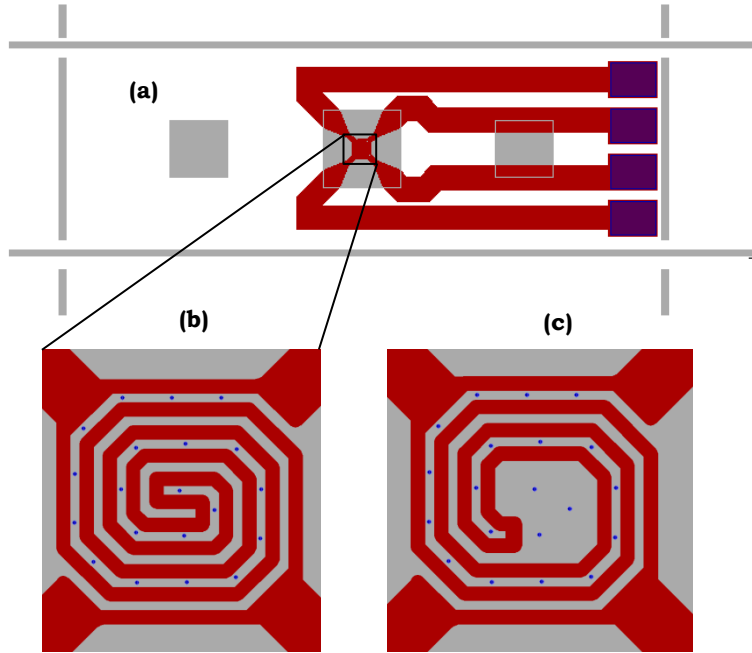
Figure 2.1. (a) Four-contact pad single heater chip design. Red represents the metal layer while purple is bond pads (b) magnified microheater design with spiral coil, (c) flat centre heater coil. Blue circles are electron-transparent SiN windows. Grey areas are 400 nm thick SiN membrane.

Another advantage of the flat centre heater is one can fabricate additional structures on the area to use microheater in different type of experiments. For this purpose, there is enough area in the centre of the microheater as shown in figure 2.1c. The application of flat centre heater can be seen in Chapter 3.

2.2.2 Material choice and fabrication process

A four-inch silicon wafer was used for fabrication of microheaters. The thickness of the wafer varies according to the type of the experiments, and the TEM holder. The wafer thickness between 300-525 µm was the most common ones to be used in our fabrication. The first step of the fabrication is defining markers on the wafer by stepper. This step is called "zero-layer". Since the fabrication includes many layer and lithography steps, markers are crucial and have to be defined in the way that connects with different steps. The

schematic of main fabrication steps of microheater is demonstrated in figure 2.2

The next step is low pressure chemical vapor deposition (LPCVD) of silicon nitride (Si-rich Si_xN_y, it will be represented as SiN in the rest of the thesis). The thickness of the first layer of LPCVD SiN is 200 nm. During this process low-stress deposition recipe is used. The importance of the stress on SiN is given in Chapter 4.

On top of the first layer of SiN, the metal layer is deposited as a heating material. According to the fabrication process, and the demands of the experiments different material can be used as a heating material. Table 2.1 shows the thermal properties of the materials which are used in our heaters. This table includes the properties of the support materials as well. Note that these are bulk properties and that as a thin film or in combination with another thin film, they can behave quite different. We use platinum (Pt) as a heater material that allows a temperature up to ~ 800 ^{0}C. Other heater materials like molybdenum (Mo) or tungsten (W) can be applied to allow a higher temperature, in particular for temperatures above 1000 ^{0}C. The applicability of the various metals depends strongly on the layer package of the membrane and the heater in the MEMS fabrication. Platinum can be embedded in SiN, while tungsten cannot due to oxidation problem during the RCA cleaning process before deposition of SiN.

Table 2.1. (a) Thermal properties of support materials, (b) heater materials. The units for thermal expansion and conductivity are ($\mu m.m^{-1}.K^{-1}$) and ($W.m^{-1}.K^{-1}$).

(a)	thermal condutivity	thermal expansion	max temperature
SiO2	1.4	0.55	1100
SiN	30	3	1000
SiC	120	4	1650
AlN	140	4.5	1850
Al2O3	35	8.4	1750
(b)	Melting Point	thermal condutivity	thermal expansion
Ta	3017	57.5	6.3
Pt	1763	72	8.8
Pd	1555	72	11.8
W	3422	173	4.5
Mo	2632	138	4.8

In our heaters, platinum (Pt) is used as a heating metal. Tantalum (Ta) is used for adhesion layer, and the thickness of the metals are 20 nm (Ta) and

180 nm (Pt). The metals are sputtered with a TCOathy sputtering machine at the Mesa Institute in Twente. After sputtering 200 nm thick metal layer, the next step is preparing wafer for optical lithography. An Oir 907-17 photoresist is used to coat the wafer with a spin rate of 4000 rpm, and baked in hotplate at 95 ^{0}C for 90 seconds. The defined pattern is transferred to the resist by using optical lithography EVG620 mask aligner. In this process, dark field mask (the area is exposed is not the heater structure) is used, and after development of photo resist the area exposed is etched by Ion Beam Etching (IBE) Oxfordi300. The remained photoresist is stripped by applying O_2 plasma. The sputtering and etching of metal layer are more reliable than the e-beam evaporator and the lift-off technique. Structure of the heater, and the edges of metal lines are critical for the temperature adjustment and the stability of the heater. During the depositing of metal layers by e-beam evaporator we have been faced with a problem such as peeling of the metal layer, leads to bad lift-off process result later. Therefore, we have chosen the sputtering and etching of metal layer. The whole fabrication of the metal layer is carried out at Mesa Institute (Twente), since the required devices for sputtering and etching of the Pt were not present at Kavli Nanolab Delft. Deposition and etching of metal layer are demonstrated in figure 2.2b.

After defining the heater layer, next step is the cleaning of the wafer with RCA1 and RCA2 solutions to prepare the wafer for second step LPCVD of 200 nm thick SiN (figure 2.2c). The heater material Pt is embedded in 400 nm thick SiN after second step of LPCVD. The next fabrication step is defining the electron-transparent windows. Since optical lithography is used in fabrication process, photo resist AZ5214 E with a spin rate of 5000 rpm/min is applied on wafer and baked at 90 ^{0}C for one minute that results with a resist thickness of ~1.4 μm. The diameter of 6 μm holes are patterned on the photo resist by optical lithography EVG620 mask aligner. The chemical MF320 developer is used to develop the pattern, and DI is used as stopper. After development, the pattern is transferred to SiN up to Si substrate by reactive ion etching (RIE) using a plasma of CHF_3 and Ar and photo resist is stripped by O_2 plasma (seen in figure 2.2d).

For in situ TEM experiments the most critical part of MEMS device is the electron-transparent viewing windows. These windows have to be contamination free, stable, and as thin as possible. The required thickness of SiN for the most of the experiments is ~20 nm. The detailed information related to electron-transparent windows is given in the next part of this chapter. For electrical connection of the microheater, there are bond pads in the design (figure 2.1). Similar fabrication step for opening holes is also applied for opening the bond pads. The pattern is defined by optical lithography and

development. After development, around 220 nm thick SiN is etched up to metal layer to define the bond pads (see Figure 2.1 a).
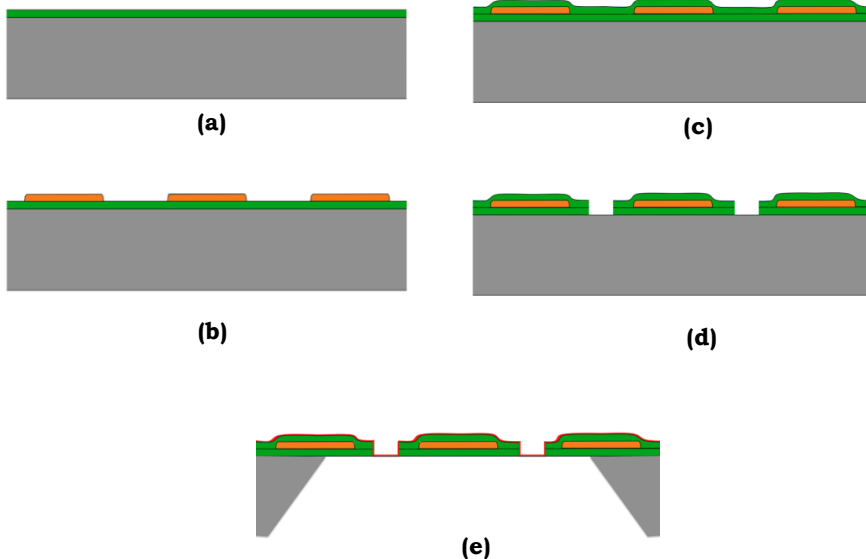
Figure 2.2. Schematic of main fabrication step of microheater. (a) 200 nm thick LPCVD SiN, (b) Ta/Pt metal layer after sputtering and etching, (c) second step of LPCVD of 200 nm thick SiN, (d) opening of electron-transparent windows, (e) completed fabrication after LPCVD of 20 nm thick SiN and obtaining membrane windows by KOH etching of silicon. (grey: Si, green: LPCVD SiN for big membrane, orange: Ta/Pt, red: LPCVD SiN for electron-transparent windows).

The next fabrication step is defining the membrane windows on the back side of the wafer. For this process, the wafer is spin coated with the same photoresist. The recipe which is applied for defining the holes is also applied for the membrane windows. The SiN is etched up to silicon substrate by RIE using plasma of CHF_3 and Ar. After stripping the photoresist by O_2 plasma, the wafer is dipped into 30% potassium hydroxide (KOH) solution where the etch rate of silicon is ~100 μm at 85 ^{0}C degrees. Depending on the thickness of the substrate the wafer is kept inside the KOH solution till obtaining the SiN membrane windows. The KOH solution is etching SiN with a very slow etch rate which is 1.5 nm/hour that leads to intact electron-transparent windows.

2.2.3 Electron transparent windows

Electron transparent windows are one of the most critical parts of the microheater for its applications in TEM studies. Figure 2.3 shows the optical image of the spiral microheater, and the magnified area that includes the electron transparent windows. These windows work as an alternative of classical copper mesh coated with holey carbon. Electron transparent windows enable to run in-situ TEM studies, and lead to important improvements and developments in the field.
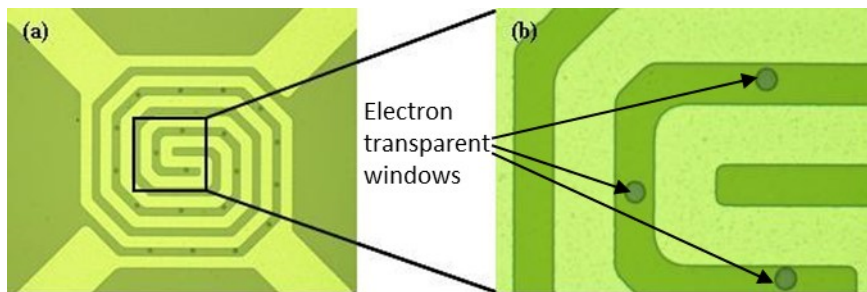
Figure 2.3. (a) Optical images of the centre of the MEMS-based heater with an embedded Pt wire for local heating with four connections, (b) electron-transparent windows with a diameter of 6 µm and 20 nm thick SiN.

Obtaining an image from TEM study is depending on the interaction between the electron beam and the sample under study. Hence, the material used as an electron transparent window should have low density, lowest roughness, lowest possible thickness. Moreover, the windows material should be amorphous to provide plain background for TEM image. The typical thickness of the window material is less than 50 nm. Mechanical strength of the windows depends on the shape and thickness of the material. Research on LPCVD SiN windows demonstrate that thinner windows up to 15 nm have higher mechanical strength than the thicker ones [23] . In addition, electron transparent windows have to be resistance to the electron-beam. Due to high energy and dose of the electron beam, the windows might be thinned down and holes can be formed locally during the experiments. For certain type of experiments such as; nanoreactors (see in Chapter 4), this is unwanted situation that might cause leakage to the chamber of the microscope.

Electron transparent windows have to be able to withstand the high temperatures that microheater can operate. Another important parameter is having low roughness. This property is desirable to obtain TEM images with better contrast. Furthermore, uniform and flat windows exibit greater

mechanical strength, including under elevated temperature conditions. In order to investigate the surface properties, a test wafer is used during the LPCVD SiN for electron transparent windows. Atomic-force-microscopy (AFM) is used to check the surface properties of the SiN. As it can be seen in figure 2.4, the AFM results show that the root mean square (RMS) surface roughness is ~0.48 nm which is in the limit of high-quality surface for semiconductor process technology.

In conclusion, in order to perform their tasks, electron transparent windows have to satisfy aforementioned requirements such as; electron transparency, mechanical strength, electron-beam resistance, and resistance to heat.
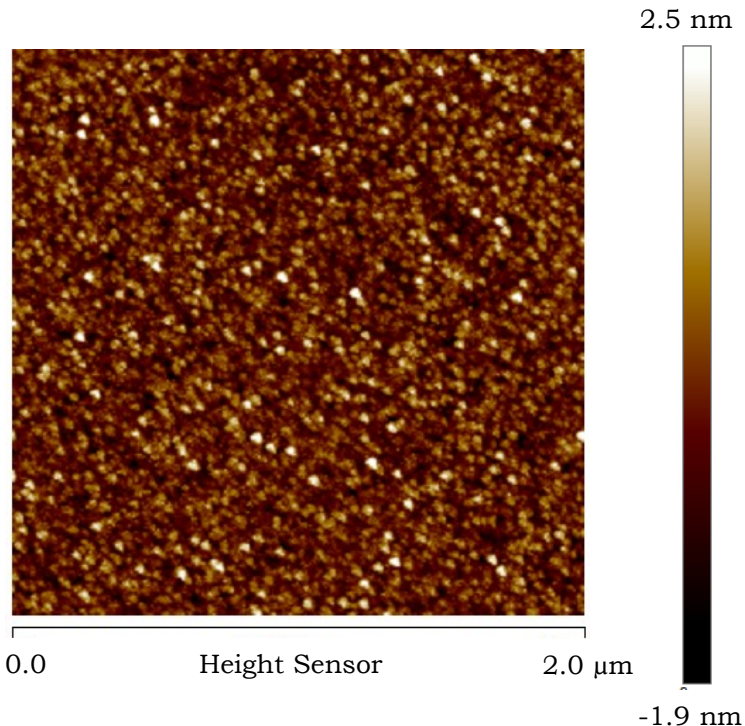

Figure 2.4. Results of AFM measurement of 20 nm thick LPCVD SiN. The RMS surface roughness value is 0.483 nm which might be influenced by the AFM tip shape indicated by triangle form of the grains.

2.2.4 Applications of microheater in situ TEM studies

MEMS-based heaters are presently used in situ TEM studies for different purposes and applications. They are used in morphological transformation of gold nanoparticles [3], sculpting of graphene [24], and thermal stability of nanoparticles [25]. A spin-off company Denssolution [26] at Delft is producing and supplying the microheaters which are initially developed in our research group to the other universities and research institutes all around the world which demonstrates the success and applications of the microheaters.

In this thesis we demonstrated the application of microheater in Chapter 3 and Chapter 4. In Chapter 3, microheater is used to study the properties of gold nano-bridges in real time with respect to the temperature changes, and application is presented in Chapter 3 including applied special fabrication technique for SiN membrane. In addition, application of microheater in gas nanoreactor studies explained in detailed way in Chapter 4. Microheater performed very well in several studies related to nanoreactor that lead to obtain remarkable results [27, 28].

2.3   Fabrication of PhC devices

Photonic devices have high potential of future applications for photonic integrated circuits. Fabrication technique for photonic crystal is CMOS compatible that includes main steps like electron-beam lithography (EBL) and plasma etching. However, EBL technology does not allow mass production today due to processing time. In the near future, fabrication of photonic devices with inline technology might be possible with the development of EBL technology.

2.3.1 Patterning of PhCs by E-beam lithography

The EBL is the most common used technique to fabricate sub-micron PhC devices. The resolution and accuracy of EBL is higher than the optical lithography. The beam used to transfer the pattern of PhC on the chips is on the order of few nanometres. The electrons are focused on the surface of the sample and then scanned over the area that shall be exposed. In our case, the system used for PhC fabrication is a Leica 5000+. The acceleration voltage of the e-beam is 100kV. A scanning step-size of 2.5 nm is used for writing the pattern.

The photonic crystals are fabricated using silicon-on-insulator (SOI) material as basic substrate. The silicon device layer of SOI is 220 nm thick.

Buried oxide (SiO$_2$) layer is 2 µm thick under the top silicon layer, while the total thickness of the wafer is 760 µm thick silicon substrate. The SOI wafers used for this thesis were 8 inches in diameter. The top silicon layer is the optical guiding layer due to its high refractive index value of 3.48, and the buried oxide layer is used to prevent leakage of optical modes to the substrate layer. The first step of the fabrication is to get small SOI pieces for fabrication. Therefore, the wafer is coated with photo resist to protect the device layer before dicing, and it is diced in to small pieces with a dimension of 14x14 mm, which makes it easy to control during the fabrication process such as spin coating (uniform resist), e-beam writing (holder availability), etching (easy to handle). The final size of the chips that we use is 14x3 mm, which fits our measurement setup. The detailed information is given in further section 2.3.4. After dicing the sample, the protection layer is removed in acetone. Finally, the samples are cleaned with nitric acid (HNO$_3$) in an ultrasonic bath to get rid of all carbon contamination, and dirt caused by dicing.

After cleaning the sample, the next step is the spin coating of resist. Diluted ZEP 520A resist is used to obtain 120 nm thick resist layer with a spin rate of 4000 rpm. The sample is kept on hot plate for 20 minutes at 175 ^{0}C to bake the resist. The thickness and the homogeneity of the resist is very important parameter for the quality of the pattern. Therefore, this spin coating recipe is obtained after several test. During the writing process, the focused electron beam scans and bombards the resist with electrons at the specified area. Depending to resist type, this area can be directly the pattern (positive resist) or surrounding of the pattern (negative resist). In our case, resist is positive. Hence, electrons are focused to expose the air-based areas such as PhC holes, and trenches of waveguides.

After e-beam lithography, the next step is to develop the resist i.e. to remove it from the exposed areas. First, the sample is kept in N-Amyl Acetate for 90 seconds. N-Amyle Acetate also etches the unexposed regions of the resist however with a low etch rate. Therefore, the development process is stopped by 90% Methyl Isobutyl Ketone (MIBK) 10% Isoproponol (IPA) solution after 30 seconds. In the last step, the sample is rinsed in IPA and blown dry with nitrogen gas.
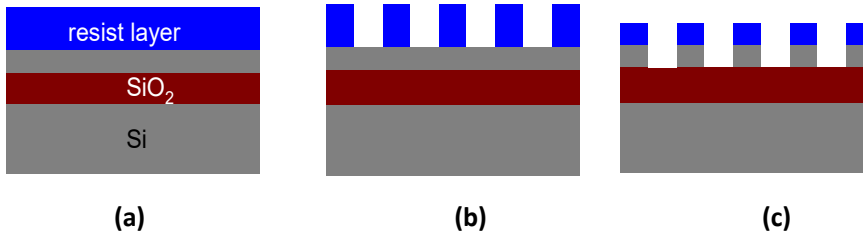
Figure 2.5. Schematic representation of fabrication process of PhC. (a) Resist spinning, (b) e-beam lithography and development, (c) dry-etching of silicon.

2.3.2 Dry-etching PhCs holes

Fabrication of PhCs is carried out based on the design and simulation of the devices. Hence, the size and shape of the holes must be as accurate as possible to the design to match the theoretical calculations. The PhCs holes have to be straight and smooth without tapering, and the sizes have to be close to the value of the design. When the fabricated sizes are different than the design, these values are added the simulations before running optical experiments. After e-beam writing and development the next step is transferring the pattern into the device layer. The system used during the dry etching is an Alcatel AMS 100 Cryo system. This device is an Inductively Coupled Plasma (ICP) system which is usable for etching silicon and some kind of metals. The etch rate of silicon is comparably higher than that of other dry-etching systems. The ICP system has two power sources which are radio frequency (RF) and low frequency (LF) source. The RF source is used to create a high-density plasma, while the LF source is used to control the energy of the etching ions. The substrate temperature is selected as -120 ^{0}C to deactivate the chemical reactions of fluorine radicals with silicon. The plasma is a mixture of 3:1 of SF_6 to O_2. Here, the SF_6 plays the role of etchant, while O_2 is used for passivation of the silicon surface. The etching time of a 220 nm thick silicon layer is 36 -40 s.

A resist thickness of 120 nm is suitable as a mask for silicon etching by ICP. The low temperature of the substrate is decreasing the etch rate of the resist thus increasing the selectivity. After etching of silicon, the next step is removal of resist layer by using PRS 3000 (positive resist spinner) at 75 ^{0}C for one hour. After removal of resist, the next step is to cleave the 14x14 mm chip to get a cleaved facet waveguide to couple the light in. In order to protect the silicon device layer during the cleaving, a photo resist is spin-coated. The SOI substrate is ~760 µm thick. There are two methods to prepare the substrate for cleaving: substrate thinning, or pre-cut from back of substrate. The first

technique is more complicated since it includes manual polishing. Second method includes sawing the substrate from the back side to around 500 μm in depth that enables the cleaving. The samples are cleaved through waveguides and coupling facets are obtained. Later, the samples are cleaned in acetone to remove the photo resist. The scanning electron microscope (SEM) micrograph shows the cleaved facet waveguide in figure 2.6, which is discussed in detail in the next section.
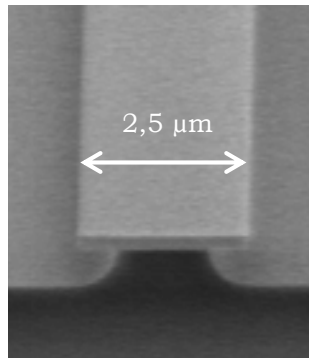
Figure 2.6. Cleaved faced of the waveguide after wet etching of 350 nm oxide layer in buffered hydrofluoric acid (see section 2.3.3).

2.3.3 Wet etching of SiO2

After etching and resist stripping, the PhC device layer is resting on the buried oxide layer. In this stage, the upper cladding layer is air, and lower cladding is buried silicon dioxide. In order to increase the refractive index contrast and the coupling efficiency to the PhC, the silicon oxide underneath the PhC needs to be partially removed by using wet-etching technique. Buffered hydrofluoric (BHF) acid is used due to its high selectivity etching rate for SiO_2. The solution has an etching rate of 70 nm/min for SiO_2. The chip is kept 5 min in BHF to remove 350 nm of oxide layer. The width of the silicon ridge waveguides is 2.5 μm. The wet-etching process removes around 700 nm oxide underneath the waveguide that is still able to support with a width of 1800 nm which is demonstrated in figure 2.6. Figures 2.7 (a-b) show the PhC device before wet etching, and figures 2.7 (c-d) show the membrane PhC after wet etching. The sample is more fragile and susceptible to deformation due to having membrane device. Therefore, after this step cleaning and handling of the sample is very critical. There is a big chance of breakdown, or buckling of membrane when the device is cleaned in an ultrasonic bath, or accidentally dropped during the process.
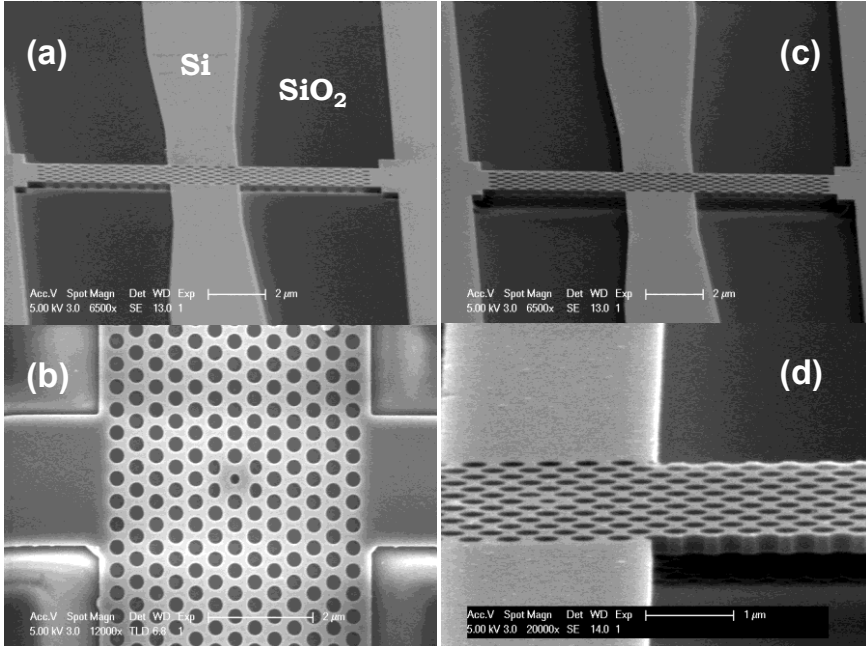
Figure 2.7. (a) and (b) are the SEM images of PhC before wet etching of SiO_2 while (c) and (d) are after removal of 350 nm oxide by BHF. The SEM images of PhC in (b) and (d) are individually different devices. In order to show the process better quality images are chosen.

2.3.4 Transmission setup

A schematic overview of the optical transmission setup for characterization of fabricated PhC devices is demonstrated in figure 2.8. This setup is called "end-fire" due to coupling occurs from the cleaved facet of the ridge waveguides (RWGs) by an external light source. In our experiments, a supercontinuum light source (SC400 Fianium) is used. The broadband output ranges from deep blue to near-infrared (400-1750 nm). Silicon absorbs wavelengths shorter than 1100 nm. Therefore, additional setup is built [29] to select the wavelength between 1300-1750 nm that enables to work with silicon PhC and to view the whole band spectrum of it. Figure 2.8 illustration that the light is coupled to PhC by objective and the signal from sample is collected by objective as well. The signal is selected by pinhole then it is guided to IR detector or optical spectrum analyser (OSA) by fibre coupling depending on the source type. For tuning laser, we used IR detector and OSA for white light

source. Splitter and thermal camera are used to align the sample on the axis of the light.
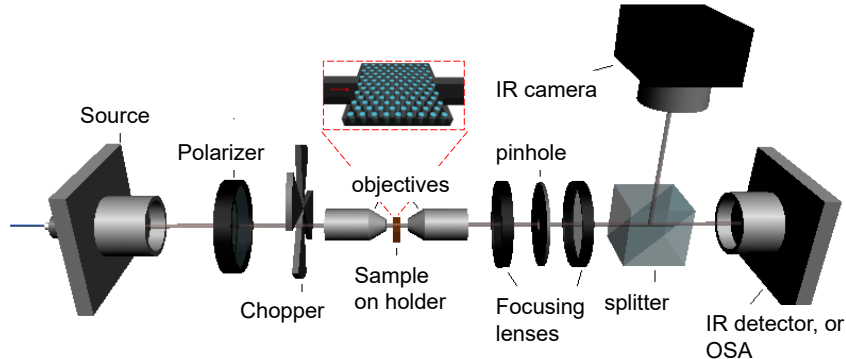
The light source is coupled to the PhC device by an objective having a numerical aperture NA=0.65 that offers a converging beam waist of 4 µm which is almost twice as wide as RWGs. This difference in width between the RWG and the beam waist causes around 5dB losses at the coupling. Therefore, the total loss of light for in-out-coupling is 10dB [31]. The transmitted light from the PhC device is collected by an output objective, and collimated beam is directed to optical spectrum analyser (OSA). The performed experiments with this setup and the PhCs devices and the obtained results are discussed in Chapter 3.

2.4 Conclusions

In conclusion, fabrication process steps such as design, lithography, etching, deposition are explained in this chapter with details. In order to have working MEMS-based heaters and photonic crystals, process steps of the fabrication are playing key roles which can help to lead successful experiments. In chapter 3, 4, 5 and 6 application of these two devices MEMS-based heaters and photonic crystals will be demonstrated.

CHAPTER 3

Electron-beam lithography technique for SiN membrane applications

3.1 Introduction

Micro-electro-mechanical system (MEMS) is a technology where mechanical and electronic systems are miniaturized by the techniques of microfabrication. MEMS devices can be simple with stable elements, or can be very complex electromechanical systems with moving elements under the control of integrated microelectronic components. MEMS devices such as micro-sensors and micro-actuators have possible applications in communication [32], medicine and biology [33].

MEMS-based devices are also used in transmission electron microscopy (TEM) studies. In MEMS-based heating holders, the heater is connected to four electrical connections that allow measurement of the resistance for temperature determination and heating. The big advantage of these heaters is that the heat produced is much lower than with the conventional heating holders (about 100 times less) [34]. MEMS-based heaters are presently used for *in situ* TEM studies, such as morphological transformations of gold nanoparticles [3], sculpting of graphene [24], gas nanoreactors [28], thermal stability of nanoparticles [25].

Our MEMS-based heaters and biasing devices are fabricated on a silicon (Si) substrate. In order to obtain electron transparency, we need to realise amorphous "windows" of less than 20 nm thickness. Mostly we use silicon nitride (SiN) for this purpose, but other materials such as SiO_2, SiC, Al_2O_3 can be also used. The requirement to the SiN windows is that they have to be amorphous, have a uniform thickness and the target thickness of a few nanometres. In our process it is done by etching of thick SiN membranes up to silicon followed by a deposition of thin SiN layer. SiN growth can be controlled with more accuracy than SiN etching. However, this procedure has one big disadvantage: the thin windows are located on the bottom side of the thick SiN membrane (see Figure 3.1), meaning that the SiN window is in a deep hole compare to the top surface of the membrane. For example, such deep-hole shaped windows cannot be used for liquid *in situ* experiments. Thus, a local removal of SiN material from the backside is needed. A similar requirement for backside material removal is occurred for biasing *in situ* TEM experiments, in which the thin SiN membrane is only needed at certain locations, for example, where a metal nanobridge is fabricated and where we would like to remove the SiN locally from underneath the part of nanobridge. In this geometry, the membrane is still strong enough to withstand mechanical forces, such as deformation due to Joule heating of the bridge, whereas the SiN is completely or partially removed below the nanobridge.
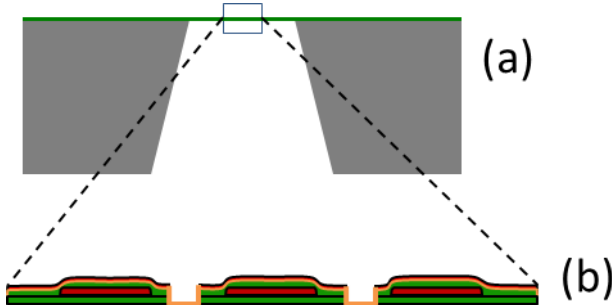
Figure 3.1. (a) Full size of heater chips including the thick (green) and thin SiN membranes and also platinum coils as a heater material (red), (b) magnified area of the membrane with thin electron transparent viewing windows (orange line, ~20 nm) that are located on the bottom side of the thick SiN membrane.

Performing a backside lithography is impossible with the conventional set-up of lithography systems with a mask by using an electron beam lithography, since the backside of the membrane is at the bottom of a KOH-etched silicon wafer 300 to 500 micron deep hole, whereas the mask should be in contact with the surface to be patterned and the lens of the electron beam lithography of the electron beam lithography requires a distance to the sample of at most 100 μm, and can be considered as the focus problem.

In this Chapter we show that one can expose an electron beam resist, which is spray coated on the backside of the SiN window, with an electron beam from the topside of the SiN membrane and, thus, through the SiN membrane and the structure on top of this membrane. In this geometry the focus problem is solved, since both a mask, as well as the lens of the EBPG can be brought in close enough distance. We give several examples and applications to of this approach in results part of this chapter.

3.2 Design and Fabrication

Fabrication of the MEMS-based heaters consists of different main steps such as deposition, lithography, and dry etching which is discussed in detailed in Chapter 2 of this thesis. In brief, we start with 300-500 μm thick silicon wafer and deposit 200 nm thick SiN with low pressure chemical vapour deposition (LPCVD) as an isolation layer between the metal and Si substrate. Heaters are made of Tantalum (Ta)/Platinum (Pt) metal layer with a thickness of ~ 20/180 nm which is deposited by electron beam evaporation technique and etched by ion etching. The second step of LPCVD SiN is performed and the heater is embedded in total 400 nm thick SiN. The SiN membrane

structures are obtained with KOH etching of silicon. Later the wafer is diced and cleaned in order to get single chips.

Next electron beam resist (PMMA:PGMEA:MEK) is sprayed on the backside of the chips with an EVG101 spray coater. The main challenge of this method is to obtain uniform resist layer on the backside of SiN membranes due to the depth 300-500 μm of the KOH-etched "hole" in the Si substrate (see schematic Figure 3.2). After several spray coating tests, the best uniformity obtained with 7 layer of spray coating of resist with a spin rate of 500 rpm, and cured on hot plate at 175 ^{0}C after coating each layer. This recipe results in a resist with a thickness of around ~ 12 μm PMMA. The pattern is written in a resist by excitation from the top site of the chip by 100kV penetrated electrons through the 400 nm thick SiN membrane with a Leica 5000+ e-beam system. After resist development the pattern is transferred to the SiN layer using reactive ion etching in Argon (Ar) and CHF$_3$-based plasma with anisotropic etching from back side of the chip. The etching rate and time are critical to obtain required thickness of the SiN for thinning down process.
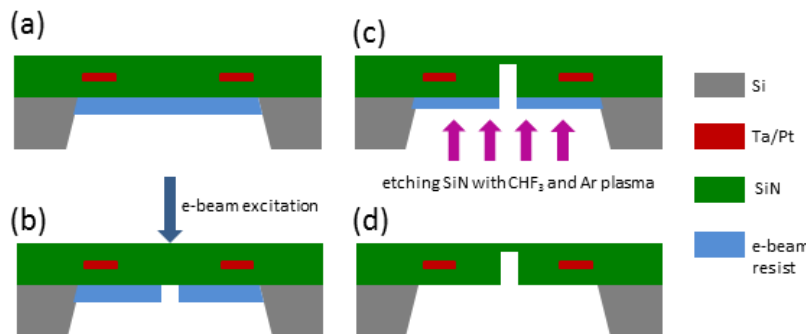
Figure 3.2. Schematic of the fabrication process of back side opening by excitation from top. (a) Spray coating of e-beam resist (PMMA:PGMEA:MEK) from the back side of the chip, (b) e-beam lithography and development, (c) etching of the SiN from back by reactive ion etching and thinning down up to required thickness, (d) after removal of the resist by PRS300 (positive resist stripper).

In order to be sure about the thickness, controlled etching method is followed, which is checking the colour the of SiN membrane by optical microscope, and estimating the thickness according to LPCVD SiN colour chart. After etching, the resist is removed by PRS 3000 (positive resist remover) and oxygen plasma. Described above fabrication steps are a part of the main removal of SiN from the back side. According to application of this technique, additional fabrication steps might be required. The applications are discussed in next section of this Chapter.

3.3   Applications

The back side lithography is a crucial technique to thin down a SiN membrane at certain locations. In order to perform this accurately, Pt markers are used for alignment with an accuracy of 20 nm. The resist is exposed on to the back side of the chip with high dose of electrons having beam step size of 150nm. In addition to these technical achievements the application of the back side lithography is applied to experiments related to TEM studies such as investigation of electro migration of gold (Au) and also related to biological application as DNA translocations. The electro migration application is explained in the next section of this chapter. The second application, DNA translocation is explained in details at Nekluyodova et.al. [35].

3.3.1 E-beam lithography technique through SiN membrane for in situ TEM research

In this application example we use the back side lithography technique to fabricate metallic nanobridges with a configuration close to free standing on top of heating chips in order to subsequently shape them into metallic nanoelectrodes separated with a nanogap of several nanometres (1-10 nm) by in situ electrical measurements in TEM. The interest to fabrication of these nanogap electrodes on top of heaters is based on the feasibility of performing TEM characterization of nano species trapped in between the nanoelectrodes such as low-dimensional nanocrystals, phase change nanoparticles or individual molecules, while applying heating, voltage or both voltage and heating simultaneously. Nanoelectrodes can be fabricated by different techniques, such as mechanical break junction [36], electron-beam lithography [37], electromigration [38] and shadow mask evaporation technique [39]. In most cases the metal structure is on top of a SiN substrate, and the electrical measurements are not hindered by the substrate. However, for structural characterization of nanogap formation or nanocrystal transformation while applying electrical or heating conditions, TEM is the best technique, but it requires preferably a free-standing metal nanobridge or at most a very thin SiN-substrate that is not thicker than a few nanometers, because a thick support leads to a too noisy background, which does not allow atomic resolution imaging of the gap and species (like molecules or small particles) in the gap. An additional advantage to use heating chips as a base for other following fabrication processes is that it allows to prevent the e-beam-induced carbon contamination while imaging with TEM by heating up to 120-140°C during the in-situ visualization. Here we present a formation of nanogap electrode using feedback controlled electromigration (FCE) technique in situ TEM in gold nanobridges fabricated onto MEMS-based heaters. FCE is a method in which an electrical current is applied to gradually narrow the

metallic bridge through electromigration. The electrical resistance is monitored in real time, and when it begins to increase, which indicates that the bridge is thinning, the current is automatically reduced by a feedback loop to avoid uncontrolled breakage. This enables precise control over the formation of nanogaps with separations in the range of 1–10 nm [40, 41].

A schematic illustration of MEMS-based heater with a flat 400 nm thick SiN centre is shown in Figure 3.3 (a). In order to fabricate thin SiN windows, the backside lithography technique was applied as described in Section 5.2 of this Chapter and a pattern of SiN windows with a diameter of 5 µm was produced in the centre of Pt heating coil using e-beam writing through the membrane. After development of e-beam resist, the pattern was transferred to SiN layer and RIE was applied from the backside of MEMS-based heaters to thin down this patterned area of SiN membrane to 50 nm. Schematically it is shown in Figure 3.3 (b). Gold bridges with a length of 700 nm, width of 250 nm and 20 nm-thick were produced on top of 50 nm thick SiN area using e-beam lithography followed by electron beam evaporation from the gold source. Contact pads to bridges were placed by the second step of e-beam lithography followed by the metal evaporation of a 250 nm thick layer of Au on a 5 nm-thick adhesion layer of Cr. The configuration of fabricated device is schematically presented in Figure 3.3 (c). In order to reduce the thickness of SiN in the location of Au nanobridge, SiN was etched from the backside of MEMS-based heater using RIE technique. Since the thickness of SiN under the nanobridge is 50 nm, we used a RIE recipe with CHF_3 and O_2 gases with a flow ratio of 50 sscm and 2.5 sscm, respectively.

The MEMS-based heater with the gold nanobridge was mounted into a custom-built TEM holder equipped with six electrical contacts, enabling the combination of heating and electrical measurements. Four of the contacts are typically used to supply current to the integrated spiral heater through a heating controller, while the remaining two contacts are used for electrical measurements across the nanobridge. To calibrate the temperature response of the spiral heater, it was gradually heated in a separate setup, and a pyrometer was used to measure the surface temperature based on the emitted black-body radiation. The measured temperature values were then correlated with the corresponding electrical resistance or input power to generate a calibration curve, which was later used during in situ TEM experiments to estimate the actual temperature of the heater.
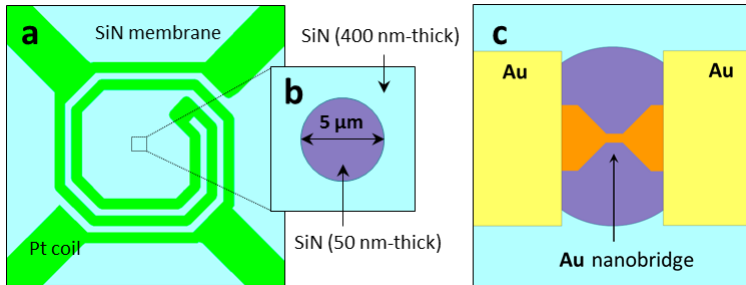
Figure 3.3. (a) Schematic illustration of MEMS-based heater with a flat 400-nm thick SiN centre. Pt heating coil (green) and 400-nm-thick SiN (blue). (b) Central part of the heating coil showing a 50-nm-thick SiN window with 5 µm in diameter (purple). (c) The configuration of fabricated device onto 50-nm-thick SiN window containing 20-nm-thick Au nanobridge (orange) and 200-nm-thick gold contact pads (yellow).

The FCE process in Au nanobridges was investigated by in situ TEM using a FEI Titan microscope operating at 300 keV. In FCE mode the bridge conductance is constantly monitored while the voltage is ramping up. If there is a sudden decrease in conductance, the FCE mechanism reduces the voltage to zero or to a lower value. The process starts again after a new reference conductance is defined. The program stops when a pre-defined conductance value is reached. To avoid the influence of carbon contamination on bridge resistance forming during illumination by electron beam the electromigration experiments were performed at T=120°C. It results in zero conductivity value after the bridge breaks.

Figure 3.4 shows snapshots of a typical in situ TEM movie recorded during the experiment on the nanogap formation in gold nanobridges by electromigration. The initial view of the bridge before the electrical measurements is shown in Figure 3.4 (a). When the current is passed through the bridge, we observe a slight grain growth prior to electromigration. The grain growth is occurring due to the temperature rise in the bridge caused by current-induced Joule-heating. In Figure 3.4 (b) the bridge starts to thin close to the cathode side forming a bottleneck. When the electromigration is observed, the current density is about 7×10^7 A/cm2). In the last stage of electromigration a tiny constriction forms as shown in Figure 3.4 (c) and the following narrowing is continued at low voltage values which is around 200 mV. As a result, a nanogap electrode is produced (Figure 3.4 (d)). The initial size of the formed nanogap is about 2-3 nm and it increases to 5-6 nm during continuous illumination by the electron beam within several seconds. Figure 3.4 (e) is TEM image acquired at higher magnification and shows the final configuration of the nanogap with the size of 5.26 nm which does not change at least after several minutes of electron beam irradiation. At the moment

when the nanogap electrode is initially formed, the tips of the electrodes are sharp. However, after several seconds when the gap size increases, the shape of the tips of electrodes become smoother which is likely due to surface tension of Au. This observation is in agreement with the previous reports of Zandbergen et al. [42] on continued relaxation of Au nanogaps formed by electron beam bombardment even after the intense irradiation is completed, also with the report of Strachan et al. [43] on the evolution of Au nanogap electrodes. A typical I–V curve of FCE process in Au nanobridges is shown in Figure 3.4 (f).
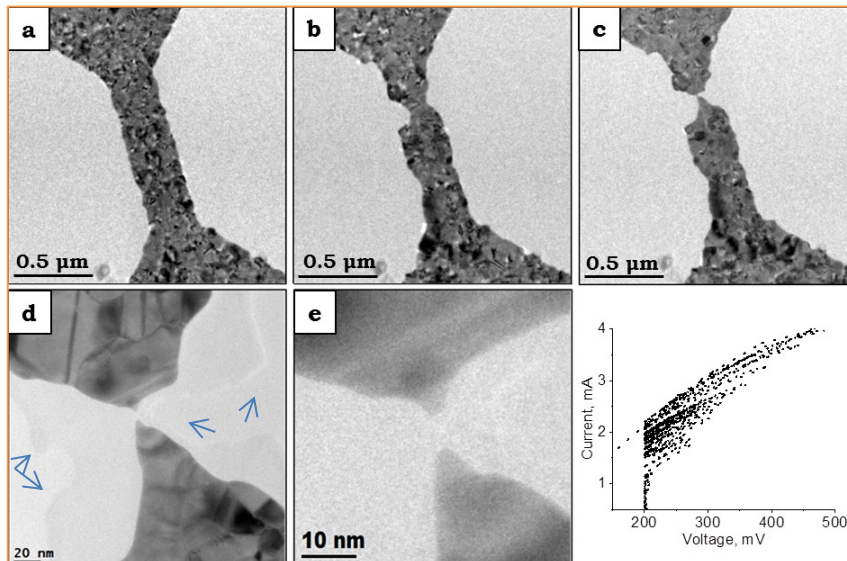
Figure 3.4. Snapshots taken from in situ TEM movie recorded during FBC electromigration process in gold nanobridge. (a) The original gold bridge. (b)-(c) TEM images showing formation of nanogap in gold bridge during FBC electromigration. (d) TEM image acquired after bridge breakdown; arrows indicate the areas with a very thin (1-3 nm) SiN layer. (e) Enlarged area of (d) showing gold electrodes separated with 5.26 nm nanogap. (f) A current-voltage curve of FCE electromigration process.

As can be seen in Figure 3.4 (d), just a very thin layer of SiN remains around the nanogap. According to standard fabrication methods of nanogaps on top of SiN membranes with the thicknesses of 100 nm [44], our technique allows to fabricate nanogap electrodes with very thin SiN layer beneath it (1-3 nm). These devices can be used for further experiments as synchronous electrical, heating and structural characterization of low-dimensional systems such as nanocrystals and individual molecules.

3.4 Discussion and Conclusions

We have shown that it is possible to expose electron beam resist through a thin membrane including thin metal lines. This opens the manufacturing for a new type of geometry in which one can control the flatness of the top side of the thin film membrane at certain locations. This is important for applications such as electromigration in metals and semiconductors. Another successful application of this technique is reducing the noise for DNA translocation experiments where the SiN windows have to be on top side of the membrane. The DNA translocation experiments are not shared in this thesis while details are explained in Neklyudova et.al [35], which was part of collaboration study with Bionanosicence Department at TU Delft. Therefore, a new fabrication technique is used which is so called back side lithography with exposure from top that enables to obtain thin SiN viewing windows on the top of the membrane which is presented the fabrication part of this article. The presented application in this chapter and DNA translocation experiments are the frontier projects that we have applied this new fabrication technique. Moreover, having thin SiN electron transparent window on the top of the membrane has advantages on in situ liquid cell studies, environmental studies, battery studies of some materials and so on, since it offers flat surface on the top that enables smooth liquid flow for liquid cell studies and controllable lift off materials after deposition. Compared to optical lithography, electron beam lithography allows one to obtain smaller structures with a high accuracy of the required dimensions. The back side lithography fabrication and applications in the nanogap electrode formation in gold by FCE electromigration technique and DNA translocation are promising evidence for the future possible applications.

CHAPTER 4

Closed cell systems for in situ TEM with gas environments

4.1 Introduction

TEM experiments are almost always performed with a 10^{-7} mbar environment around the specimen. This has to be done because the electrons have such a strong interaction with matter (and thus also gas molecules) that even a low gas pressure in the electron microscope results in a strong blurring of the TEM image. Over the last two decades, the development of environmental TEMs (ETEM) has made it possible to increase the pressure around the specimen while maintaining an acceptable vacuum in other parts of the TEM. This was realized by adding extra pumps and pumping apertures. A disadvantage is that the maximum pressure around the specimen for high-resolution imaging is about 10 mbar. This limitation is caused by the geometries in an ETEM. More than a decade ago, we realized that in order to do experiments at realistic pressures, it was necessary to develop a system with a shorter gas column. The gas column in an ETEM is about 10 mm and had to be shortened by several orders of magnitude to allow pressures of 1 bar and more. Practically, this shortening can be achieved best by developing a small microreactor or nanoreactor (NR) based on semiconductor production techniques. Figure 4.1 shows the design of the first type of NR [45]. Several prototype NRs have been designed and manufactured, which allowed getting atomic resolution images at 1 bar gas pressure and 700 ^{0}C.
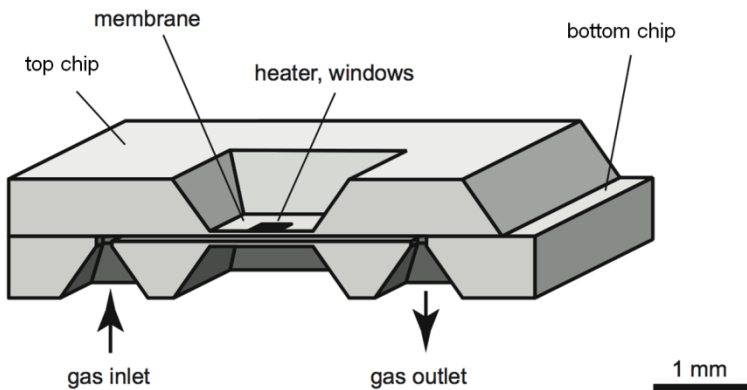

Figure 4.1. Schematic presentation of a nanoreactor composed of two chips [46].

4.2 The nanoreactor developments in Delft

The research in Delft employing MEMS to create a 1 bar environment around the sample started in 2001 with the use of a sandwich nanoreactor in which two MEMS-processed chips were aligned with respect to each other and fixed with a two-component glue. This type of ensemble was successfully used for various in situ experiments at 1 bar [45]. However, when we tried to use these glued NRs more routinely, it turned out that carbon contamination (C-contamination), ease of use (including making it airtight), and the yield were major bottlenecks. Various routes have been explored to solve the C-contamination issue: (1) finding an organic-based glue that does not outgas, (2) using an inorganic glue (water glass) [47], (3) using a Viton O-ring to make an airtight connection between the bottom and top chip, (4) making the NR as one complete chip [48]. Note that apart from the NR, contamination can also originate from hydrocarbon impurities in the rest of the gas system (in the holder and in the gas supply system). Several organic-based glues have been tried out, but we could not find a glue that did not result in C-contamination. Alternatively, water glass (a solution of sodium metasilicate, Na_2SiO_3) has been used as glue. Being inorganic, it was possible to achieve C-contamination-free experiments several times, but achieving airtightness with this glue has been quite challenging. To solve the problem of possible leakage through water glass seal, the holder has been modified such that leakage through the interface between the two chips is not a problem for the vacuum of the TEM. A drawback of gluing the two chip-halves is that once glued, it is nearly impossible to separate them. For this reason, we developed a third method for the sandwiched chip NR, where the sealing is achieved through O-rings without glue. In this design, the two chips are clamped together (see Sect. 4.4), but can be separated after the in situ TEM experiments to allow additional experiments on the same sample, for instance using a highly surface sensitive technique which requires the absence of the top chip. We have also developed an NR that consists of one component only [48]. One-chip and sandwiched chip NRs are similar in size and can therefore be loaded in the same holder.

Concerning the required vacuum tightness, the NRs and holders and their interfacings have to be vacuum sealed. Due to the very limited space in TEM holders, this is not a trivial task. For standard high vacuum connections, one normally uses O-rings of a shore diameter of 2–3 mm. But because of the space limitations in particular along the electron beam direction such O-ring sizes cannot be used. All the NR-holder components (lid, NR top, O-ring, NR bottom, O-ring, holder) have to fit within 2–3 mm. As a result, the O-rings must have a shore of about 0.40 mm. The typical tolerance for an O-ring of 0.40 mm is 0.08 mm, which is more than the tolerance of about 0.02 mm in

compression of the O-ring needed for vacuum tightness. Thus, a careful selection and optimization of all components of the assembly is needed.

4.3 Different types of nanoreactors

Two major types of NRs (see Fig. 4.2) are used in Delft: the sandwiched chip NR and the one-chip NR consisting of a bottom chip with heater and top chip. Both types can be used in a static gas system, i.e., the gas must be loaded outside the TEM, and in a flowing gas system, i.e., the gas is led from a gas handling system outside the TEM through tubes in the TEM holder and through the NR and back. The sandwiched chip NR has two types of heaters: a spiral-shaped heater with electron transparent windows in between the Pt heater spiral, or a flat centre heater with a larger area for specimen mounting. A brief comparison between both the NR designs is given in Table 4.1. Information on the fabrication of both kinds of NRs is given further in the chapter (Table 4.1).

4.4 The nanoreactor holders used in Delft

The NR has to be supported by a holder, whereby the combination of NR and holder should allow: (1) full vacuum tightness, (2) a resolution better than 0.1 nm, (3) reliable electrical contacts for the MEMS heater in the NR, and (4) a gas inlet and outlet in the case of the flowing gas holder.

Note that the gas tubes and the wiring for the electrical contacts have to fit into the TEM holder. This limits possible upgrades like adding valves in the tubes or preheating of the gas in the tube. Differences in the size of the holders influence the design of the NR. As an example, FEI and JEOL holders are shown in Fig. 4.3. Obviously, the JEOL holder with its much larger diameter provides more space for add-ons in the holder. Nevertheless, up till now we have always been able to realize all features in the FEI holders (with an inner bore of the narrow part of the holder tube being less than 5.5 mm) in which the most complicated one was a double tilt vacuum transfer heating-holder.
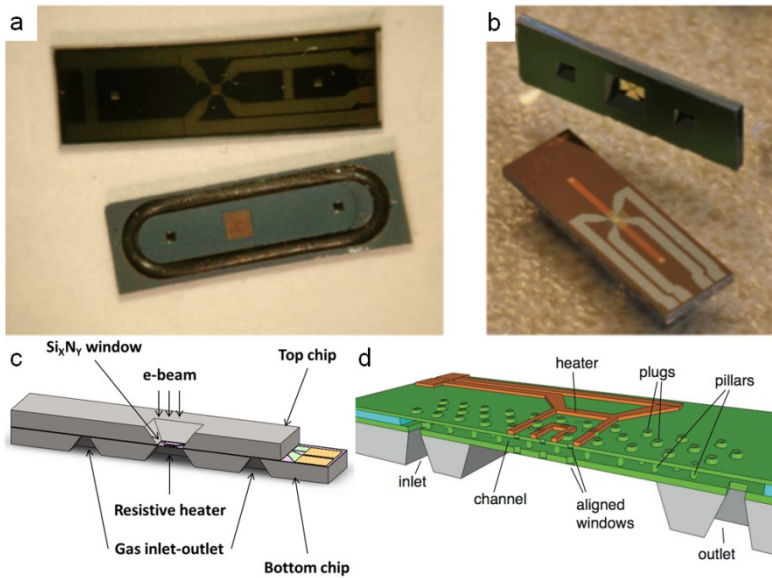
Figure 4.2. Optical images of the two chip halves of the sandwich NR (a) and one-chip NR seen from top and bottom (b). (c) 3-D sketch of the sandwich NR, consisting of a bottom chip with the heater and the contact pads for connection of the heater to the heater control. (d) 3-D sketch of the all-in-one NR. For clarity, the thin-films' thicknesses have been drawn thicker than they are in reality. The channel is 4.6 mm long and 0.3 mm wide.

Figure 4.3. A comparison of the shapes of a JEOL and an FEI flowing gas holder.

Table 4.1. Advantages (in upright) and disadvantages (in *italics*) of sandwiched chips and one-chip NRs.

Sandwiched chips NR	One chip NR
Sample of any size can be loaded	*Only particles can be loaded with a dispersion led through the gas channel*
Sample can be positioned at a desired location (only in the middle of the heater)	*The whole inside space of the NR will contain particles*
Sample is only presented on the heater membrane	Sample is presented on both membranes
Channel height can increase from 5 to 35 μm upon gas pressure	Channel height (e.g., 2 μm) dependent on pressure
Top chip can be removed for further analysis (tomography, surface analysis, etc.)	*Top membrane cannot be removed*
O-ring thickness between NR chips is critical	NR itself is leak-tight
Assembly process may cause contamination	It is easier to prevent contamination
The fragile parts of the two chips are well protected	*Top of the chip is very fragile*
Alignment of two chips could fracture a membrane	Alignment is not an issue in this case
A modification (e.g., add biasing line) is fairly easy	*Modification is complicated*
More than one sample can be loaded and studied at the same time	*The loading of the suspension could clog the channel*
An NR can be used several times, e.g., in case of metal lamella	*Reusing this system also requires thorough cleaning which is not feasible in all cases*
External dirt particles can be present during the assembly	Dust particles is limited to suspension only

Figure 4.4 shows our flowing gas holder for an FEI TEM, which has been used for the 1 bar corrosion experiment discussed in Malladi et al. [28]. The gas system (all components that are in contact with the gas that is lead through the NR) can be taken out of the holder for dedicated cleaning. We used two types of materials for this: Pt and Ti. In the example shown in Fig. 4.4, the material is Ti. The construction on the right side of the holder shown in Fig. 4.4 is to prevent strain on the Ti tube coming out of the holder, which could induce a leak due to the creep of the tubes.
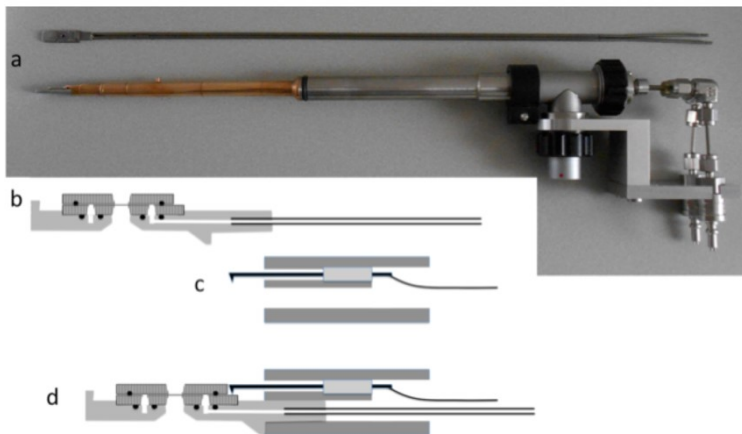
Figure 4.4. The flowing gas holder (a) shows a holder that has been realized and has been used for corrosion experiments. Above the holder the tip/tubing combination is shown that can be removed as one piece. (b–d) Cross-sectional sketches of the holder tip disassembled and assembled onto the holder. The inlet and outlet tubes run all the way to the other side of the holder (extending outside of the TEM), where they are attached to a gas supply system. The tip and gas tubes of the holder shown in (a) are completely composed of Ti (except for the O-rings in the tip). This tip-tubes system can be taken out from the holder and be cleaned, for instance by a bake-out in vacuum at 300 ^{0}C.

Figure 4.5 shows our static gas holder. The holder has a separable tip, which contains an airtight chamber that can store gas with a volume of 1–10 mm^3. Gas is loaded in or pumped out through a valve in the tip (see arrow in Fig. 4.5b). The NR is similar to that of the flowing gas holder, but could also be made more dedicated, for instance with a build-in pressure meter. In the experiments we did up till now, we used our standard NRs, which allow both static and gas-flow experiments.
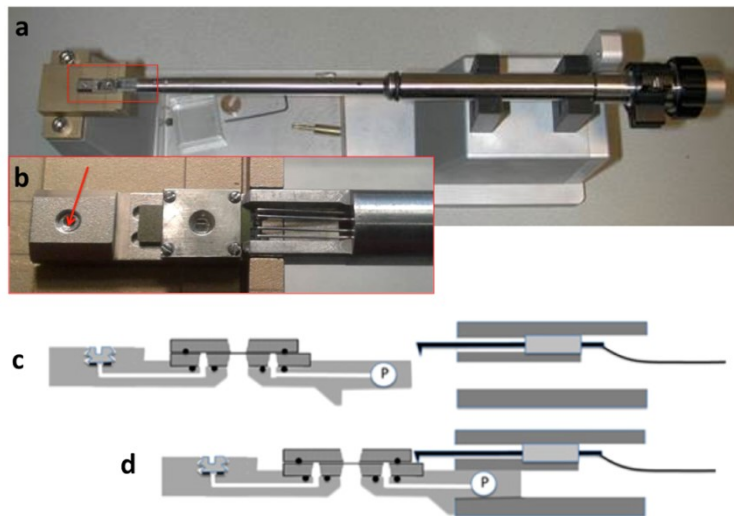
Figure 4.5. (a) Image of the static gas holder and (b) an enlarged view of the tip part with the square lid on top. The red arrow indicates the valve to open or close the tip, (c, d) show cross-sectional sketches of the holder tip disassembled and assembled onto the holder, respectively. P indicates a pressure meter. The lid to clamp the two chips together is not given in (c) and (d) but can be seen in (b).

Figure 4.6 shows a previously used holder, in which the NR is allowed to be leaky between the two chip halves. The advantage is that this connection between the two chips is not critical in the airtightness, for instance allowing glues that are not sealing very well but do not contain hydrocarbons. The disadvantage is that the lid (with a hole of 1.0 mm over the membrane area) to make the chamber in which the NR is located has been thick because the large O-ring has to be pressed down everywhere sufficiently by two screws of the far ends of the lid.

Some advantages and disadvantages of the static gas holder and the flowing gas holder are indicated in Table 4.2.
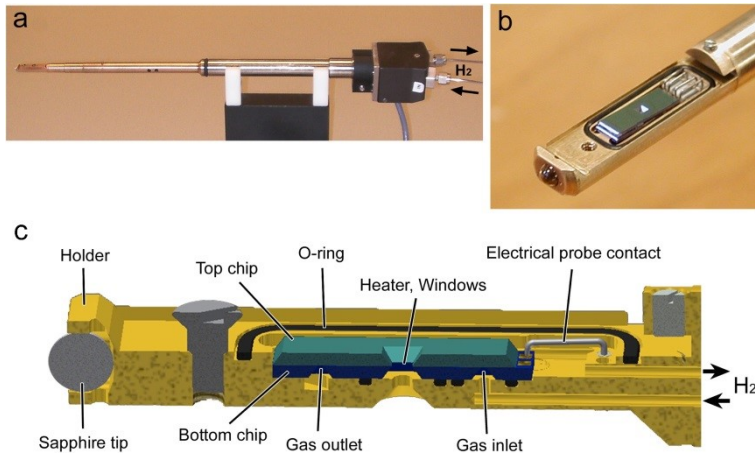
Figure 4.6. Sample holder used for the 4.5 bar hydrogen gas experiments. (a) Sample holder. (b) NR inserted in the sample holder. The lid of the holder is removed for a better view. Mounting of the lid is done by sliding it into an opening indicated by the blue arrow and next tightening the screws indicated by the red arrows. (c) Schematic diagram of the NR inserted in the sample holder.

Table 4.2. Comparison of using NR with static gas or flowing gas, advantages (in upright) and disadvantages (in *italics*).

Flowing gas system	Static gas system
Gas handling system near TEM is complicated	Simple setup at the TEM
Gas pressure regulation possible	*Pressure cannot be regulated, is dependent on T and may drip due to leakage*
Alternating different gases possible	*Because price of tip is small compared to whole holder, running several experiments in parallel (e.g., ageing) is well doable*
Allowed leakage can be much higher than in static gas situation	*Even a very small leak results in significant pressure drop*
	Tiny gas volume allows for special/expensive gases
High hazard gases not possible	Also, high hazard gases can be loaded outside the TEM area
	Transfer to another analysis tool is easy

4.5 Manufacturers of nanoreactor systems

There are three major companies that produce holders and chips for different types of in situ TEM experiments at pressures that cannot be realized in an ETEM: DENSsolutions [49], Hummingbird [50], and Protochips [51].

The Hummingbird gas holder provides single and multichannel gas delivery systems, which are used to study solid–gas interactions at or just above atmospheric pressure. When the holder is fitted with a heating chip, it also supports real-time observation of catalysis reactions in the TEM. The sample can be heated up to ~800 ^{0}C. The temperature is controlled with closed-loop temperature control software that works with the calibrated sensor on the chip. Protochips has gas and liquid flow holders, giving the opportunity to study the real-time material behaviour inside the TEM at pressure and temperature up to 1 bar and 1000 ^{0}C, respectively. Note that the presence of a gas allows heat exchange with its environment. When the temperature calibration was done in vacuum, this leads to wrong temperature indications (see further information below). Most of our own NR developments described in this chapter are or will be commercialized by DENSsolutions. Several examples of applications of the gas holders are: (1) The solid–gas interactions related to oxidation reaction of cobalt-based nanocatalysts uncovering in situ evolution of the Kirkendall effect [52]; (2) The oxidation of two-dimensional Ti_2C_3, also known as "Mxhene," whereby the production of carbon-supported TiO_2 was shown as a function of the heating rate, the temperature range, and the exposure time [53]; (3) The formation of mesoporous Pd powder with a pore diameters of 7 or 13 nm in vacuum and H_2 gas; (4) The (de)hydrogenation of Pd at pressures up to 4.5 bar [47].

The three companies also have liquid (flow) holders, which enable research to be carried out in a static or dynamic liquid environment, also see review by the de Jonge and Ross [54]. Examples of this kind of in situ TEM are (1) in situ quantification of the electrochemical nucleation and growth of copper clusters on gold from a 0.1 M $CuSO_4.5H_2O$ 1 vol.% H_2SO_4 solution [55]; (2) direct observation of calcium carbonate crystal nucleation which enables future research on the role of living organisms on this type of nucleation [56]; (3) the use of ETEM in closed liquid cells or in liquid flow devices. The authors claimed that atomic resolutions can be achieved in liquid enclosures with 50 nm thick SiN membranes [57]; (4) the electrochemical charging of a battery in a TEM liquid flow cell by imaging of electrochemically active ions in the electrode and electrolyte in electrical energy storage systems at nanoscale [58]; and (5) the structural evolution and electrochemical response of Pt–Fe nanocatalysts, which showed that the particles growth rate depends on both site and the potential [59].

4.6 Design requirements for the NRs

There are several general and specific requirements can be listed for operational and successful NRs. These requirements are given in the following sections of this chapter.

4.6.1 Electron transparent windows that withstand 10 bars

A MEMS NR consists of two parallel membranes of about 500 nm thick with a gas in between them. These two membranes contain several ultra-thin regions (e.g.,15 nm thick) that act as electron transparent windows. Most of the time we and other NR developers have used SiN as membrane material, but other materials such as SiC and SiO_2 are also possible. In this subsection, we write SiN membrane, but it should be read as a class of materials that are relatively inert, can withstand high temperatures, and are preferably amorphous.

When the goal is to obtain a gas pressure of 10 bar, the requirement for a reliable NR is that the big relatively thick membrane and the very thin electron transparent windows must survive exposure to this gas pressure. Modelling can be done on the mechanical response of different window geometries under uniform pressure to determine the limits of various designs. Furthermore, Alan et al. [23] did an experimental study to characterize the reliability of certain window thicknesses. The simulations and the experiments show that high-pressure operation can easily be obtained by simple design rules for the SiN membranes and windows.

Nonlinear finite element ABAQUS software was used to map the deflections and stress distributions for the membranes under the influence of 10 bar uniform pressure to estimate the failure probability of the devices. Two components have to be modelled: (1) The larger membrane that contains, e.g., the microheater and (2) the electron transparent windows. The stress distribution in the large membrane is shown in Fig. 4.7. It can be seen that the largest stress is present near the location, where the membrane is attached to the Si chip. Note that these stresses can be reduced by changing the size and shape of the windows which is discussed in Fig. 4.9. In addition to larger membrane calculations, several different window geometries (elongated and circular) were tested as illustrated in Fig. 4.8 and Table 4.3. The maximum stress values decrease with decreasing lateral dimensions. Circular structures have lower maximum stresses, due to their symmetry.
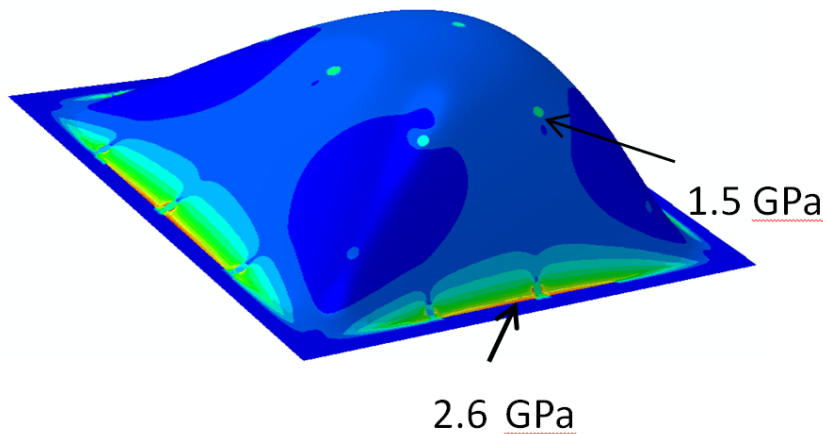
Figure 4.7. Stress distribution in the large membrane and the electron transparent circular SiN windows (small green areas, one indicated by an arrow).

Next, the simulations were repeated by taking the corner stress singularities into account. Figure 4.12 shows the models for two calculations: a 90^0 corner and a tapered shape. The calculations show that the tapered corner has reduced stresses (from 2.85 to 1.95 GPa), and hence increases reliability significantly.
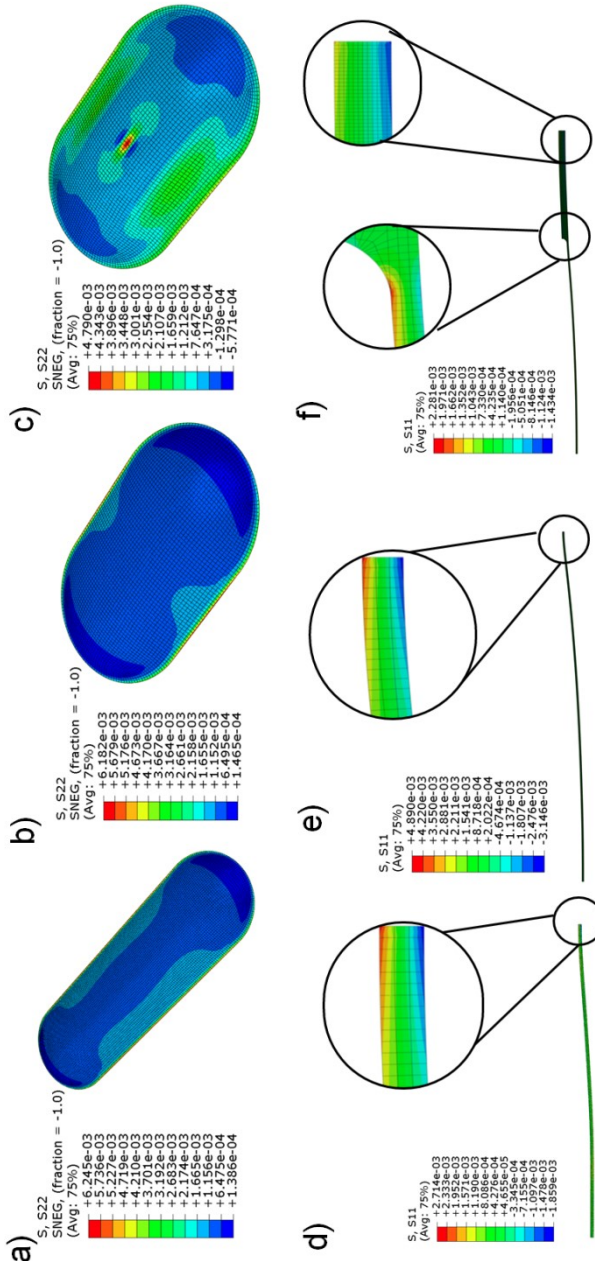
Figure 4.8. Deflected shapes of the windows and the resulting stress distributions under 1 bar uniform pressure. Top figure: elongated membranes with lateral dimensions (a) 6x20, (b) 6x10, and (c) 3x5 μm. Bottom figure: axis symmetric models of circular windows in cross-section having (d) 3 μm and (e, f) 6 μm radii. The small circles in (d–f) indicate the transition from the thin electron transparent window to the thick SiN support. In (f), this is two-step transition, firstly from the thin window to a thicker window as indicated in Fig. 6.12, and secondly from this window to the thick SiN support.

57
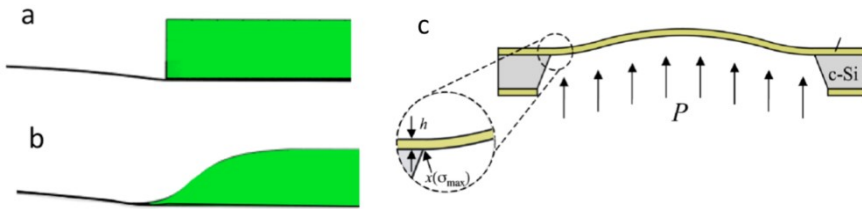
Figure 4.9. Shapes of the models used for the calculations with (a) singular corners, (b) tapered corners, and (c) schematic of nanoscale bulge tests.

Table 4.3. Summary of the simulated results compared to experimental failure probability. The simulation results indicate that circular membranes have a much higher chance of survival under 10 bar pressure. Reliability and stiffness may be further enhanced by varying the thickness at the edges of the membrane.

Applied Load	1 MPa uniform pressure					
Membrane type	15 nm thick elongated			15 nm thick circular		
Lateral membrane dimensions (µm)	3x5	6x10	6x20	3	6	6
Variation in membrane thickness (nm)	-	-	-	-	-	15-60
Maximum out of plane deflection (nm)	105	215	256	66	170	115
Maximum tensile stress (10^{-3} GPa)	4.79	6.18	6.25	2.71	4.89	2.28
Failure probability	8%	52%	56%	1%	10%	<1%

According to the simulations, the NR design with the elongated windows has an approximate 50% chance of survival under 10 bar pressure. The results also suggest that the survival probability would increase to 99% if the lateral window dimensions are reduced and if circular windows are taken with a varying cross-section as indicated in Table 4.3. Note that the probability of survival should be very high because failure of the membrane could result in a damaged electron source, of which a replacement costs 10,000 to 20,000 euro.

4.6.2 Allow heating of gas and specimen with a high accuracy in T

The MEMS heater has as big advantage that the power needed for the heating of the sample is small. In the design of the heater, this is achieved by realizing local heating inside or on top of the central part of a thin membrane. Because the heat conductance through the membrane to the supporting Si on the sides of the membrane is poor, one can easily obtain a temperature of 1000 ^{0}C in the centre of the membrane, whereas the temperature of the Si hardly increases. We typically measure temperatures less than 40 ^{0}C for the Si chip for a heater temperature of 1000 ^{0}C. Note that the heat transfer to the Si chip depends on the distance from the heater to the Si and the thickness of the SiN. To reduce the heat transfer, one can increase the membrane size or reduce the thickness of the membrane, which indeed is an efficient way of heat transfer reduction, but increasing the size of the membrane width leads to more bulging of the membrane upon heating and a very substantial decrease in the membrane thickness can lead to more easy drum-like vibration of the membrane, which leads to loss of resolution when the sample is tilted.

Figure 4.10 shows a schematic presentation of the components in the heater chip and the holder that are relevant for the discussion on the drift properties of the total system. Figure 4.10 depicts the various components as a series of thermal resistors. One can relatively easily determine the temperature of the heater by the resistance of the heater. This obviously requires a calibration, which for instance can be done on a local scale (e.g., 10 μm) using the Raman spectrum of Si [60] or carbon nanotubes [61]. Once the heat distribution in the heater is characterized by local Raman spectroscopy, a pyrometer can be used to determine the temperature over a bigger area like 200 μm. The actual temperature of the specimen can be different from that of the heater because there are several thermal resistors between the sample and the heater (see Fig. 4.10). When the heater is in vacuum, a significant difference between heater and specimen only occurs if the temperature is well above 600 ^{0}C. This is because radiation becomes important above this temperature. In this case, the sample temperature will be lower than the heater temperature to an extent that is determined by the radiation losses of the various components from heater to specimen and the heat resistances of these components. For instance, we noticed a difference in the evaporation speed of the Au particles on graphene suspended over an 8 μm hole in the SiN: the evaporation was significantly slower in the central part of the graphene sheet. At low temperatures, the radiation is relatively small and one can assume that the temperature of the sample is about equal to that of the heater even if the thermal resistance between the thin window and the sample is high because there is no energy loss.
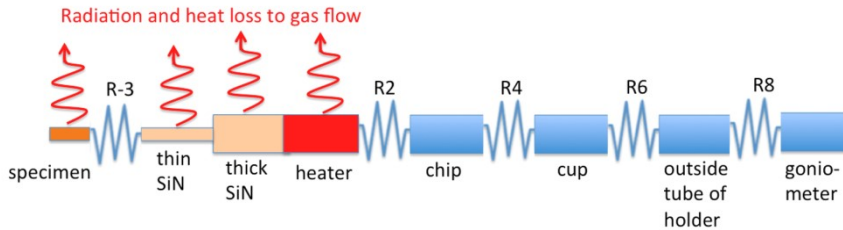
Figure 4.10. Schematic representation of the various thermal resistors (R1–R8, where R3, R2, R4, R6, and R8 represent the connections between the various parts) that determine the heat transfer of the heater to the goniometer of the TEM. Note that the outer tube is connected to several parts of the goniometer with components that have their own thermal resistance and contacts with the final heat sink. Also, the specimen itself, its contact with the support of the heater and the support-heater contact introduces thermal gradients and thus the real situation is more complicated than indicated here.

When a gas is used (either in an ETEM or an NR), the situation is very different because the gas acts as a heat exchanger between the heater/sample and the surrounding area. Since the power to obtain the set temperature is steered by measuring the resistance of the heater, the effect of heat dissipation by the surrounding gas is fully taken into account. In Tables 4.4 and 4.5, two measurements are given, one for nitrogen and one for helium. The heat transfer of helium is much larger than that of nitrogen; the latter is comparable to that of oxygen and argon. The heat exchange of hydrogen is comparable to that of helium. For example, compared to heating in vacuum, the power required to heat the Pt wire to 400 ^{0}C is about two times higher for 100 mbar nitrogen and four times higher for 100 mbar helium. A calibration based on a vacuum condition would lead to using an inaccurate required power to reach a certain temperature, i.e., the obtained temperature would be more than 100 ^{0}C lower in both cases. This signifies the importance of a real temperature determination, for instance based on a resistance. In fact, a four-point resistance measurement can be realized by adding another resistor than the heater, but this would require two extra electrical contacts. It would also require some extra microfabrication steps in the cleanroom because the heater and the T measurement wires will be on top of each other and need to be separated by an isolating layer such as SiN.

Table 4.4. Changes in power to microheater with applied pressure (as read from the gauge from nitrogen bottle).

P (bar)	T (°C)	R (Ω)	P (mW)	I (mA)
~10^{-3}	37	169	0.102	0.77
~10^{-3}	400	270	8.8	5.5
~0.1	400	270	20.1	8.60
~0.5	400	270	20.1	8.63
~1.0	400	270	20.2	8.65
~3.0	400	270	20.2	8.66

Table 4.5. Changes in power to microheater with applied pressure in a helium atmosphere as measured as the system was connected to a vacuum pump.

P (bar)	T (°C)	R (Ω)	P (mW)	I (mA)
Helium				
10^{-5}	30	281	0.181	0.80
10^{-5}	400	387	8.60	4.72
10^{-4}	400	387	8.60	4.71
1.4×10^{-2}	400	387	8.69	4.75
10^{-1}	400	387	9.51	5.0
5×10^{-1}	400	387	11.2	5.4
1.0	400	387	13.4	5.9
1.5	400	387	15.5	6.3
2.	400	387	16.8	6.6
5.0	400	387	22.6	7.4
10	400	387	27.1	8.1
20	400	387	32.4	8.9
40	400	387	35.3	9.6
50	400	387	36.6	9.8
100	400	387	38.5	10
250	400	387	39.9	10.1

Thus, in order to have a reliable temperature in a gas environment, the temperature has to be controlled by a device component that allows for a temperature determination. This could be done for instance by constantly measuring the resistance of the heater (we are using this method) or by a Raman optical system. Note that the latter requires a dedicated TEM within-column space for the Raman optical microscope. We have used Raman for an *ex-situ* calibration of the temperature distribution, for which we have built a dedicated measurement setup (Fig. 4.12).

Figure 4.12 shows simulations of the heat distributions in a vacuum environment of two types of heaters, a full spiral (left) and a flat centre heater (right). In both cases, the thickness of the SiN is 400 nm. A disadvantage of the full spiral heater is that the central area with a diameter of about 100 µm with an equal temperature is not completely flat due to the presence of the Pt lines of about 150 nm thick. Due to this it is, for instance, difficult to place exfoliated graphene over the holes. The centre part of the flat centre heater is completely flat. Note that the central flat heater has a slightly lower temperature, which is due to radiation loss. An almost constant temperature for the flat centre is seen for temperatures below 600 ^{0}C, where radiation losses are very small.
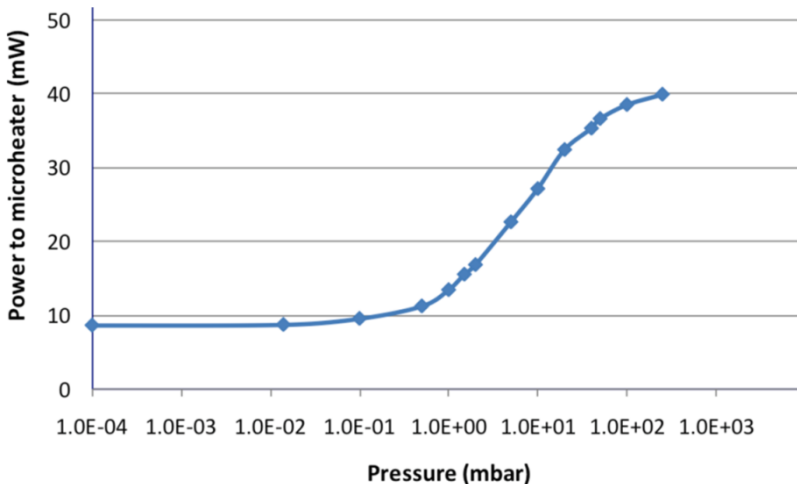

Figure 4.11. Power needed for the microheater to maintain a temperature of 400 ^{0}C at different helium pressures.
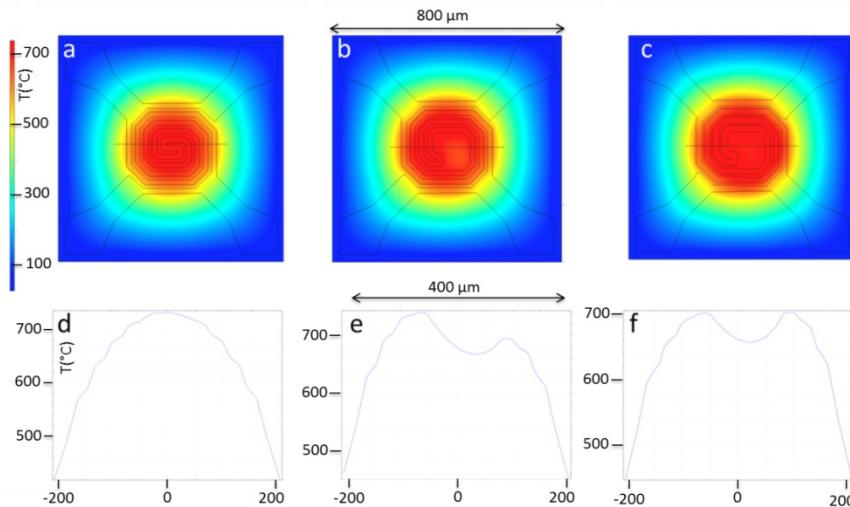
Figure 4.12. Simulated temperature distribution across the membrane incorporating a Pt heating coil of different shapes. In (a), the spiral is continuous up to the centre. In (b), a flat centre area in the middle is present. On one side of the central flat area, four-point lines are present and on the other side three-point lines. Due to this, the temperature profile is asymmetric. In (c), the same asymmetry in terms of number of lines of the heater is presented as in (b), but the width of the lines is adjusted such that a symmetric temperature distribution is obtained. The temperature profiles of the centre 400 µm of (a–c) are given in (d–f). With two types of heating coils, one with a continuous heating coil (a) and one with a flat centre in the middle (b). (c, d) Represent line-scans of the temperature distribution in the NR along the horizontal axis through the centre of the heating spiral. Similar results as to (a) are reported by Vendelbo et al. [62], who included the presence of CO gas.

4.6.3 Easy loading of the specimen

The samples to be studied with in situ TEM analysis are pieces of metals, ceramics, thin films on substrates, or even soft biological materials. Over the years, several successful specimen preparation techniques for various kinds of materials have been developed for conventional TEM analysis. For conventional TEM studies, the most common specimen preparation techniques include electro-polishing, ion-milling, grinding the specimen to extremely fine particles (<100 nm), and dispersing on standard TEM grids and specialized techniques like ultramicrotomy and focused ion beam (FIB). Almost all of these techniques can be adapted for in situ TEM studies using the NR provided the specimen is transferred successfully to one of the two chips (the bottom chip). We have carried out an experiment on the dehydrogenation of Pd deposited on the top as well as the bottom membrane

as a function of temperature and hydrogen pressure and observed that the temperature difference between top and bottom chip was less than 10 K. Nevertheless, it is best to put the sample on the chip half that contains the heater. Conventional TEM specimens are 3 mm circular discs that fit in standard specimen holders. However, owing to the limited size of the microheater and the electron transparent windows the sample size in an NR is more limited. Since one wants to keep the distance between the two membranes small, the sample should also be thin (e.g., less than 2 µm) over the whole lateral shape. In addition, really thin sample areas are required over some of the electron transparent windows (typically ~5 to 20 µm in diameter). Of course, the thin part of the specimen should precisely be placed on such a window.

Ceramic TEM specimens are prepared by just crushing a bulk material and putting them in suspension. Nanoparticle suspensions or suspensions of biological specimens are best transferred by sonicating the suspension for sufficient amount of time and drop casting a sample. Because the densities of these suspensions are usually high enough to cover most of the TEM windows, there is enough material to carry out in situ TEM studies. Bulk metallic specimens and thin films over substrates for which cross-section specimens are required, specimen preparation using FIB works best. An added advantage of using an FIB is that very specific areas of interest can be selected. Examples are cross-section samples across an interface, specimens from a special phase, and specimens corresponding to a specific crystallographic orientation (Fig. 4.13). Such specimens are typically of the size ~15 µm x 5 µm with thicknesses ≤100 nm.
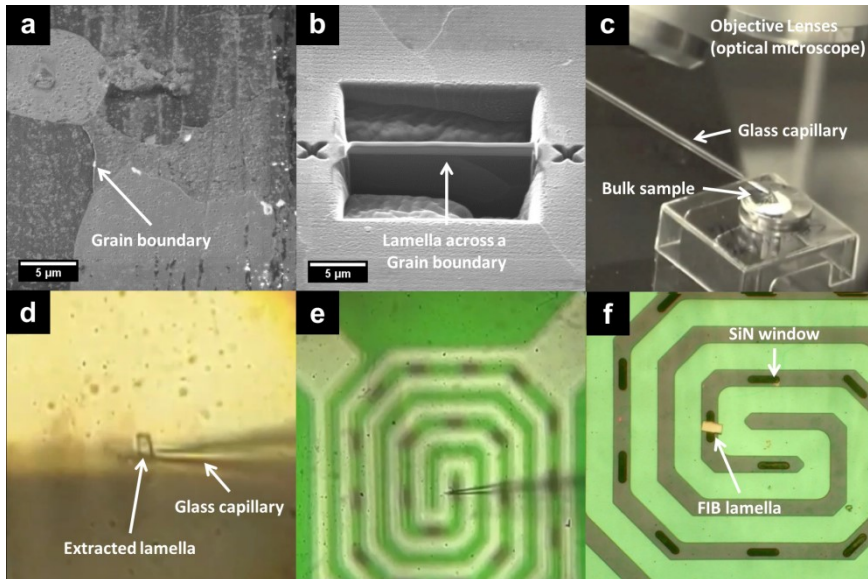
Figure 4.13. (a) FIB-SEM image showing grain boundaries in an aluminium specimen. (b) FIB cross sectional lamella prepared across grain boundary shown in (a); the lamella at this stage is cut and finally thinned to thickness <100 nm and released to stand freely in the cavity. (c) Photograph showing glass capillary controlled by a hydraulic micromanipulator. (d) Optical micrograph focused on extracted FIB lamella from a cavity as shown in (b). (e) Optical micrograph focused on glass capillary positioned precisely over a TEM window; the hydraulic micromanipulator allows positioning the lamella with an accuracy of ~2 μm. (f) FIB lamella deposited over a thin SiN window, ready for imaging either for in situ heating experiments, or for assembling an NR.

Specimens can be transferred to the TEM windows of an NR very precisely by using an *in situ* micromanipulator available on most modern FIBs or by using the conventional ex situ micromanipulator employing a glass capillary with a sharp tip. An example of FIB cross-sectional preparation across a grain boundary in an aluminium alloy and its *ex-situ* transfer using a glass micro capillary is shown in Fig. 4.13c–e. If there are specific areas of interest in conventional 3 mm disc specimens, these areas can be cut precisely using the FIB and transferred to the bottom chip. Upon successful transfer, the specimen is ready for either in situ heat treatment studies using a heating-holder compatible with this bottom chip or, for in situ environmental TEM studies when the bottom chip is coupled to a top chip to make an NR as shown in Fig. 4.14.

The bottom and the top chips are first positioned facing each other in a custom-made alignment tool as shown in Fig. 4.14d. The procedure of alignment starts with coarsely positioning the top chip (facing downwards) such that the large SiN windows in both the top and bottom chip coincide with each other. The alignment tool consists of micrometre screws connected to metal plates which displace the top chip with ~1 μm step size. The alignment tool has the capability to precisely displace the top chip only in the XY-plane. In order to avoid any displacements in the Z-direction, the top chip is restricted to just horizontal movement by fixing the lid. Once the window(s) of the top and the bottom chip coincide, the top chip is moved down in the Z-direction by gently screwing down the lid. While fastening the top chip, one has to be very careful not to damage the top chip by any excessive torque. An indication of the right channel height for in situ TEM experiments is that both the top and the bottom chip are visible in the same focal plane in the optical microscope.

The alignment tool described here requires the NR to be glued either by an epoxy-based glue, super glue, or water glass. This principle of aligning the top and the bottom chips together has been extended further to avoid gluing altogether by including an O-ring in between the chips by creating a groove in the top chip. For this, the alignment tool has been adapted to allow either a retractable tip or a TEM holder with gas-flow channel. In these cases, the top chip is held in position after alignment by the lid. The O-ring in between the chips helps to maintain the NR leak-tight to allow live imaging inside the TEM.
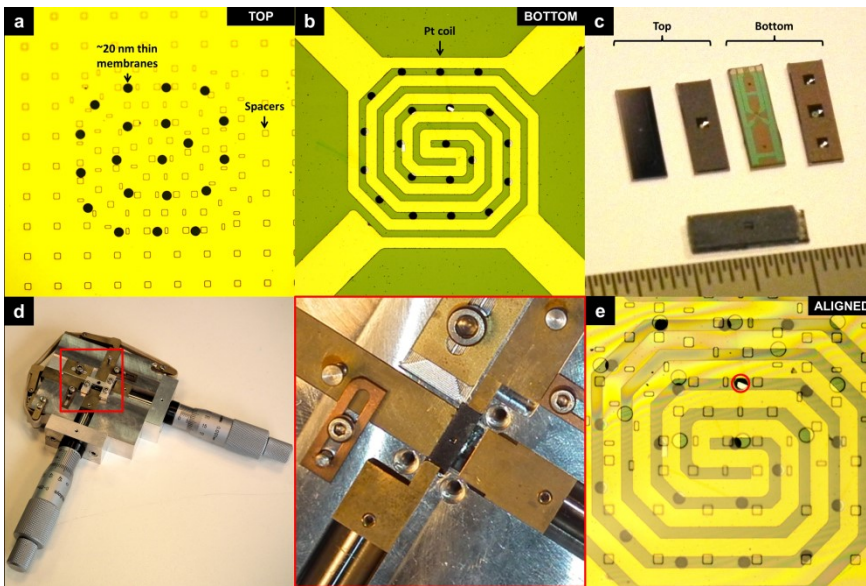
Figure 4.14. Optical micrographs showing the large SiN windows of (a) the top chip and (b) bottom chip. These windows are at the centre of the chips shown in (c). The bottom chip is placed facing upwards in the alignment tool shown in figure (d) while the top chip is placed facing downwards. Zoomed image of the area bounded by red box at the centre of the alignment tool shows the metal plates connected to micrometer screws which displace the top chip with displacements as small as ~1 µm. The lid is placed over the chip assembly and tightened enough to allow displacement only in the XY-plane. After the window(s) in the top and the bottom chip are aligned as shown in (e), the NR is ready for gluing to be used either in a static gas system or a flow-gas system.

4.6.4 Allow a controllable gas

Ultimately, one would like to control the gas pressure and the composition to the extent that both can be changed instantaneously. This is, however, not possible due to the geometry of the NR and the geometry of the holder. The NR has very narrow channels creating barriers for a fast gas flow, needed for a rapid gas exchange. Thus, the small size of the NR, giving on the one hand the advantage of fast temperature changes without experiment-limiting specimen drift, has on the other hand the disadvantage of slow gas exchange. Also, the NR is only hot in the centre of the two membranes, and the rest of the NR is at about room temperature. Thus, some of the reaction products could be deposited on the cold part of the NR. Furthermore, the diameter of the TEM holder does not allow for electrically controlled valves close to the NR. Therefore, the gas tubes of the holder have to be pumped to exchange the gas.

If one needs only a fixed gas pressure, one could use a static gas holder for which the exchangeable tip can be extended with a pressure meter for instance. This requires extra electrical wires at the outside of the holder, making the holder more complicated. If one needs a gas flow or a change of the gas composition, a flowing gas holder is required. As mentioned in Table 4.2, the static gas and flowing gas holders have their own advantages and disadvantages.

4.6.5 Compatibility with normal TEM operation

One of the big advantages of an NR over an ETEM is that the experiments can be done in any TEM, provided that the holder is completely compatible with the normal operation of a standard TEM sample holder. This is fairly easy to realize. Note that with this approach also low-end TEMs can be used, which are actually sufficient for quite some experiments. With the possibility to use also low-end TEMs, in situ TEM is also attainable for relatively less equipped research groups. Note in this respect that for an LaB$_6$ type of electron source the restrictions on airtightness of the NR and the holder are less stringent. This is because in the case of a collapse of the NR, damage to the gun is less severe and replacing the gun is much less costly and time consuming than for an FEG. We have never had a problem with a collapse of the NRs, even in high-risk experiments in which we explored the maximum pressure or temperature allowed, for which we typically used our LaB$_6$-operated TEM. The gas holder can be made completely compatible with a standard goniometer, such that the *in-situ* experiments are not hampering the normal use of the microscope in any way.

4.6.6 The NR should be easy to use and made as disposable

The challenges involved in in situ TEM experiments at relatively high gas pressures require sophisticated MEMS fabrication to obtain reliable miniaturization. The sample clamping and preparation need to occur at a very high control, which typically requires about 40–100 cleanroom process steps. Evidently, these challenges become more difficult when one wants to combine several external stimuli such as an electrical measurement in a gas environment. If more stimuli are added, a further miniaturization has to be realized, given the limited available space in the electron microscopes.

4.6.6.1 The cleanroom process for the sandwiched NR

The design of the sandwiched NR consists of two different chips which are a MEMS-based heater chip (bottom) and O-ring chip with grooves (top). The MEMS-based heaters that are presently used in the NRs are the same as those for in situ heating TEM studies. These heaters have been shown to be

very efficient in TEM studies, such as morphological transformation of gold nanoparticles [3], sculpting of graphene [24], thermal stability and degradation of nanoparticles [25]. The heaters have platinum (Pt) as the heat-conducting material, which is embedded in a ~400 nm thick SiN membrane with 6 µm wide viewing windows of ~20 nm thick SiN. Since the embedding requires two SiN deposition steps, Pt has to be stable in the gases used in the second SiN deposition. In the case of an NR, embedding of the Pt by SiN is essential to prevent that Pt is reacting with the experimental gas. Our MEMS heater contains four electrical connections that allow for temperature determination and heating. The other chip (also called top chip) has a groove depth of ~300 µm for the O-ring. The top chip consists of a ~500 nm thick SiN membrane with 12 µm wide viewing windows of ~20 nm thick SiN. MEMS-based heaters and top chips can withstand at least 1 bar pressure.

In Fig. 4.15, the fabrication steps are shown for bottom and top chips. The steps include low-pressure chemical vapor deposition (LPCVD) of SiN, plasma enhanced chemical vapor deposition (PECVD) of SiO_2, lithographic definition, dry and wet etching, dicing, and cleaning. Both Si wafers have an initial thickness of 500 µm. The initial step to fabricate a heater is LPCVD of 200 nm thick SiN that acts as an isolation layer between Pt and Si. The platinum layer is embedded in ~400 nm thick SiN layer in total. Subsequently, by optical lithography the viewing windows with a diameter of 6 µm are patterned onto SiN layer by anisotropic plasma etching based on AR and CHF_3. The last LPCVD step is performed to obtain 20 nm thick SiN electron transparent viewing windows. The silicon substrate is etched by KOH to get SiN membrane devices. The final steps are dicing the wafer and cleaning which leads to carbon-free, non-contaminated high-quality chips.

1. Heaters   **2. Tops (with spacers)**   **3. Full chip size**

(a)   (i)

(b)   (ii)

(c)   (iii)

(d)   (iv)

(e)

(f)
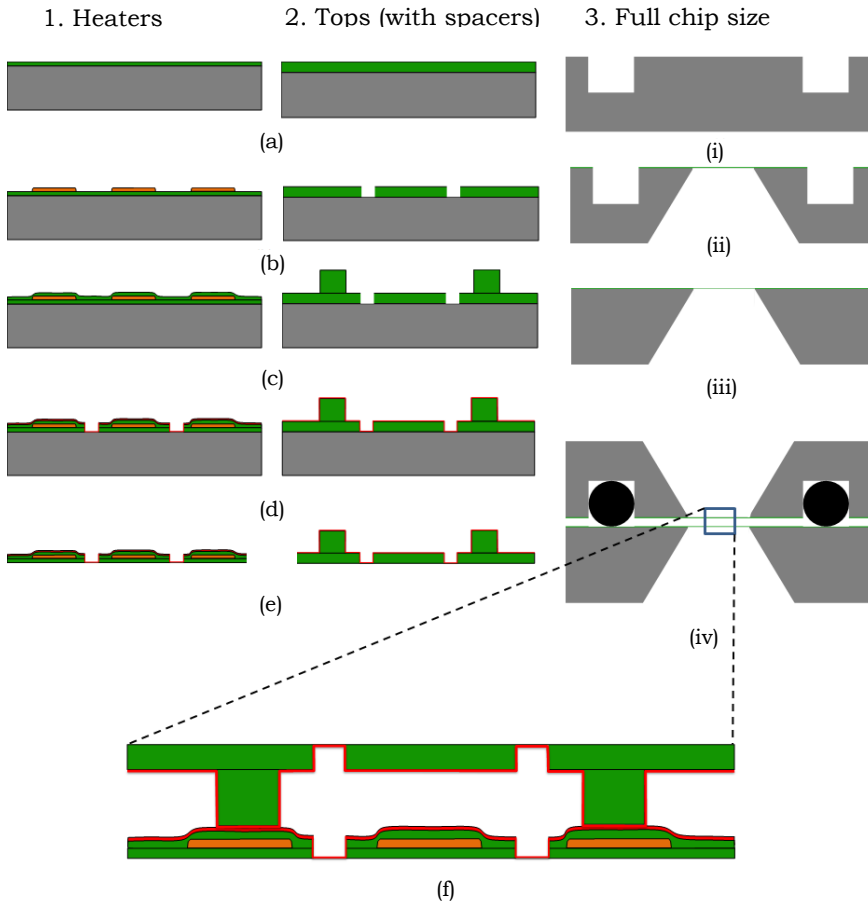
Figure 4.15. Schematic cross-section of fabrication steps for heaters (1) and top chips (2) are demonstrated. (3) Shows the full-size chip for heaters and tops for better understanding of sizes. (1a) and (2a) are deposition steps of SiN. (1b) is obtaining the Pt/Ta after deposition and etching, while (2b) is opening the electron transparent windows with optical lithography and dry etch of SiN. (1c, 2c) are LPCVD of SiN as a cladding layer for heater and spacer for O-ring tops, (1d, 2d) after lithography of viewing windows and deposition of ~20 nm thick LPCVD SiN. (1e, 2e) Are the final step of fabrication which are after back side lithography and wet etching of silicon by KOH. (3i) is after opening the O-ring grooves and (3ii) is after KOH etching of Si. (3iii) Shows the heater chip after KOH, and (3iv) is the full size of chips when they are mounted together including the O-ring rubber with the enlarged view in (f).

Similar to heater chips, the production of the top chips is started from a 500 μm bare silicon wafer. PECVD of SiO_2 is used as a mask layer, and the

~300 μm depth grooves are patterned and transferred to silicon layer by SF_6-based dry etching. The mask layer SiO_2 is removed by selectively wet chemical etching with buffered HF. LPCVD SiN is performed to get membrane ~500 nm. The viewing windows with a diameter of 12 μm are patterned and transferred to SiN layer. The size of these windows is bigger than the size of the windows in the heater to increase the alignment tolerance. The thin SiN deposition is performed, and silicon is etched by KOH from the back side to create a free-standing SiN membrane. The size of the top chips is slightly smaller than the heaters to have space for electrical contact pads, see Fig. 4.2.

4.6.6.2 The clean room process of the one-chip NR

The cleanroom process of fabricating the one chip NR is sketched in Fig. 4.16 [48]. The process roughly consists of the following steps: (1) Growth of wet thermal SiO_2 on a 100 mm Si wafer (0.2 μm); (2) Deposition of low-stress SiN_x (0.7 μm); (3) Photolithography and wet etching holes for electron transparent windows; (4) LPCVD of Tetraethyl orthosilicate (TEOS) as a sacrificial layer (1.0 μm); (5) Patterning of TEOS for pillars by using buffered HF (BHF); (6) Deposition of top SiN_x (0.5 μm) and plasma etching to create access holes to remove the TEOS in BHF; (7) Inside coating with TEOS and 15 nm SiN; (8) Plugging the access holes with SiN; (9) Creation of the Pt heater; (10) Local KOH etching of the mono Si to expose the electron transparent windows.

The important concept is the introduction of a sacrificial TEOS layer that can be removed later in the process, followed by (a) the internal deposition of again an LPCVD TEOS layer as an etch stop for later steps, and (b) the LPCVD SiN_x electron transparent 15 nm layer (exposed later by a KOH etch of the monocrystalline Si substrate). The access holes to remove the sacrificial layer are "plugged" by a PECVD SiN local layer sealed with another PVCVD SiN layer. The resistive heater is made by evaporation of Pt (0.2 μm) on top of an adhesion layer of Ta (15 nm) with the aid of a lift-off process. The final steps are the release of the electron transparent windows using buffered HF etching. The inlets and outlets of the channel are created by plasma etching using a shadow mask.
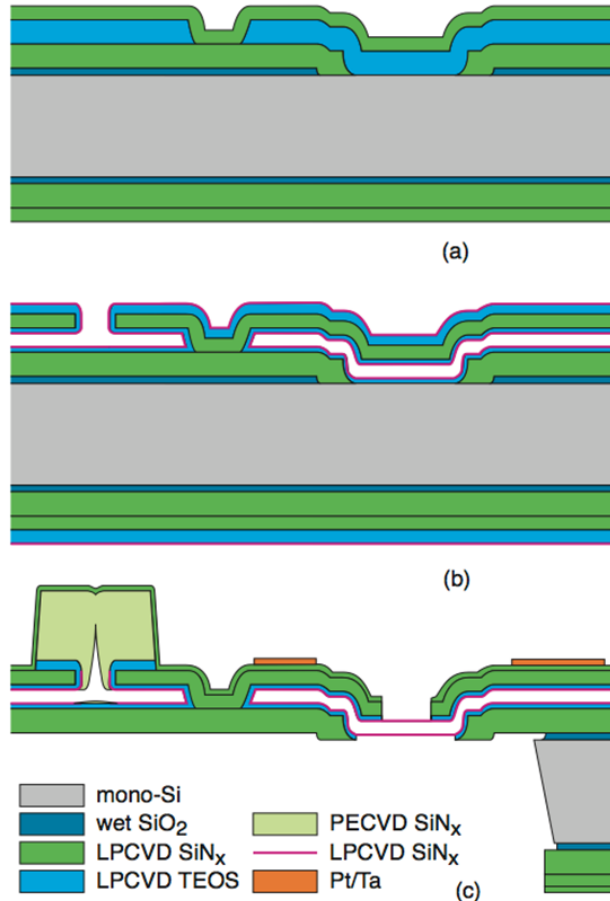
Figure 4.16. Schematic cross-section of the NR, in different stages of the fabrication [48]. (a) Initial wet thermal oxidation and low-stress SiN_x deposition, followed by photolithography and wet etching holes for electron transparent windows, and deposition of LPCVD TEOS sacrificial layer. (b) Sacrificial etching and internal coating of the channel with the window material. (c) Final thin-film structure: plugged channel, released windows. Fabrication steps: Growth of wet thermal SiO_2 on a 100 mm Si wafer (0.2 μm). Deposition of low-stress SiN_x (0.7 μm). Photolithography and wet etching holes for lower electron transparent windows. Deposition of LPCVD TEOS as sacrificial layer (1.0 mm). Patterning TEOS for pillars using buffered HF (BHF). Deposition of top SiN_x (0.5 μm) and plasma etching to create access holes to remove the TEOS in BHF. Inside coating with TEOS and 15 nm SiN_x. Plugging the access holes with SiN_x. Creation of Pt heater. Local KOH etching of the mono Si to expose the electron transparent windows.

4.6.7 The carbon contamination should be negligibly small

Since the characterization of a material under a gas atmosphere requires that the surface is very clean, the formation of C-contamination has to be prevented during the in situ TEM experiments. If available, a reliable method to remove any carbon is required. Keeping the sample free from C-contamination usually requires the absence of hydrocarbons, whereby the presence of water accelerates the formation of C-contamination. Note that the electron beam is an extremely efficient hydrocarbon "detector" because the electron beam can crack the hydrocarbon very efficiently to C. The presence of water plays an important role because it strongly effects the surface diffusion of hydrocarbons and probably plays a role in the cracking process as well. For instance, heating a sample in vacuum at 300 ^{0}C for a few minutes allows for subsequent C-deposition-free experiments at room temperature (see Fig. 4.17). Alternatively, cooling of the NR to, e.g., -60 ^{0}C while heating of the membrane to, e.g., 400 ^{0}C will allow trapping of water and hydrocarbon molecules outside the reaction area, thereby strongly reducing the formation of C-contamination as we have verified experimentally.

In Fig. 4.17, the deposition of C can be observed well, if one defocuses. In this case, a thick contamination was deposited by a beam roughly of the size of the contamination. Note that if a larger beam size is used, most of the contamination is deposited as a ring at the edges of the beam. If the C-deposition is much smaller than that shown in Fig. 4.17a, it can be difficult to verify the absence of any C-deposition. When a hole is available, C-deposition can be observed by growth of the edge as explained in Fig. 4.17b. When a hole like the one in Fig. 4.17b is not available and the C-deposition is small, we use a small spot size of, e.g., 5 nm and keep the beam for about 10 min at the same position (so no drift should be present) with the sample at about zero focus (to be sure that the actual beam on the sample is indeed small). Note that the beam should not be so intense that a hole is drilled in the electron transparent window as in Fig. 4.17b. Next at high under focus or over focus we check whether there is a local intensity change. If there is a hole as in Fig. 4.17b, we put the beam on the edge of the hole (as the yellow dot in the inset of Fig. 4.17b and keep it there, e.g., 10 min. In the case of C contamination, the edge will "grow" along the edge of the beam. If the growth is relatively fast, one can see it if the recording is done in movie mode.
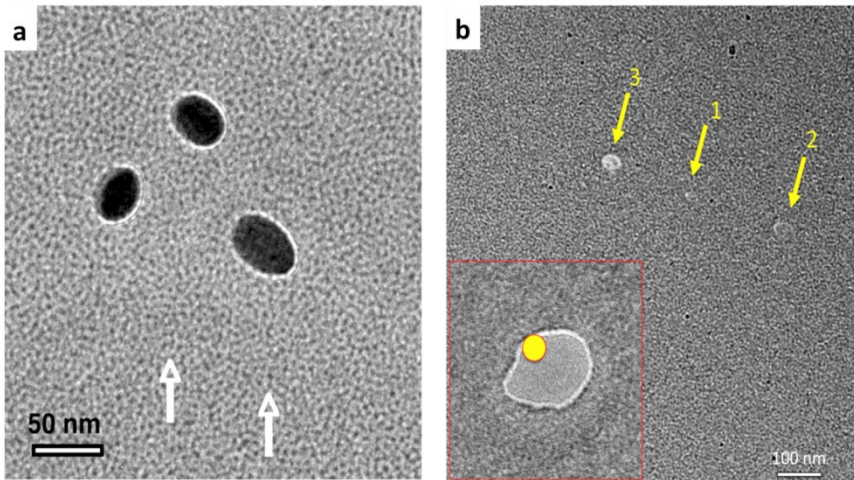
Figure 4.17. (a) Three C-contamination dots deliberately created on a C film using a dirty C film on a MEMS heater, by focusing the electron beam on these three areas for 2 min. Next, the sample was heated at 200 °C for 2 min. Subsequent focusing of the electron beam at the areas indicated by the white arrows for several minutes did not lead to any visual contamination. Note that a strong defocus was used to image the C-contamination dots. (b) shows that a very intense fully focused electron beam can remove SiN finally resulting in a hole in the SiN membrane. The beam was positioned at the locations indicated by the arrows 1, 2, and 3 for 1, 2, and 5 min. At arrow 3 a hole is present. This hole can be used for a precise determination of the absence of C-contamination, by putting a beam with a relatively low intensity such that no SiN is removed at the edge of the hole as the yellow spot in the inset in (b). In case of any C-contamination, one can see the growth of material at the edge real time.

4.6.8 The electron transparent membranes should be uniform in thickness and amorphous

Preferably, one would like to have no effect of the presence of the two membranes, but this is not possible of course. Typically, one wants to image the sample relatively close to zero focus. In this condition, one of the two membranes will also be close to zero focus, but the other one will not be and the modification of the electron wave by this membrane can be significant. This can be seen in Fig. 4.18, where two samples are shown at zero focus and 10 μm focus. Clearly, the effect of the membrane is much less at zero focus.
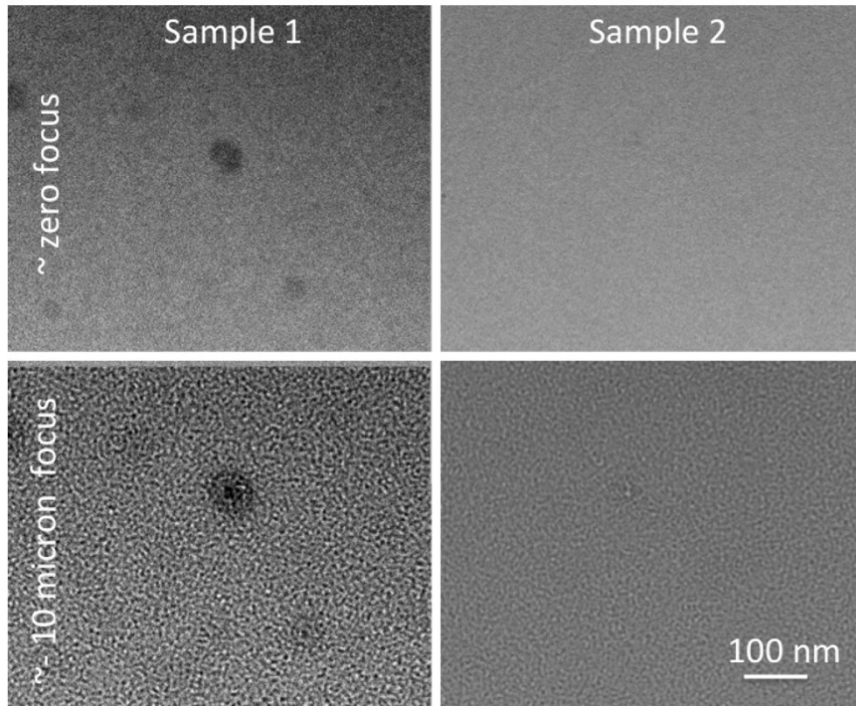
Figure 4.18. Example of two electron transparent ~20 nm thick SiN windows at zero focus and a focus of about −10 μm. In the left example, SiN-like particles are present of different sizes. In the right, hardly any particle can be observed. Note that such particles are much better visible if the imaging is done at high under or over focus.

Furthermore, it is clear from Fig. 4.18 that thickness variations (in the form of local bumps) can have a strong effect on the image. Therefore, the interpretation of a sample between one or two windows with thickness variations will be less easy. Therefore, we have put quite some effort in making uniform windows, which are as thin as possible. During the deposition of the thick SiN for the electron transparent windows, we add an Si test wafer, which can be tested for roughness using STM. Typically, we get a roughness of 0.4 nm RMS. Note that even when one has perfectly uniformly thick electron transparent windows, the relative positions of areas of interest can affect the measurement. For example, when both membranes are covered with particles of the sample to be studied, particles on one membrane will strongly hamper the study of particles on the other membrane if their projections partly coincide in one or more of the required viewing directions.

4.6.9 The length of the gas (or Liquid) column should be small

We have done experiments with thin SiN electron transparent windows to determine the minimum required thickness to maintain a 1 bar pressure difference over the window without breakdown. We have noticed a significant failure rate (>10 % of 10 chips with each 16 electron transparent windows) when the windows were 10 nm or thinner. Note that such a test will depend strongly on the quality of the deposited SiN. A thickness of 20 nm might be required for other SiN depositions to obtain no failure.

Assuming the thickness of the SiN windows is 15 nm, the total thickness of SiN is thus 30 nm. Taking as rule of thumb that the density of a gas at 1 bar is 1000 times smaller than the solid (of the same composition), a gas column of 20 μm of O_2 gas at 1 bar will be equal to 20 nm of solid O_2. The latter has a lower scattering potential than the two 10 nm thick SiN windows. Under these conditions, a good resolution can still be achieved. This back-on-the-envelope estimation also shows that a large reduction of the gas column is not very useful, if the thickness of the SiN windows is not significantly reduced.

One could use thinner SiN membranes if the failure rate is reduced or by using a lower pressure in the NR. Note however, that normally the holder is first in air and thus the pressure on the outside of the NR is 1 bar and once inside the holder this pressure drops quickly to 0 bar. Starting for instance with a pressure of 0.1 bar inside the NR, one has a pressure difference of 0.9 bar. Only if the pressure inside the NR is kept the same as outside the NR by a shunt between the inside of the NR and the vacuum of the microscope, one can use electron transparent windows that do not withstand a 1 bar pressure difference.

4.6.10 The resolution should preferably be the same as that of a standard holder

If an HRTEM that allows 1 Å resolution is used for the NR experiments and this resolution is lost because of the NR-holder-HREM ensemble, the reason for the resolution loss can be: the thickness of the SiN membranes, the thickness of the gas column, specimen drift, mechanical instability of the holder/NR ensemble, charging and other electrical instabilities, and/or the holder–goniometer interface. The specimen drift is discussed in more detail below. Our experimental results in getting 1 Å resolution show that all causes for resolution loss can be overcome. In many cases, one is interested in experiments for which a relatively large field of view is needed. For instance, if the front of the oxidation of Pd to PdO moves fast and over a big area, one gets

much more information from an overview movie with a relatively low resolution than a low field of view HREM movie.

Given the contradictory requirements of a high field of view and sometimes very detailed imaging, the best option is a combination of two detectors, whereby the first detector has a hole behind which at some depth a second camera is placed. If both cameras have 4k x 4k pixels and the first one has an effective pixel size of 0.1 nm/pixel and the second one a pixel size of 0.02 nm, the problem is how to display this in an efficient manner given the nature of the human eye. The display should be such that: both images are displayed on the same monitor or an array of monitors; whereby the image of the second detector is shown in the centre, and the first detector is displayed around this central area with the same magnification as the second detector and thus with 5x5 pixels in the display for each pixel of this camera. In this display mode, one can use the human eye, which is fine-tuned for focusing on the centre with high resolution and still be able to detect movements and rapid changes in the periphery.

4.6.11 The drift should be small enough to record high-resolution images

We typically set our goal for the drift to be less than 3 nm/min. This allows 1 Å resolution imaging with an exposure time of 0.5 s, which we consider as a standard recording time. In the case of imaging of changes, one prefers to obtain as many images as possible, and in such case exposure times of 0.5 s are rather long. Therefore, the possibility to record high-resolution images is not limited by the holder or NR.

4.7 Conclusions

An open system employing differential pumping and a closed system using MEMS technology with electron transparent windows in a device holding the specimen and the gas came up during the last decade, enabling a gas pressure of several bars. Here, we presented this closed cell approach based on a functional MEMS device known as "nanoreactor" to investigate gas–material interactions inside a TEM. We discussed the design and the development of different kinds of nanoreactors, along with the necessary accessories to carry out drift-stabilized, atomic-resolution environmental TEM studies.

CHAPTER 5

Thermal tuning of a silicon photonic crystal cavity infilled with an elastomer

"This chapter is based on the following article: 'Tuning of a cavity in a silicon photonic crystal by thermal expansion of an elastomeric infill,' authored by A.K. Erdamar, M. M. van Leest, S. J. Picken, and J. Caro, published in Applied Physics Letters, Volume 99, Issue 11, in 2011. Some sections have been adapted and expanded for the purpose of this thesis."

5.1 Introduction

Photonic crystals (PhCs) are artificial dielectric materials with a periodic modulation of the dielectric constant. The most striking property of a PhC is the photonic band gap, *i.e.,* a wavelength range where the PhC is opaque. The bandgap and the possibility to engineer its position in wavelength enable the control of the propagation of light [4]. Using these properties, novel devices have been proposed and demonstrated. In a PhC light can be confined in cavities, of which the transmission can be changed via a tuneable refractive index. These properties of a cavity are highly attractive for applications such as optical switches [15], add-drop filters [18] and low-threshold lasers [17]. These examples indicate that active tuning of PhC devices is indispensable for applicable functionalities. The refractive index can be tuned with optical [63], mechanical [22] and electrical methods [21]. Another method is filling the air hole(s) of a cavity in a PhC with a liquid crystal. The cavity transmission can then be tuned by driving the liquid crystal through the phase transition [64].

5.1.1 Cavity tuning with elastomer

In this work, we apply an elastomer as infill material to tune the transmission of a PhC cavity. Elastomers have weak bonding forces between the polymer chains, which leads to a strong thermal expansion and consequently a high negative thermo-optic coefficient (TOC) dn/dT. For infilling and transmission tuning we use Kraton SEBS G 1657 [65] (further just called "elastomer"), which is a highly stable and durable elastomer for infilling. The index of the elastomer is temperature dependent $n_{elast}(T) = 1.478 - 3.32 \times 10^{-4}(T - T_0)$ in the range of 293-323 K ($T_0 = 293\,K$), as deduced from refractometry measurements at 1550 nm.

For the tuning to be virtually lossless, the absorption of the elastomer should be weak in the wavelength range of the measurements (around 1550 nm). That this is indeed the case can be seen in Figure 5.1, which shows the absorbance as a function of wavelength. The data in this figure results from measurements of the light intensity transmitted through a 150 μm thick elastomer layer deposited on a quartz substrate. The absorbance thus includes absorption and scattering by the elastomer and reflection from interfaces, so that a deduced attenuation coefficient from these data gives an upper bound of the absorption coefficient. As can be seen, the absorbance is rather low and flat between 1200 and 1650 nm, while above this range it shows peaks at 1720 and 2300 nm due to vibrational modes, the latter one being very pronounced. At 1550 nm the absorbance amounts to 0.0026, which corresponds to a maximum possible absorption coefficient of 0.405 cm-1. Thus, on the scale of the elastomer thicknesses relevant in this work

absorption is negligible. The peak at 2300 nm may be strong enough to induce heating effects by absorption, which is promising for tuning applications in the mid-infrared.

With the experiments, global infilling of a hole-type silicon PhC slab with the elastomer and global thermal tuning of its refractive index is demonstrated. In particular, we study the tuning properties of the transmission of a cavity in the elastomer infilled PhC as a function of temperature. Our approach goes beyond the operation regime of thermal waveguides [66], which are clad by a polymer with a negative TOC of the silicon waveguide to make the properties temperature insensitive.
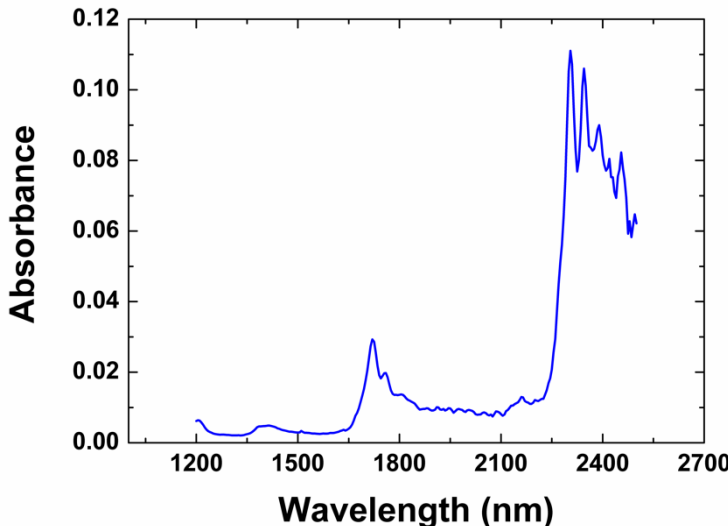

Figure 5.1. Absorbance of the bulk elastomer. Absorbance includes absorption, reflection and scattering. The thickness of the bulk elastomer is ≈ 150μm.

The final tuning goal on the basis of the elastomer is local infilling and local optical heating of the elastomeric infill of a cavity, resulting in an index change and a shift of the resonance wavelength. The absorption of the elastomer being low around 1550 nm, local heating should then be accomplished by doping the elastomer with dye molecules or quantum dots, provided that these materials after light absorption mainly decay non-radiatively, to ensure efficient conversion of locally deposited optical energy into heat. With the global infilling and global tuning experiments presented here we qualify the elastomer for tuning by local heating.

5.2 Design and device fabrication

Figure 5.2(a) shows a scanning electron microscope (SEM) image of the design of the cavity including the superimposed mode profile. The cavity, centred between the waveguides, is the modified point-defect cavity of Loncar *et. al.* [67]. The PhCs have a triangular lattice with nine rows of holes between the waveguides and are oriented for light propagation in the ΓM direction. The designed ratio r/a of the hole radius to the lattice constant is 0.3. The centre modified hole has r/a ratio of 0.2. The four holes closest to central defect hole are reshaped into half ellipses with the ellipticity 0.2. The cavity is very sensitive to an index change of the infill, since an appreciable part of the mode energy is localized in the holes. The lattice constant is litho-tuned in the range 490-510 nm across the PhCs on a chip.

The PhCs are fabricated in silicon-on-insulator (SOI) material, using electron-beam lithography and dry etching. The device layer of the SOI is 220 nm thick, while the buried oxide is 2μm thick. The lithographic pattern with PhCs and 2.5 μm wide waveguides for in-and-out coupling of near-infrared light is written in a 120 nm thick ZEP 520 resist with a Leica 5000+ e-beam system. After resist development the pattern is transferred to the silicon layer using inductively coupled plasma etching in an SF_6-based plasma at a substrate temperature of -120 ⁰C. The final step is creating the membrane PhCs by selectively etching 350 nm of the buried oxide in buffered HF which is seen in Fig. 5.2(b).

After optical measurements of the empty crystal (i.e. holes not infilled), the chip is cleaned in isopropanol and dried with nitrogen gas, as a preparation for infilling. Infilling is performed with by applying a droplet of 2% solution by weight of elastomer in cyclohexane. Owing to its low viscosity and good wetting properties, the solution quickly spreads over the PhCs, flows through the holes and fills the space below the membrane, resulting in infilled PhCs with elastomer upper and lower cladding. These features can be seen in Fig. 5.3, which is a SEM image of an infilled device. The measurements are performed after a certain time, to make sure that the solvent has completely diffused out of the elastomer, as indicated by the stabilization of the spectral features.
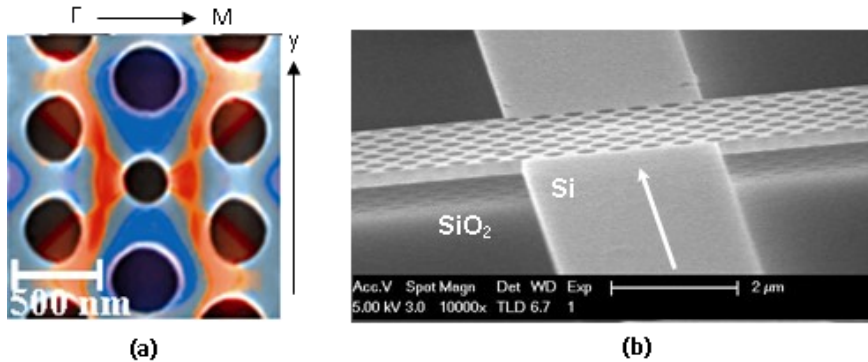
Figure 5.2. (a) SEM image of the cavity including the mode profile superimposed (Ey-field). The r/a ratio of the PhC is 0.32, while the modified central hole has r/a=0.22 and the half ellipses have ellipticity of 0.2. (b) Membrane PhC device. The arrow shows the propagation direction of the light through the waveguide.
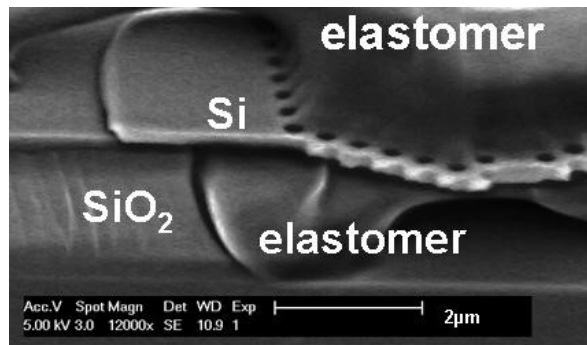

Figure 5.3. SEM image of a cleaved elastomer infilled PhC.

5.3 Transmission measurements

5.3.1 Optical measurement set-up

Optical transmission measurements are performed with the end-fire-technique using, a supercontinuum white light source (Fianium SC 400) in combination with a prism based spectral selection unit [29], giving a wavelength range 1300-1700 nm for the measurements. For excitation of transverse electric PhC modes, the polarization is selected in-plane with a polarizer. The light transmitted through the PhC is measured with an optical spectrum analyser (ANDO-AQ6315A). A temperature controller (Conductus LTC-10) is used to regulate the temperature of the chip, which is working with a heating resistor and a Pt100 temperature sensor mounted on the sample

holder. In the temperature range 20-60 ^{0}C the resulting accuracy of the sample-holder temperature is better than 0.2 ^{0}C.

5.3.2 Infill effect

Figure 5.4 shows the room-temperature transmission spectrum of one of the PhCs, in a range covering the air band edge and part of the bandgap, both for the empty and infilled situation. For the empty case the steep side at 1365 nm is the air band edge, while the strong peak at 1436 nm is the cavity resonance. These experimental positions show good agreement with the positions from the transmission spectrum we calculated with the finite-difference-time-domain (FDTD) simulator CrystalWave [68], as indicated with the blue vertical stripes in the upper part of the Fig. 5.2-a. After infilling, in spite of the decreased index contrast $n_{elast} = 1.478$ at 20 ^{0}C we still clearly observe the main features of the spectrum, which exhibits a pronounced red shift, as expected. The infill effect on the air band edge and on the cavity, resonance is clearly observed. The air band edge starts from 1500 nm and the cavity resonance is at 1570 nm, the shift in either case being about 135 nm. The FDTD simulations after infilling predict a stronger shift, as indicated by the red vertical stripes in Fig. 5.4. This difference will be discussed later in the text.
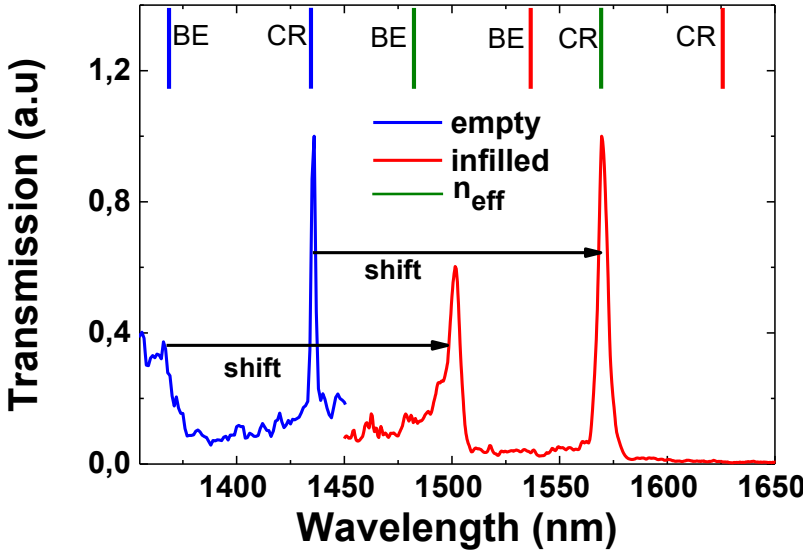
Figure 5.4. Transmission spectrum of empty (blue) and infilled (red) PhC, showing the air-band edge and the cavity resonance, the spectra normalized to unity for the cavity peak. The blue and red stripes denote simulated positions of the band edge (BE) and the cavity resonance (CR). The green stripes denote these positions for an index n_{eff}.

5.4 Global thermal tuning of the cavity resonance

In Fig. 5.5(a) we zoom in on the cavity peak, showing it in detail for nine temperatures. In addition to the temperature dependence of the peak after infilling shown in right panel of Fig. 5.5(a), we also present the data for the empty case in the left panel of Fig. 5.5(a), for reference. In the right panel, we observe the elastomer induced thermal tuning. With increasing temperature from 20 ^{0}C to 60 ^{0}C the cavity resonance peak shows a steady blue shift. After the temperature dependent transmission measurement for silicon cavity resonance shows a red shift due to having a positive TOC [69]. From comparison of empty and infilled PhC measurements, we conclude that the negative TOC of the elastomer overcompensates the positive TOC of the silicon. In addition, we observe the broadening of cavity resonance that shows the reduction of the quality factor which will be discussed below.

In Fig. 5.5 (b), peak shifts as a function of temperature for empty and infilled case are shown, which are obtained from the measurements and FDTD simulations, in which temperature dependent refractive index of silicon $n_{Si}(T) = 3.48 + 1.85 \times 10^{-4}(T - T_0)$ and aforementioned $n_{elast}(T)$ are used. From

the linear fits to data points for the empty case the total shift amounts are 2.1 nm and 2.4 nm, for the measurements and the simulations, respectively. This is considered as a good agreement. However, after infilling, the experimental and simulation data show an inconsistency. Over the total temperature range, the total amount of shift is -2.7 nm for measurements, while it is -4.4 nm for the simulations.

The thermal tuning behaviour can be understood from the perturbation expression for the relative shift of the resonance wavelength [4]:

$$\frac{\Delta\lambda(T)}{\lambda(T_0)} \approx \sum_i \frac{\Delta n_i(T)}{n_i(T_0)} \times fr(i) \tag{5.1}$$

Here the summation index denotes silicon or elastomer, $n_i(T_0)$ and $\Delta n_i(T)$ are the refractive indices at the reference temperature (20 ^{0}C) and the index perturbation resulting from heating the material to temperature T. Further, $fr(i)$ is the fraction of the electrical energy of the cavity mode in the region where the perturbation occurs. Simply putting $fr(Si) + fr(elast) = 1$, and using Eq. 5.1 combined with $n_{elast}(T)$ and $n_{Si}(T)$ we obtain $fr(Si) = 0.66$ and $fr(elast) = 0.34$. So, thermal tuning effect we observe results from the combination of 34% of the total energy of the cavity mode with the negative TOC of the elastomer.
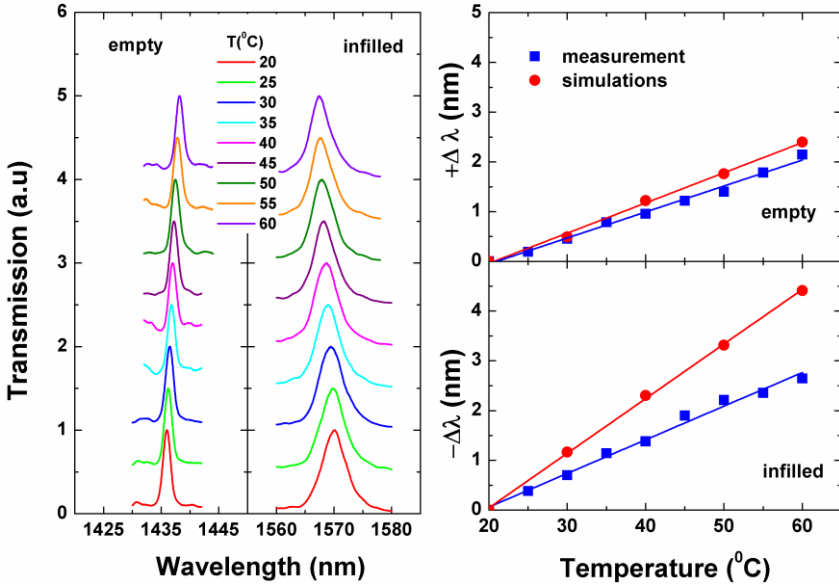
Figure 5.5. (a) Cavity resonance as a function of temperature for the empty and infilled PhC. The cavity resonance is normalized to unity and offset for clarity. (b) Temperature dependence of the measured and simulated shift of the cavity resonance, for the empty and infilled PhC. The lines are fits to data points.

The aforementioned discrepancies for the position of the band edge and the resonance, and for the resonance shift with temperature, suggests that the experiment probes effective values of the index and the TOC of the elastomer that are systematically some lower than the regular values. By performing further simulations, we find that for the band edge and resonance position the discrepancy is to a large extent removed by using $n_{eff} = 0.92 \times n_{elast}$ (green stripes in Fig. 5.5(b); stripe positions fitted to experimental positions, with emphasis on the resonance position). Since the cavity mode is more sensitive to the infilled holes than to the claddings, we interpret this reduced index as an indication of partially filled cavity holes. Contrary to holes in non-membrane PhCs, however, where partial filling may arise from air inclusions in the lower part of the holes [70] we suggest that here partial infilling has a different origin. Evaporation of the solvent out of the solution goes along with a density increase, leading to the regular density of the elastomer. In Ref [71], which treats solvent evaporation from large area polymer films, the density increase results from film-thickness reduction. In our case the elastomer solution in the holes is a three-dimensional system with an aspect ratio close to unity, so that size reduction in the lateral

direction may be expected as well, a process in which the cohesion forces of the compacting elastomer exceed the adhesion forces to the wall of a hole. Modelling the partial filling of cavity holes with an empty shell ($n=1$) surrounding a cylindrical elastomeric core, we find $f_{Shell} = 0.28$ and $f_{Core} = 0.72$ for the filling fractions. In view of the roughness of the model, these fractions show fair agreement with the ratio of the slopes of the lines in Fig. 5.5(b) for the infilled case, which amount to 0.61 and should be compared to $f_{Core} = 0.72$.

The quality factor Q is determined from the resonances in Fig. 5.5(a) for each measurement, using fits to the measured line shape. Figure 5.6 shows the resulting temperature dependence of Q, for the empty and infilled PhC, along with values obtained from simulations, for which in this case we use MEEP [72] in view of the Q values directly output by the Harminv tool. It is seen that as a result of infilling Q is drastically reduced form about 900 to about 330, while both for the empty case and after infilling Q is rather temperature insensitive. After infilling of the air holes with elastomer, due to the refractive index change from air to elastomer, the PhC mirror surrounding the cavity have a shallower bandgap and thus lower reflectivity [70]. For infilled cavity, when the temperature increases the cavity shows slight but steady increase of the Q, which arises from the index decrease of the elastomer that leads to a slight increase in the mirror reflectivity. The simulated Q values are systematically higher than the measured Q values, which we attribute to fabrication imperfections as mentioned above.
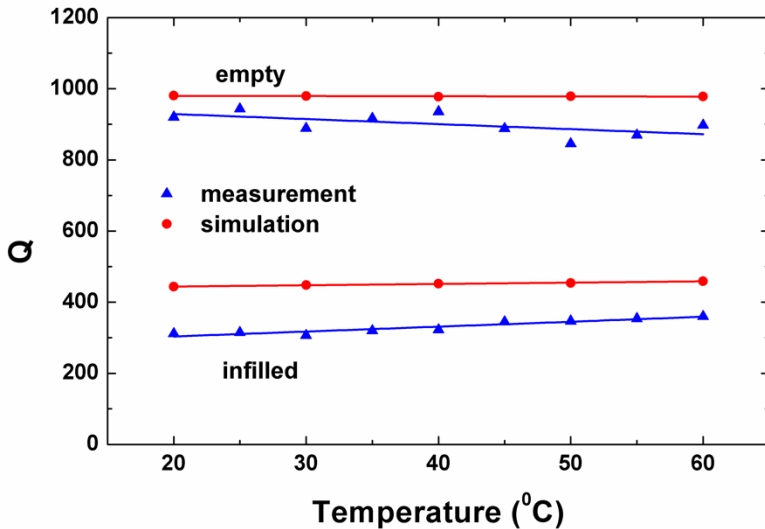
Figure 5.6. *T*-dependence of the measured and simulated quality factor (Q, x-axis) of the resonance, for the empty and infilled PhC.

5.5 Conclusions

In conclusion, global infilling of membrane silicon photonic crystals with the elastomer Kraton SEBS G 1657 and measurement of the transmission of a cavity in an infilled crystal as a function of temperature have been performed. The strong thermal expansion of the elastomer and the resulting negative thermo-optic coefficient of the elastomer lead to a pronounced blue shift on the cavity resonance with temperature. The experimental results are supported by simulations including a somewhat reduced density of the elastomer originating from the constrained geometry of the membrane with holes. These results call for local thermal tuning, for example using dye or quantum dot doping of the elastomer, which enables conversion of locally applied optical energy into heat.

CHAPTER 6

Conclusions and Future Work

6.1 Conclusions and Outlook

This thesis has explored the integration of MEMS-based microheaters, electron-beam lithography (EBL) techniques, nanoreactors, and photonic crystal (PhC) devices, demonstrating their combined potential for in situ transmission electron microscopy (TEM) and tunable nanophotonic applications. While the focus of the study has primarily been on MEMS-based platforms and in situ TEM experimentation, initial implementations of EBL and PhC components have been introduced to support future integration. By refining fabrication processes, optimizing material properties, and enhancing experimental methodologies, this work has addressed key challenges in nanoscale thermal control, high-resolution imaging, and optical device development.

A key contribution of this research is the development and optimization of MEMS-based microheaters for high-precision in situ TEM studies. The integration of platinum microheaters embedded in silicon nitride (SiN) membranes has enabled stable, reproducible heating up to 800°C, facilitating real-time investigations of temperature-dependent material transformations at the atomic scale. The fabrication approach combining photolithography, thin-film deposition, and reactive ion etching enabled uniform heating performance, which is essential for studies on catalysis, phase-change materials, and nanomaterial stability. The integration of electron-transparent SiN windows into MEMS heaters enhanced imaging resolution by reducing electron scattering, making these devices suitable for in situ functional analysis and advanced experimental setups. Overall, the methods developed in this thesis lay the groundwork for multi-modal in situ functional analysis in areas such as heterogeneous catalysis, battery research, and gas-phase nanomaterial synthesis, where precise temperature control at the nanoscale is critical.

This research has contributed to advancing electron-beam lithography (EBL) techniques for nanoscale patterning on ultrathin membranes by addressing the specific challenge of back-side alignment, which is a key limitation in conventional lithographic processes involving deep-etched substrates. The backside EBL approach developed in this work enables the fabrication of nanoscale free-standing structures by overcoming alignment and resist-coating difficulties commonly encountered on non-planar surfaces. This method has been successfully applied to fabricate gold nanobridges and nanoelectrodes for in situ TEM, facilitating the study of electromigration phenomena, nanoelectronic transport, and localized heating effects. In addition to these applications, the technique offers a route toward precision fabrication in areas such as quantum electronics, nanoelectromechanical

systems (NEMS), and single-molecule detection, where maintaining structural integrity at the nanoscale is essential.

Another significant outcome of this work is the design and fabrication of nanoreactors for high-pressure in situ TEM experiments, overcoming the limitations of conventional environmental TEM (ETEM) systems. The sandwiched-chip and single-chip nanoreactor designs developed in this thesis have demonstrated the ability to maintain vacuum integrity while allowing real-time gas-phase studies at pressures up to several bars. These nanoreactors, incorporating MEMS-based heating elements and electron-transparent SiN windows, enable atomic-resolution imaging of solid-gas interactions, catalytic transformations, and nanostructural changes under controlled environmental conditions. The optimization of sealing techniques, gas-flow dynamics, and contamination reduction strategies has positioned these nanoreactors as scalable, reproducible platforms for studying dynamic reactions in operando conditions. Furthermore, the successful integration of MEMS heaters within these nanoreactors suggests new possibilities for combining thermal, electrical, and gas-phase stimuli in multi-functional in situ TEM holders, expanding their applications to diverse fields such as energy materials, semiconductor processing, and nanoparticle synthesis.

In the realm of nanophotonics, this thesis has introduced a thermally tunable silicon PhC cavity using an elastomeric infill material, demonstrating a precisely controlled shift in the photonic bandgap. The experimental validation of temperature-dependent refractive index tuning confirms that the negative thermo-optic coefficient (TOC) of the elastomer effectively counteracts the positive TOC of silicon, enabling dynamic wavelength modulation with sub-nanometer precision. This approach provides a scalable, energy-efficient solution for reconfigurable photonic devices, with potential applications in optical switches, wavelength-selective filters, and photonic sensing technologies.

By bridging the disciplines of MEMS engineering, in situ electron microscopy, high-resolution lithography, and photonic device fabrication, this thesis has established a robust technological foundation for future advancements in nanoscale science and engineering. The methodologies developed here not only improve the precision, stability, and functionality of MEMS-based analytical devices but also enable new experimental paradigms for studying dynamic nanoscale phenomena in real time. The integration of MEMS heaters with nanoreactors, the application of backside EBL for free-standing nanostructures, and the demonstration of thermally tunable photonic cavities represent significant steps toward more versatile, high-performance devices for nanoelectronics, optoelectronics.

In previous chapters, two research topics were individually addressed as explained: the design, fabrication, and application of MEMS-based heaters with transmission electron microscopy (TEM) applications, and the study of photonic crystals and their applications. The thesis continued with an investigation into the optical properties of diamond photonic crystals, specifically examining nitrogen-vacancy (NV) centers, using cathodoluminescence (CL) in conjunction with transmission electron microscopy (TEM). Diamond's unique characteristics, including its wide bandgap and stable NV centers, make it an exceptional material for advanced photonic applications.

6.2 Future work: In-situ CL study of the diamond Photonic Crystals

In the next section of this chapter, we first examine the integration of cathodoluminescence (CL) spectroscopy with TEM for investigating the optical properties of nitrogen-vacancy (NV) centres in diamond photonic crystals. The chapter focuses on the design and implementation of a TEM holder adapted for in-situ CL experiments, where NV centres are studied under electron beam excitation. Despite extensive efforts, the experiments did not yield detectable NV-related optical signals, primarily due to challenges with fibre-diamond coupling and the impact of carbon coating on transmission. The chapter finishes with several recommendations for future work based on these preliminary findings. Suggestions include improvements in fibre-diamond coupling, the use of collector mirrors, and enhanced pre-experimental verification to optimize experimental conditions and, hopefully, achieve successful NV detection.

6.2.1 Introduction

This chapter explores the cathodoluminescence (CL) phenomenon in diamond photonic crystals containing nitrogen-vacancy (NV) centres, by using TEM. NV centres in diamond exhibit exceptional quantum properties, making them significant for various applications [73]. Investigating NV centres in photonic crystal structures enhances our understanding of their optical properties and light-matter interactions [74]. Utilizing CL with TEM enables a detailed examination of the emission behaviours of NV centres within complex diamond photonic crystal structures.

Photonic crystals are engineered materials with a periodic arrangement of dielectric materials that create photonic bandgaps, analogous to the electronic bandgaps in semiconductors [75]. These bandgaps restrict the propagation of certain wavelengths of light, giving rise to unique optical properties, such as high reflectivity and low transmission within the bandgap.

Photonic crystals find applications in a wide range of fields, including optical communication, sensing, and laser technology [4]. For photonic crystals detailed information is given in Chapter 1.

Diamond is an attractive material for photonic crystals due to its wide bandgap, excellent optical properties, high thermal conductivity, and chemical stability [76]. The exceptional refractive index contrast between diamond and air or other dielectrics allows for the precise engineering of photonic bandgaps, making diamond photonic crystals promising for various applications, including high-performance optical devices and quantum technologies. Diamond, with its unique optical and material properties, is now used in many different applications. Among its various defects, NV centres are particularly interesting because of their special quantum properties, like long coherence times and the ability to be controlled with light [74]. Using cathodoluminescence with TEM is one of the possible approaches to study the emission properties of NV centres in diamond photonic crystal structures, offering valuable information about their distribution and emission behaviour.

6.2.2   Principles of Cathodoluminescence with TEM

Cathodoluminescence is a powerful technique that involves the emission of photons from a material under the exposure of a focused high-energy electron beam, as in Transmission Electron Microscopy (TEM). This approach enables the study of a material's optical properties at the nanoscale, revealing details about luminescence behaviour, defects, and local electronic structure [77, 78].

Conducting cathodoluminescence experiments within a TEM requires specialized instrumentation, including photon detectors and tailored sample holders. The Gatan Vulcan holder [77], for example, has played a pivotal role in enabling such integrated studies. This advanced TEM holder allows precise control over electron beam application on a sample while simultaneously capturing its cathodoluminescence emission. By accurately adjusting the electron beam's position and intensity, researchers can spatially resolve cathodoluminescence emissions across different sample regions, offering detailed insights into the sample's nanoscale optical properties [77]. Furthermore, the Gatan Vulcan holder is compatible with various TEM systems, enhancing its versatility and broad applicability for investigating diamond photonic crystals and other nanostructured materials. This adaptability makes it a valuable tool for advanced optical studies in nanoscale materials science.
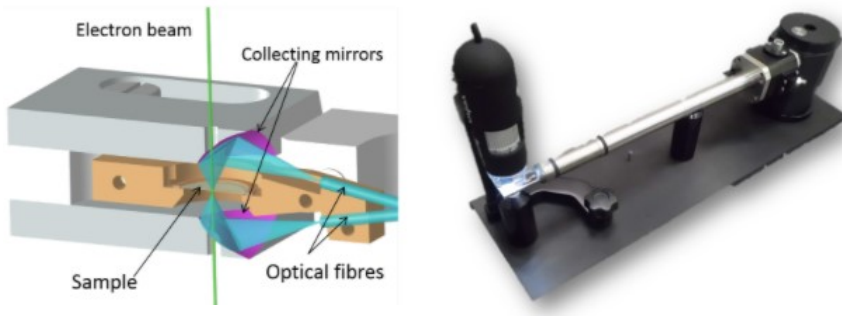
Figure 6.1. Gatan Vulcan holder. (a) Schematic representation of Vulcan holder light collection system (b) Full picture of Vulcan holder in workstation [77].

6.2.3   Experiments

To perform cathodoluminescence investigations on diamond photonic crystal samples, we required a setup that could capture the emitted light from the electron-specimen interaction within the Transmission Electron Microscope (TEM). Standard TEM holders lack the necessary features for in situ cathodoluminescence, prompting a need for modification to allow effective light collection and transmission. Therefore, we designed a custom holder equipped with a thin metal tube to accommodate an optical fibre. This fibre collects light generated by the electron interactions with the diamond photonic crystal sample. Figure 6.2 presents a schematic of this modified holder, with each component labelled for clarity. In this design, the conventional back-side o-ring, normally used for vacuum sealing, was removed. Instead, we inserted a metal tube into the holder and sealed it with a specialized adhesive to maintain a vacuum-tight environment within the TEM.

The fibre runs through the metal tube to the tip of the holder, allowing precise alignment with the electron-specimen interaction zone. Metal pins positioned at the holder's tip serve as reference markers, ensuring accurate fibre placement near the interaction region. Figure 6.3 shows an optical microscope image of the holder tip, with the fibre centered between the pins. Due to limited adjustability in the TEM's knobs, this alignment must be carefully established beforehand. Once positioned, the fibre is fixed in place using adhesive at the front and back ends of the tube, providing stability throughout the experiment.
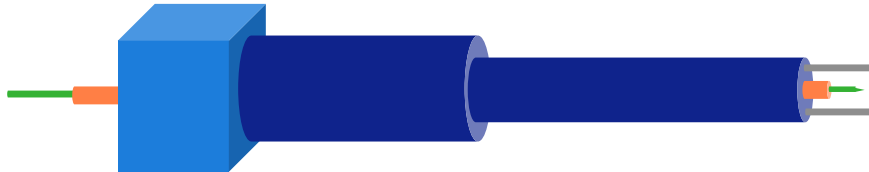
Figure 6.2. Sketch of TEM cathodoluminescence holder. The metal tube (orange) is inserted inside the holder in order to put optical fibre (green) through the holder. There are metal tips (grey) of the holder as a reference point for the optical fibre.
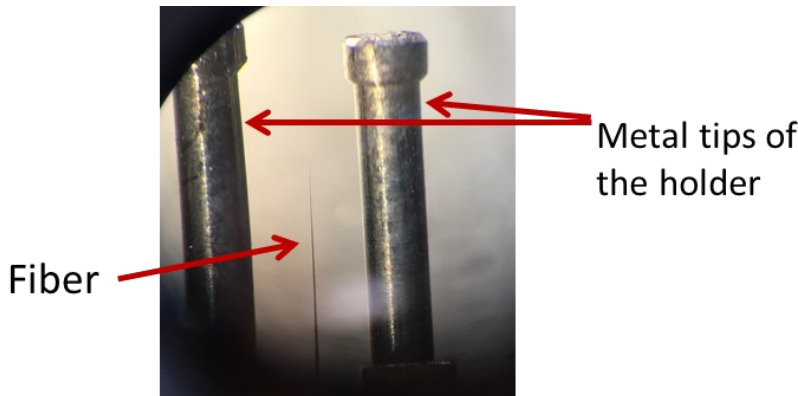

Figure 6.3. TEM cathodoluminescence holder tip including the fibre.

The fibre used in this experiment is called SM 600 which has operational wavelength between 633-780 nm. This wavelength range is suitable to observe NV centres cathodoluminescence signal [79]. To enhance the coupling between fibre and diamond [79], the tip of the fibre is tapered where the diamond photonic crystal is intended to be mounted.

The initial test of exposing the optical fibre to the e-beam was carried out without diamond. The aim was to understand the behaviour of the optical fibre under e-beam exposure. The tests resulted in charging and subsequently localized melting of the fibre tip, transforming the tapered shape of the tip into a ball-like form. To prevent charging and consequent melting of the tip, a thin carbon coating with a thickness of about 50 nm was deposited on top of it using a standard carbon coater for TEM samples. In this situation, carbon deposition on the fibre tip becomes the first and crucial step of the experiments.

After carbon deposition, the optical fibre was mounted into the TEM holder, as previously discussed and shown in Figures 6.2-6.3. The diamond photonic crystal was transferred onto the tip of the optical fibre using a glass

needle installed in a manual micromanipulator equipped with an optical microscope. Diamond photonic crystals are located on the chip (where they have been fabricated) as a membrane structure [76, 79]. In a first step and to remove diamond photonic crystals from the chip, a glass needle is prepared and mounted on the micromanipulator. This needle serves as a carriage. The diamond PhC is lifted from the chip and placed on the tip of the glass needle. Using the micromanipulator and optical microscope, the glass needle is moved close to the fibre. The electrostatic force between the fibre and the diamond plays a crucial role in mounting the diamond on top of the fibre. This step is very critical; there is a high chance of damaging the fibre tip or mounting the diamond specimen in the wrong place on the fibre. If the fibre tip is damaged, it needs to be replaced with a new fibre. If a diamond specimen is mounted in the wrong location, the initial attempt would be to remove the specimen without damaging the fibre and attempt to place it in the correct position.

The next step is to prepare the connecting of the fibre to the optical detector. The fibre has a cleaved end face and must be connected to another fibre, which can carry the signal to the OSA (Optical Spectrum Analyzer). Therefore, this step involves connecting the end of the fibre to another fibre. To avoid confusion, the fibre in the TEM holder is referred to as Fibre 1, and the one used for connection is referred to as Fibre 2 in subsequent parts of this chapter.

The fuse splicing method is used to connect the fibres. Fiber 2 is the same type as Fiber 1 (SM600) and has one APC (Angle Polished Connector) end for connection to the OSA. In the fuse splicing method, the following steps are executed: first, we strip the protective coatings from Fiber 2, leaving only the bare fibre. Second, we cleave the fibre. Third, the cleaved facets of Fibre 1 and Fibre 2 are mounted on a splicing device, which automatically aligns the fibres and then melts the fibres ends by heating, permanently welding the two fibres ends together. The last step is to protect the connected part from bending and tensile forces by using heat shrink tubing, as shown in Figure 6.4. After splicing, a laser light is connected to the APC connection of Fibre 2 to check whether the splicing works or not. Figure 6.5 shows that the laser light reaches the tip of Fibre 1, proving that the splicing works.

Figure 6.4. Spliced and protected fibres by heat shrink tubing.

As aforementioned, the exposure of the e-beam to the fibre tip causes charging and local melting of the fibre tip. Coating carbon on the fibre tip prevents this deformation. In order to understand the impact of coated carbon thickness on this charging and deformation, several TEM tests were performed. In addition to carbon thickness and charging variation, we also observed the impact of carbon thickness on the tip of the fibre in Figure 6.5. When the carbon thickness is around 5-10 nm, we see bright laser light at the end of the fibre tip as shown in Figure 6.5 (a).

In Figure 6.5(b), the carbon coating has a thickness of approximately 50 nm, and the tip of the fibre appears less bright due to reduced light transmission at the distal end. Light was coupled into the proximal end of the fibre using a stable laser source, with constant power and wavelength applied in both cases. The splicing method and tooling were also kept identical. Under these conditions, the thickness of the carbon layer plays a significant role in affecting the efficiency of light transmission. Nevertheless, a ~50 nm carbon coating was necessary to prevent local deformation of the fibre tip during electron-beam exposure.

Figure 6.5 TEM holder with Fibre 1 tip after splicing: (a) when the carbon thickness is ~ 5-10 nm. It was not possible to run experiments due to charging and deformation of the tip. (b) The carbon thickness is ~ 50 nm that enables to run experiments.

After splicing and verifying the connection between Fibre 1 and Fibre 2 with a laser, the next step is TEM experiments. To capture the optical signal from the fibre, an Optical Spectrum Analyzer (OSA) is connected to the APC end of Fibre 2. Operating within the wavelength range of 400-1700 nm, the OSA offers the flexibility to narrow down the wavelength scan range as necessary, with a maximum resolution of 0.05 nm. Figure 6.6 provides a visual representation of the TEM apparatus, showcasing the inserted holder, Fibre 1 protruding without an outer jacket, and Fibre 2, identifiable by its yellow outer jacket, connected to the OSA.
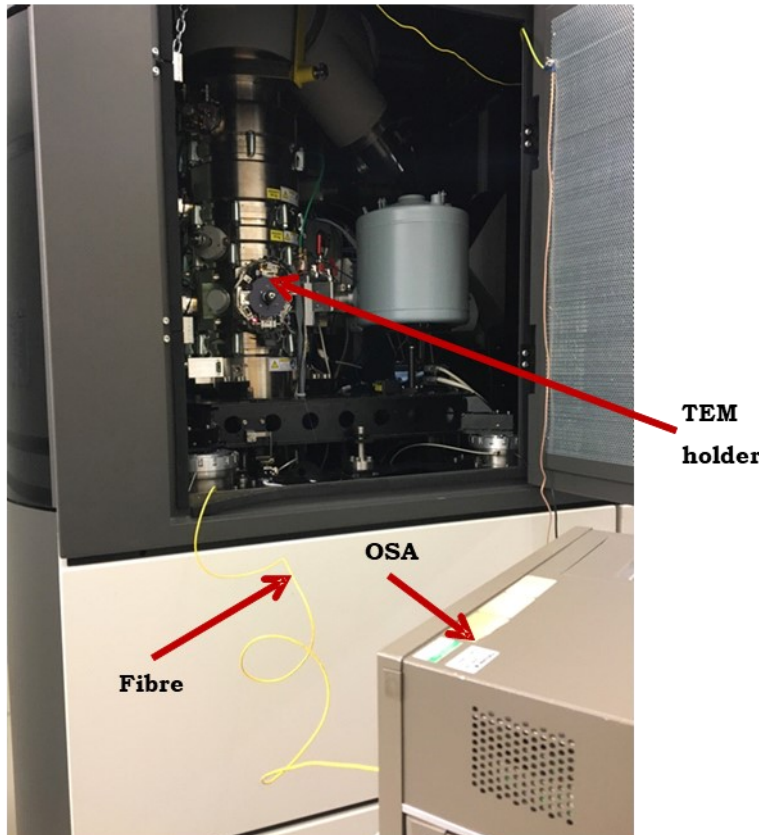
Figure 6.6. Cathodoluminescence experimental set-up including TEM (FEI Titan), Fibre 1 (without yellow outer jacked, not visible) comes out from TEM holder and Fibre 2 (partly with outer yellow jacket) connection and OSA.

Following all experimental preparations and the insertion of the TEM holder into the TEM, successful imaging of both the fibre tip and the diamond was achieved. Figure 6.7 presents the TEM images capturing the fibre tip and the diamond photonic crystal mounted at its apex. The images affirm the physical integrity of both the fibre and the diamond, indicating the absence of fibre-tip melting. Notably, the diamond photonic crystal is precisely positioned at a designated location on the tip, with its periodic structures clearly discernible on the diamond surface. Moreover, the precise positioning of the diamond holds significant importance, as it can influence the optical coupling efficiency, which was evidenced in prior research [79].
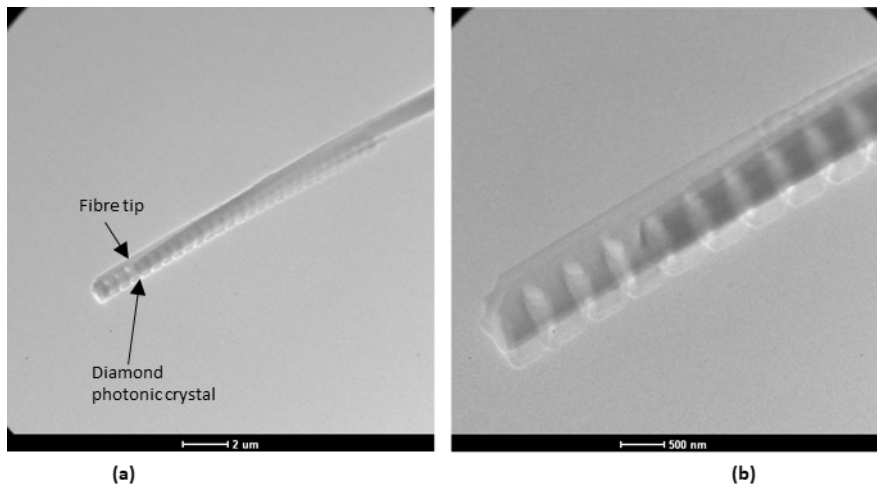
Figure 6.7. TEM images of the fibre tip and the diamond photonic crystal. (a) The tip of the fibre and photonic crystal, (b) magnified image of the diamond and partially the tip of the fibre. Electron beam is applied in different locations of the diamond photonic crystals to get NV cathodoluminescence signal.

The electron beam is focused on various locations on the diamond photonic crystals. Simultaneously, the wavelength range between 600-700 nm is scanned, where the cathodoluminescence signal is anticipated. The spectrum scanning was conducted with the high-resolution option of 0.2 nm by using an Optical Spectrum Analyzer (OSA). The aforementioned experiment has been repeated multiple times in an effort to obtain a discernible NV cathodoluminescence signal from the diamond photonic crystal. However, each attempt resulted in signals falling within the range of noise.

6.2.4 Conclusions

In this chapter, we have discussed the investigation of diamond photonic crystals by cathodoluminescence experiments using TEM. We covered the properties of diamond photonic crystals, the principles of cathodoluminescence, and the setup for TEM-based cathodoluminescence experiments. Despite these efforts, it was not possible to verify or demonstrate successful optical signal transfer after fibre splicing, nor was coupling from the fibre to the diamond photonic crystal confirmed with the current experimental configuration. The only feasible approach was to perform in situ TEM experiments and attempt to detect light emission when the electron beam was focused on the diamond. As mentioned earlier, the fibre and diamond were jointly inspected multiple times, but the optical signals recorded showed no clear evidence of NV-related emission. One possible explanation for this

outcome is the detection sensitivity limit of the optical spectrum analyzer (OSA). The OSA used in this study has a detection limit on the order of approximately –90 dBm (depending on the wavelength range and resolution bandwidth). Based on estimated photon yields from cathodoluminescence in diamond under similar beam conditions, the expected signal intensity may have been below this threshold, especially considering additional losses from imperfect coupling, absorption in the carbon coating, and scattering within the fibre.

To better understand the contributions of each factor, more advanced experimental setups are required. These include direct measurement of fibre connection losses, pre-characterization of coupling efficiency between the fibre tip and diamond using a calibrated optical setup, and quantitative analysis of carbon deposition effects on coupling. Unfortunately, due to time constraints and limited experimental infrastructure, these investigations could not be completed. Additionally, commercial cathodoluminescence holders offer enhanced capabilities; such as built-in collector mirrors or direct specimen illumination without a fibre interface; which may provide more favourable conditions for detecting NV signals in future work.

References

1. Williams, D.B. and C.B. Carter, *Transmission electron microscopy.* 2009: Springer.

2. Reimer, L. and H. Kohl, *Transmission Electron Microscopy* 2008: Springer Series in Optical Sciences (1–). Springer New York.

3. Young, N.P., et al., *Transformations of gold nanoparticles investigated using variable temperature high-resolution transmission electron microscopy.* Ultramicroscopy, 2010. **110**(5): pp. 506-516.

4. Joannopoulos, J.D., et al., *Photonic Crystals Molding the Flow of Light.* Second ed. 2008: Princeton University Press.

5. Haider, M., et al., *Electron microscopy image enhanced.* Nature, 1998. **392**(6678): pp. 768-769.

6. Egerton, R.F., *Electron energy-loss spectroscopy in the electron microscope.* 2005: Springer.

7. KILBY, J.S., *Turning potential into realities: The invention of the integrated circuit.* Proceeding of the IEEE, 2002. **16**(05): pp. 699-710.

8. Moore, G.E., *Cramming more components onto integrated circuits,* Electronics, 1965; reprinted in Proceedings of the IEEE, 1998. **38**(1): pp. 82-85.

9. Waldrop, M.M., *The chips are down for Moore's law* Nature, 2016. **530**(7589): pp. 144-147.

10. Intel. *Intel Ponte Vecchio GPU.* 2023; Available from: https://www.intel.com.

11. Intel. *Intel 2022 Investor Meeting.* 2022; Available from: https://www.intel.com.

12. Markov, I.L., *Limits on fundamental limits to computation.* Nature, 2014. **512**(7513): pp. 147-154.

13. Miller, D.A.B., *Device requirements for optical interconnects to silicon chips.* Proceedings of the IEEE, 2009. **97**(7): pp. 1166-1185.

14. Yablonovitch, E., *Inhibited Spontaneous Emission in Solid-State Physics and Electronics.* Physical Review Letters, 1987. **58**(20): pp. 2059-2062.

15. Tanabe, T., et al., *All-optical switches on a silicon chip realized using photonic crystal nanocavities.* Applied Physics Letters, 2005. **87**(15): pp. 151112.

16. Tanabe, T., et al., *Fast bistable all-optical switch and memory on a silicon photonic crystal on-chip.* Optics Letters, 2005. **30**(19): pp. 2575-2577.

17.   Painter, O., et al., *Two-dimensional photonic band-gap defect mode laser.* Science, 1999. **284**(5421): pp. 1819-1821.

18.   Takano, H., et al., *In-plane-type channel drop filter in a two-dimensional photonic crystal slab.* Applied Physics Letters, 2004. **84**(13): pp. 2226-2228.

19.   Velha, P., et al., *Temperature tuning of ultra high Q/V SOI microcavities - art. no. 69891P.* Photonic Crystal Materials and Devices Viii, 2008. **6989**: pp. 69891P1-P6.

20.   Wild, B., et al., *Temperature tuning of the optical properties of planar photonic crystal microcavities.* Applied Physics Letters, 2004. **84**(6): pp. 846-848.

21.   Englund, D., et al., *Electrically controlled modulation in a photonic crystal nanocavity.* Optics Express, 2009. **17**(18): pp. 15409-15419.

22.   Hopman, W.C.L., et al., *Nano-mechanical tuning and imaging of a photonic crystal micro-cavity resonance.* Optics Express, 2006. **14**(19): pp. 8745-8752.

23.   Alan, T., et al., *Micro-fabricated channel with ultra-thin yet ultra-strong windows enables electron microscopy under 4-bar pressure.* Applied Physics Letters, 2012. **100**(8): pp. 081903(1-4).

24.   Song, B., et al., *Atomic-Scale Electron-Beam Sculpting of Near-Defect-Free Graphene Nanostructures.* Nano Letters, 2011. **11**(6): pp. 2247-2250.

25.   Yalcin, A.O., et al., *Core-shell reconfiguration through thermal annealing in FexO/CoFe2O4 ordered 2D nanocrystal arrays.* Nanotechnology, 2014. **25**(5): pp. 055601 (9pp).

26.   Yablonovitch, E., *Photonic Band-Gap Crystals.* Journal of Physics-Condensed Matter, 1993. **5**(16): pp. 2443-2460.

27.   Malladi, S., et al. *Studies on In Situ Heat-Treatment and Corrosion of Al Alloy 2024 in a TEM.* in *2015 MRS Spring Meeting* 2015. San Francisco.

28.   Malladi, S., et al., *Localised corrosion in aluminium alloy 2024-T3 using in situ TEM.* Chemical Communications, 2013. **49**(92): pp. 10859-10861.

29.   Dunsby, C., et al., *An electronically tunable ultrafast laser source applied to fluorescence imaging and fluorescence lifetime imaging microscopy.* Journal of Physics D-Applied Physics, 2004. **37**(23): pp. 3296-3303.

30.   van Leest, M.M., *Tuning of a Si photonic crystal cavity with elastomeric infilling.* 2009, MSc Thesis, Delft University of Technology.

31.   Heiden, R.v.d., *InP-based Planar Photonic Crystals*, in *Applied Physics*. 2006, PhD Thesis, Eindhoven University of Technology.

32.   Wu, M.C., A. Solgaard, and J.E. Ford, *Optical MEMS for lightwave communication*. Journal of Lightwave Technology, 2006. **24**(12): pp. 4433-4454.

33.   Voldman, J., M.L. Gray, and M.A. Schmidt, *Microfabrication in biology and medicine*. Annual Review of Biomedical Engineering, 1999. **1**: pp. 401-425.

34.   Tichelaar, F.D., M.A. van Huis, and H.W. Zandbergen, *Transmission Electron Microscopy as Nanolab*, in *Handbook of Nanoscopy*. 2012, Wiley-VCH Verlag GmbH & Co. KGaA. pp. 345-374.

35.   Neklyudova, M., et al., *Through-membrane electron-beam lithography for ultrathin membrane applications*. Applied Physics Letters, 2017. **111**(6): pp. 063105.

36.   Reed, M.A., et al., *Conductance of a molecular junction*. Science, 1997. **278**(5336): pp. 252-254.

37.   Chen, W., H. Ahmed, and K. Nakazoto, *Coulomb-Blockade at 77 K in Nanoscale Metallic Islands in a Lateral Nanostructure*. Applied Physics Letters, 1995. **66**(24): pp. 3383-3384.

38.   Park, J., et al., *Coulomb blockade and the Kondo effect in single-atom transistors*. Nature, 2002. **417**(6890): pp. 722-725.

39.   Kubatkin, S., et al., *Single-electron transistor of a single organic molecule with access to several redox states*. Nature, 2003. **425**(6959): pp. 698-701.

40.   Ke, S.H., H.U. Baranger, and W. Yang, *Electron transport through molecules: Self-consistent and non-self-consistent approaches*. Physical Review B, 2004. **70**(8): pp. 085410.

41.   Strachan, D.R., et al., *Controlled fabrication of nanogaps in ambient environment for molecular electronics* Applied Physics Letters, 2005. **86**(4): pp. 043109.

42.   Zandbergen, H.W., et al., *Sculpting nanoelectrodes with a transmission electron beam for electrical and geometrical characterization of nanoparticles*. Nano Letters, 2005. **5**(3): pp. 549-553.

43.   Strachan, D.R., et al., *Clean electromigrated nanogaps imaged by transmission electron microscopy*. Nano Letters, 2006. **6**(3): pp. 441-444.

44.   Rudneva, M., et al., *In Situ Transmission Electron Microscopy Imaging of Electromigration in Platinum Nanowires*. Microscopy and Microanalysis, 2013. **19**: pp. 43-48.

45.   Creemer, J.F., et al., *Atomic-scale electron microscopy at ambient pressure.* Ultramicroscopy, 2008. **108**(9): pp. 993-998.

46.   Alan, T., et al. *Characterization of ultrathin membranes to enable TEM observation of gas reactions at high pressures.* in *ASME 2009 International Mechanical Engineering Congress and Exposition.* 2009. American Society of Mechanical Engineers.

47.   Yokosawa, T., et al., *In-situ TEM on (de)hydrogenation of Pd at 0.5-4.5 bar hydrogen pressure and 20-400 degrees C.* Ultramicroscopy, 2012. **112**(1): pp. 47-52.

48.   Creemer, J., et al. *An all-in-one nanoreactor for high-resolution microscopy on nanomaterials at high pressures.* in *Micro Electro Mechanical Systems (MEMS), 2011 IEEE 24th International Conference on.* 2011. IEEE.

49.   *http://www.denssolutions.com/.* 2015.

50.   *http://www.hummingbirdscientific.com/.* 2015.

51.   *http://www.protochips.com/.* 2015.

52.   Xin, H.L.L., et al., *In Situ TEM Study of Catalytic Nanoparticle Reactions in Atmospheric Pressure Gas Environment.* Microscopy and Microanalysis, 2013. **19**(6): pp. 1558-1568.

53.   Ghassemi, H., et al., *In situ environmental transmission electron microscopy study of oxidation of two-dimensional Ti3C2 and formation of carbon-supported TiO2.* Journal of Materials Chemistry A, 2014. **2**(35): pp. 14339-14343.

54.   de Jonge, N. and F.M. Ross, *Electron microscopy of specimens in liquid.* Nature Nanotechnology, 2011. **6**(11): pp. 695-704.

55.   Radisic, A., et al., *Quantifying electrochemical nucleation and growth of nanoscale clusters using real-time kinetic data.* Nano Letters, 2006. **6**(2): pp. 238-242.

56.   Nielsen, M.H., S. Aloni, and J.J. De Yoreo, *In situ TEM imaging of CaCO3 nucleation reveals coexistence of direct and indirect pathways.* Science, 2014. **345**(6201): pp. 1158-1162.

57.   de Jonge, N., M. Pfaffa, and D.B. Peckysa, *Practical Aspects of Transmission Electron Microscopy in Liquid.* Advances in Imaging and Electron Physics, 2014: pp. 1.

58.   Holtz, M.E., et al., *Nanoscale Imaging of Lithium Ion Distribution During In Situ Operation of Battery Electrode and Electrolyte.* Nano Letters, 2014. **14**(3): pp. 1453-1459.

59.   Zhu, G.Z., et al., *In Situ Liquid Cell TEM Study of Morphological Evolution and Degradation of Pt-Fe Nanocatalysts During Potential*

Cycling. Journal of Physical Chemistry C, 2014. **118**(38): pp. 22111-22119.

60. Hart, T.R., R.L. Aggarwal, and B. Lax, *Temperature Dependence of Raman Scattering in Silicon.* Physical Review B-Solid State, 1970. **1**(2): pp. 638-642.

61. Huang, F.M., et al., *Temperature dependence of the Raman spectra of carbon nanotubes.* Journal of Applied Physics, 1998. **84**(7): pp. 4022-4024.

62. Vendelbo, S.B., et al., *Visualization of oscillatory behaviour of Pt nanoparticles catalysing CO oxidation.* Nature Materials, 2014. **13**(9): pp. 884-890.

63. Fushman, I., et al., *Ultrafast nonlinear optical tuning of photonic crystal cavities.* Applied Physics Letters, 2007. **90**(9): pp. 091118-3.

64. Leonard, S.W., et al., *Tunable two-dimensional photonic crystals using liquid-crystal infiltration.* Physical Review B, 2000. **61**(4): pp. R2389-R2392.

65. Polymers, K., *http://www.kraton.com/*. 2011.

66. Ye, W.N., J. Michel, and L.C. Kimerling, *Athermal high-index-contrast waveguide design.* Ieee Photonics Technology Letters, 2008. **20**(9-12): pp. 885-887.

67. Loncar, M., et al., *High quality factors and room-temperature lasing in a modified single-defect photonic crystal cavity.* Optics Letters, 2004. **29**(7): pp. 721-723.

68. CrystalWave, *http://www.photond.com/products/crystalwave.htm*. 2011.

69. Cocorullo, G., F.G. Della Corte, and I. Rendina, *Temperature dependence of the thermo-optic coefficient in crystalline silicon between room temperature and 550 K at the wavelength of 1523 nm.* Applied Physics Letters, 1999. **74**(22): pp. 3338-3340.

70. Martz, J., et al., *Liquid crystal infiltration of InP-based planar photonic crystals.* Journal of Applied Physics, 2006. **99**(10): pp. 103105-4.

71. Tsige, M. and G.S. Grest, *Solvent evaporation and interdiffusion in polymer films.* Journal of Physics-Condensed Matter, 2005. **17**(49): pp. S4119-S4132.

72. Oskooi, A.F., et al., *MEEP: A flexible free-software package for electromagnetic simulations by the FDTD method.* Computer Physics Communications, 2010. **181**(3): pp. 687-702.

73. Davies, G. and M.F. Hamer, *Optical Studies of 1.945 Ev Vibronic Band in Diamond.* Proceedings of the Royal Society of London Series

a-Mathematical and Physical Sciences, 1976. **348**(1653): pp. 285-298.

74.   Gruber, A., et al., *Scanning confocal optical microscopy and magnetic resonance on single defect centers.* Science, 1997. **276**(5321): pp. 2012-2014.

75.   Yablonovitch, E., *Photonic Band-Gap Structures.* Journal of the Optical Society of America B-Optical Physics, 1993. **10**(2): pp. 283-295.

76.   Burek, M.J., et al., *High quality-factor optical nanocavities in bulk single-crystal diamond.* Nature Communications, 2014. **5**: pp. 5718.

77.   Gatan. *Cathodoluminescence from insulators, metals, and plasmonics, https://www.gatan.com/cathodoluminescence-insulators-metals-and-plasmonics.*

78.   Strunk, H.P., M. Albrecht, and H. Scheel, *Cathodoluminescence in transmission electron microscopy.* Journal of Microscopy, 2006. **224**: pp. 79-85.

79.   Hausmann, B.J.M., et al., *Coupling of NV Centers to Photonic Crystal Nanobeams in Diamond.* Nano Letters, 2013. **13**(12): pp. 5791-5796.

Summary

This thesis investigates the fabrication and application of MEMS-based devices and photonic structures, focusing on innovative fabrication techniques and their implementation in various scientific fields. The research covers the development of MEMS-based microheaters, silicon photonic crystals, novel electron-beam lithography methods, and nanoreactors for in situ gas environment studies. Additionally, it explores the thermal tuning of photonic devices, presenting new possibilities for advancements in nanoscale research and device performance.

A detailed description is provided of the fabrication processes for MEMS-based microheaters and silicon photonic crystals, highlighting critical steps such as design, lithography, etching, and deposition. These processes are key to ensuring the precision and functionality of the devices, which are later employed in experiments involving nanoreactors and photonic systems. The importance of these fabrication steps lies in their ability to achieve the level of control needed for reliable experimental outcomes.

A novel fabrication technique, referred to as "through membrane e-beam lithography," is introduced. This method allows for the exposure of electron beam resist through thin membranes, including those embedded with metal lines, enabling enhanced control over membrane flatness. Such precision is crucial for applications in electromigration of metals and semiconductors, and in the fabrication of electron-transparent silicon nitride (SiN) windows. These windows are pivotal in reducing noise in DNA translocation experiments and facilitating in situ studies in liquid cell environments. The technique's advantages extend to battery material analysis and environmental studies, with potential future applications in nanogap electrode formation.

The development of closed-cell systems for in situ transmission electron microscopy (TEM) studies in gas environments is also explored. These systems, known as nanoreactors, incorporate MEMS-based devices and electron-transparent windows, allowing for atomic-resolution observation of gas-material interactions under high-pressure conditions. The thesis details the design and fabrication of these nanoreactors, which facilitate drift-stabilized, high-resolution environmental TEM studies. The use of such nanoreactors is crucial for advancing our understanding of dynamic material transformations, particularly in catalytic and environmental applications.

In the domain of photonic devices, the thesis investigates the thermal and optical properties of silicon photonic crystals infilled with the elastomer. The research demonstrates that the thermal expansion of the elastomer

causes a pronounced blue shift in the photonic crystal's cavity resonance as temperature increases. Supported by simulations, the findings show that the constrained geometry of the elastomer in the membrane reduces its density, affecting the crystal's optical performance. This thermal tuning capability holds significant potential for applications in sensing, telecommunications, and optoelectronics. Further possibilities for local thermal tuning, through the use of dyes or quantum dots, are suggested, enabling precise control over the conversion of optical energy into heat in photonic systems.

The thesis concludes with an investigation into the use of cathodoluminescence (CL) in combination with TEM for studying diamond photonic crystals containing nitrogen-vacancy (NV) centres. After introducing the principles of CL in TEM and existing commercial CL holders, a custom TEM holder is designed in which an optical fibre is routed through a thin metal tube to the sample region. Diamond photonic crystal samples are positioned on the tapered fibre tip, and the system is used to attempt CL measurements in the NV emission range. Despite multiple experiments, no clear NV-related CL signal is detected: the recorded spectra remain at the noise level. The thesis analyses the likely causes of this outcome, including limited fibre–diamond coupling, absorption in the protective carbon coating on the fibre tip, and the detection limit of the optical spectrum analyser. Based on these results, several recommendations are proposed for future work, such as improved alignment and pre-characterization of fibre–diamond coupling, direct measurement of optical losses, and the possible use of CL holders with integrated collector mirrors to enhance collection efficiency.

In summary, this thesis makes substantial contributions to the fabrication and application of MEMS-based microheaters, advanced lithography on thin membranes, nanoreactor systems for gas-phase in-situ TEM, and elastomer-tuned photonic crystal devices, and it explores the integration of CL spectroscopy with TEM for diamond photonic crystals. By developing and refining these fabrication techniques and experimental platforms, the work provides conducting controlled, high-resolution studies of materials and photonic structures under realistic thermal and environmental conditions.

Samenvatting

Dit proefschrift beschrijft de fabricage en toepassing van MEMS-gebaseerde apparaten en fotonische structuren, met een focus op innovatieve fabricagetechnieken en hun toepassing binnen diverse wetenschappelijke domeinen. Het onderzoek omvat de ontwikkeling van MEMS-microheaters, silicium-fotonische kristallen, nieuwe methoden voor elektronenbundellithografie en nanoreactoren voor in-situ studies in gasomgevingen. Daarnaast wordt de thermische afstemming van fotonische componenten onderzocht, waarmee nieuwe mogelijkheden worden geboden voor vooruitgang in onderzoek en prestaties op de nanoschaal.

Er wordt een gedetailleerde beschrijving gegeven van de fabricageprocessen voor MEMS-microheaters en silicium-fotonische kristallen, waarin kritische stappen zoals ontwerp, lithografie, etsen en depositie worden behandeld. Deze processen zijn essentieel om de nauwkeurigheid en functionaliteit van de structuren te waarborgen, zodat zij later kunnen worden ingezet in experimenten met nanoreactoren en fotonische systemen. Deze fabricagestappen zijn essentieel voor controleerbare en betrouwbare experimentele resultaten.

Een nieuwe fabricagetechniek, aangeduid als "through-membrane e-beam lithography", wordt geïntroduceerd. Deze methode maakt het mogelijk om elektronenbundellak aan de achterzijde van dunne membranen te belichten door de membranen heen, ook wanneer zich metaallijnen in het membraan bevinden. Hierdoor kan de vlakheid en dikte van het membraan beter worden gecontroleerd. Deze nauwkeurigheid is van groot belang voor toepassingen zoals elektromigratie-studies van metalen en halfgeleiders, en voor de fabricage van elektronen-transparante silicium-nitride (SiN) vensters. Dergelijke vensters zijn essentieel voor het verminderen van ruis in DNA-translocatie-experimenten en voor in-situ studies in vloeistofcellen. De voordelen van deze techniek strekken zich ook uit tot onderzoeken van batterijmaterialen en milieustudies, met toekomstige mogelijkheden voor de realisatie van nanogap-elektroden.

Ook de ontwikkeling van gesloten-celsystemen voor in-situ transmissie-elektronenmicroscopie (TEM) in gasomgevingen wordt onderzocht. Deze systemen, nanoreactoren genoemd, combineren MEMS-structuren met elektronen-transparante vensters, waardoor observatie van gas-materiaalinteracties met atomaire resolutie onder hoge druk mogelijk wordt. Het proefschrift beschrijft het ontwerp en de fabricage van deze nanoreactoren, die drift-gestabiliseerde studies met hoge-resolutie in de TEM in een gasomgeving mogelijk maken. Het gebruik van dergelijke systemen is

van cruciaal belang voor het begrijpen van dynamische materiaaltransformaties, vooral in katalytische en milieutoepassingen.

Op het gebied van fotonische componenten beschrijft dit proefschrift de thermische en optische eigenschappen van silicium-fotonische kristallen die zijn opgevuld met een elastomeer. Het onderzoek toont aan dat de thermische uitzetting van het elastomeer een duidelijke blauwverschuiving veroorzaakt in de resonantie van de fotonische kristalcaviteit bij stijgende temperatuur. Deze bevindingen worden ondersteund door simulaties, die aantonen dat de ingesloten geometrie van het elastomeer in het membraan leidt tot een verminderde dichtheid, wat de optische prestaties van het kristal beïnvloedt. Deze vorm van thermische afstemming biedt aanzienlijke mogelijkheden voor toepassingen in sensing, telecommunicatie en opto-elektronica. Tevens worden verdere mogelijkheden besproken voor lokale thermische afstemming door het gebruik van kleurstoffen of quantumdots, waarmee de omzetting van optische energie in warmte nauwkeurig kan worden gestuurd.

Het proefschrift sluit af met een onderzoek naar het gebruik van kathodoluminescentie (CL) in combinatie met TEM voor het bestuderen van diamanten fotonische kristallen met stikstof-vacature (NV) centra. Het ontwerp van een op maat gemaakte TEM-houder wordt beschreven, waarin een optische vezel door een metalen buis naar het beeldveld wordt geleid. Op het eind van deze vezel, die taps toeloopt, wordt het diamanten fotonische kristal gemonteerd. Dit systeem wordt gebruikt om CL-metingen uit te voeren binnen het NV-emissiebereik. Ondanks dat er herhaaldelijke pogingen zijn ondernomen, is er geen duidelijk NV-gerelateerd CL-signaal gedetecteerd; de gemeten spectra blijven op ruisniveau. Verschillende oorzaken voor het uitblijven van een signaal worden besproken, waaronder beperkte koppeling tussen vezel en diamant, absorptie in de beschermende koolstoflaag op de vezeltip en de detectiegrens van de spectrometer. Op basis van deze inzichten worden aanbevelingen gedaan voor toekomstig onderzoek, zoals verbeterde uitlijning, voor-karakterisatie van de vezel-diamantkoppeling en de directe meting van optische verliezen.

Samenvattend levert dit proefschrift belangrijke bijdragen aan de fabricage en toepassing van MEMS-microheaters, geavanceerde lithografiebehandelingen op dunne membranen, nanoreactoren voor gasfase-in-situ TEM en elastomeer-afgestemde fotonische kristallen, en het onderzoekt de integratie van CL-spectroscopie met TEM voor diamanten fotonische structuren. Door deze fabricagetechnieken en experimentele platforms te ontwikkelen en te verfijnen, ondersteunt dit werk gecontroleerde, hoge-resolutie studies van materialen en fotonische structuren onder realistische thermische en omgevingscondities.

Acknowledgement

I would like to express my sincere gratitude to everyone who supported and accompanied me throughout this long and demanding journey of my PhD.

First and foremost, I would like to thank my promotor, Prof. Paddy French, for his invaluable support and guidance during the final phase of my doctoral studies. He kindly accepted to become my promotor at a crucial stage of this journey, and without his continuous encouragement, patience, and trust, this thesis would not have been completed. I am deeply grateful for his commitment and support.

I would also like to express my sincere appreciation to my second promotor, Prof. Urs Staufer, for his critical feedback and insightful discussions. His constructive comments helped me to think more deeply and critically about the content of this thesis and significantly improved the quality of the work.

At the beginning of this journey, I am grateful to Prof. Huub Salemink and Dr. Jaap Caro for offering me the opportunity to start my PhD at TU Delft and the Kavli Institute of Nanoscience. Photonics has always been my passion, and it was an inspiring experience to be part of the photonics team at such a unique institute and university. I truly appreciated that both Prof. Salemink and Dr. Caro were always approachable for scientific as well as personal discussions. I thank them sincerely for their support during the early stages of my PhD.

I benefited greatly from working with highly knowledgeable colleagues, especially Thijs van Leest, Delphine Brousse, and Nguyen Minh Hoang. I thank them for the fruitful scientific discussions and for the enjoyable moments we shared outside the laboratory.

During the middle phase of my PhD, I had the opportunity to take on a new challenge by joining the High-Resolution Electron Microscopy (HREM) group under the supervision of Prof. Henny Zandbergen. During this period, I spent extensive time in the cleanroom fabricating MEMS heaters and nanoreactors. I significantly expanded my fabrication skill set by developing MEMS heaters and nanoreactors from mask design to final device delivery for experimental applications. Seeing these chips being successfully used in important and challenging research was a breakthrough moment for me. I am especially grateful to Prof. Zandbergen for giving me this opportunity and for his support throughout this part of my PhD. I also thank the HREM group members Frans Tichelaar, Tom de Kruijf, Anil Ozan Yalcin, Sairam Malladi,

List of Publications

1. M. Neklyudova, A.K. Erdamar, L.Vicarelli, S.J. Heerema, T. Rehfeldt, G. Pandraud, Z.Kolahdouz, C. Dekker, H.W. Zandbergen, "Through-membrane electron-beam lithography for ultrathin membrane applications", Applied Physics Letters,111, 063105, 2017

2. M. Neklyudova, C. Sabater, A.K. Erdamar, J.M. van Ruitenbeek, H.W. Zandbergen, "In situ transmission electron microscope formation of a single-crystalline Bi film on an amorphous substrate", Applied Physics Letters,110, 103101 2017.

3. S. Malladi, A.K. Erdamar, T. de Kruijff, C. Liu, F. Tichelaar, H.W. Zandbergen, "Improved gas holder for in-situ TEM studies", European Microscopy Conference, 153-154, August 28-September 02, 2016.

4. A.K. Erdamar, S. Malladi, F.D. Tichelaar, H.W. Zandbergen,Title of Chapter: "Closed Cell Systems for in-situ TEM with gas environments ranging from 0.1 to 5 bar", In T.W. Hansen and J.B. Wagner (Eds.), Title of the book: Controlled Atmosphere Transmission Electron Microscopy, Springer Science+Business Media, January 2016.

5. S. Malladi, A.K. Erdamar, T. de Kruijff, C. Liu, F. Tichelaar, H.W. Zandbergen, "Studies on In Situ Heat-Treatment and Corrosion of Al Alloy 2024 in a TEM", Materials Information Using Novel Techniques in Electron Microscopy, at 2015 MRS Spring Meeting & Exhibit, San Francisco CA, April 6-10, 2015.

6. A.O. Yalcin, B. Goris, R.J.A. van Dijk-Moes, Z. Fan, A.K. Erdamar, F.D. Tichelaar, T.J.H Vlugt, G. van Tendeloo, S. Bals, D. Vanmaekelbergh, H.W. Zandbergen, M.A. van Huis, "Heat-induced transformation of CdSe-Cds-ZnS core-multishell quantum dots by Zn diffusion into inner layers", Chemmical Communications, 51, 16, 3320-3323, 2015.

7. S. Malladi, S. Basak, MY Wu, Q Xu, A.K. Erdamar, F.D. Tichelaar, H.W. Zandbergen, "In situ environmental TEM studies using MEMS based devices", International Microscopy Congress, Prague, 2014.

8. A.K. Erdamar, H.W. Zandbergen, "Mems-based heaters for ultrahigh temperature in situ TEM studies", International Microscopy Congress, Prague, 2014.

9. A.K. Erdamar, M.M. van Leest, S.J. Picken, J. Caro, "Tuning of a cavity in a silicon photonic crystal by thermal expansion of an elastomeric infill", Applied Physics Letters, 99, 111113, 2011.

10. A. K. Erdamar, M.M. van Leest, S.J. Picken, J. Caro, "Thermal tuning of a silicon photonic crystal cavity infilled with an elastomer", Proc. SPIE 8095, 80951J, San Diego CA, 2011.

11. H. Cankaya, U. Demirbas, A. K. Erdamar, A. Sennaroglu, "Absorption saturation analysis of Cr2+: ZnSe and Fe2+: ZnSe", JOSA B, 25 (5), 794-800, 2008.
12. S. Celebi, A. K. Erdamar, A. Sennaroglu, A. Kurt, H. Y. Acar, "Synthesis and characterization of poly (acrylic acid) stabilized cadmium sulfide quantum dots", The Journal of Physical Chemistry B, 111 (44), 12668-12675, 2007.

Curriculum Vitae

03 June 1982	Born in Ankara, Türkiye

2000-2005   Bachelor of Science in Physics, Middle East Technical University, Ankara, Türkiye

2005-2007   Master of Science in Physics, Koc University, Istanbul, Türkiye

Thesis title: *Spectroscopic Investigation of CdS Quantum Dots and Fe^{2+}: ZnSe*

2007-2009   Trainee at the Stan Ackermans Institute, TU Eindhoven, Holst Center

Eindhoven, the Netherlands

2009-2016   PhD Researcher at Faculty Applied Science, Kavli Institute of Nanoscience, TU Delft

Delft, the Netherlands

January 2026, thesis title: *Temperature-Controlled MEMS Reactors and Photonic Crystals for In-Situ Transmission Electron Microscopy*

2016- present   Employed in different positions at ASML

Since 2023: Product Manager at ASML

Veldhoven, the Netherlands